January 2021

VNIR Spectral Properties Of Five G-Class Asteroids: Implications For Mineralogy And Geologic Evolution

Justin Todd Germann

VNIR SPECTRAL PROPERTIES OF FIVE G-CLASS ASTEROIDS: IMPLICATIONS FOR MINERALOGY AND GEOLOGIC EVOLUTION

by

Justin Todd Germann

Bachelor of Science, University of North Dakota, 2017

A Thesis

Submitted to the Graduate Faculty

of the

University of North Dakota

in partial fulfillment of the requirements

for the degree of

Master of Science

Grand Forks, North Dakota

May
2021

Name: Justin Germann

Degree: Master of Science

This document, submitted in partial fulfillment of the requirements for the degree from the University of North Dakota, has been read by the Faculty Advisory Committee under whom the work has been done and is hereby approved.

DocuSigned by:
Sherry Fieber-Beyer
689BC90C95CB46B...
Dr. Sherry Fieber-Beyer

DocuSigned by:
Dr. Michael Gaffey
9884BEAF6CBA497...
Dr. Michael Gaffey

DocuSigned by:
Wayne Barkhouse
2A58DE608208413...
Dr. Wayne Barkhouse

This document is being submitted by the appointed advisory committee as having met all the requirements of the School of Graduate Studies at the University of North Dakota and is hereby approved.

DocuSigned by:
Chris Nelson
2E0AF088C733403...
Chris Nelson
Dean of the School of Graduate Studies

5/3/2021
Date

Title	VNIR Spectral Properties of Five G-Class Asteroids: Implications for Mineralogy and Geologic Evolution
Department	Space Studies
Degree	Master of Science

PERMISSION

In presenting this thesis in partial fulfillment of the requirements for a graduate degree from the University of North Dakota, I agree that the library of this University shall make it freely available for inspection. I further agree that permission for extensive copying for scholarly purposes may be granted by the professor who supervised my thesis work or, in her absence, by the Chairperson of the department or the Dean of the School of Graduate Studies. It is understood that any copying or publication or other use of this thesis or part thereof for financial gain shall not be allowed without my written permission. It is also understood that due recognition shall be given to me and to the University of North Dakota in any scholarly use that may be made with any material in my thesis.

Justin Todd Germann
May 3rd, 2021

ACKNOWLEDGMENTS

I would like to express my gratitude to my advisory committee - Dr. Sherry Fieber-Beyer, Dr. Mike Gaffey, and Dr. Wayne Barkhouse - for their support and guidance while working on the following research. Dr. Fieber-Beyer particularly deserves credit for suggesting research into the G-class asteroids, and Drs. Fieber-Beyer and Gaffey both deserve acclaim for their willingness to teach, mentor, and provide research opportunities for me throughout my graduate education.

I would also like to thank all of my classmates and friends in Space Studies - particularly Elias Holte, Steven Russel, Will Green, Peter Henson, and Caleb Strom - for their friendship and support throughout our time together in Space Studies. Finally, I'd like to thank my longtime partner Kalea Hoff and my parents for putting up with my bewildering excitement and at times complaints over small, rocky bodies within our solar system.

TABLE OF CONTENTS

Permission iv

Acknowledgments v

List of Figures ix

List of Tables xii

List of Equations xiii

Abstract xiv

Chapter I: Introduction 1

1.2: The Scientific SignifiCance of Asteroids and Meteorites 2

1.3: Purpose 3

1.4: Problem Statement 4

1.5: Thesis Structure 5

Chapter II: Literature Review 6

2.1: A Brief History of Asteroid Investigations 6

2.2: Asteroid Belt Structure 8

2.3: Observing Asteroids 10

2.3.1: Photometry 11

2.3.2: Spectroscopy 12

2.4: Crystal Field Theory 14

2.5: Space Weathering 16

2.6: Asteroid Taxonomies 18

2.6.1: CMZ and Bowell taxonomies 19
2.6.2: Tholen Asteroid Taxonomy 20
2.6.3: Barucci Taxonomy 22
2.6.4: Post ECAS Taxonomy 22
2.7: G-Class Characteristics 24
2.8: (1) Ceres - Evidence For Hydration 29
2.9: Investigations into Possible Surface Minerals of C-complex Asteroids 30
2.10: Phyllosilicates and Hydrated Minerals 32
2.11: Ammoniated Minerals 38
2.12 Meteorite Classification Review 43
2.12.1 Chondrites 44
2.12.2 Achondrites 49
2.12.3 Meteorite Spectral Features 51
Chapter III: Methods 56
3.1: Targets 56
3.2: Observations and Data Collection 57
3.3: Asteroid Spectrum Reduction 58
3.3.1: Starpack Creation 58
3.3.2: Atmospheric Corrections 60
3.3.3: Production of Nightly Average Spectrum 62
3.3.4: Spectral Normalization 63
3.4: Band Center Measurements 64

Chapter IV: Results 67
4.1: (1) Ceres 68
4.2: (13) Egeria 71
4.3: (19) Fortuna 74
4.4: (84) Klio 76
4.5: (130) Elektra 78
Chapter V Discussion 81
5.1: 0.7-μm Absorption Band 81
5.2: 0.95-μm Absorption Band 81
5.3: 1.14-μm Absorption Band 82
5.4: 1.25-μm Absorption Band 83
5.5: 1.4-μm Absorption Band 83
5.6: 1.9-μm Absorption Band 84
5.7: 2.3-μm Absorption Band 85
5.8: Geologic Interpretation of the Studied Asteroids 86
5.9: Possible Surface Minerals 90
Chapter VI: Conclusions 92
6.2: Future work 94
References 96

LIST OF FIGURES

Figure 1. The distribution of asteroids as a function of semi-major axis. The histogram shows areas of high asteroid density and low density even within the main asteroid belt - areas of low density are orbital resonances (IAU-MPC A, 2020). 8

Figure 2. Scatter plot of asteroids with semimajor axis vs. inclination. Modified to identify the approximate location of the 3:1, 5:2, 7:3, and 2:1 orbital resonances (Known as the Kirkwood Gaps) as well as the ν_6 secular resonance. (IAU-MPC, 2020). 9

Figure 3. Two-dimensional plot from Tholen's classification for 405 asteroids. Each asteroid is labeled with its taxonomic class, though the E, M, and P objects are labeled as X as they are spectrally degenerate. (Tholen, 1984). 21

Figure 4. S-complex zones for each asteroid on Band I Center – Band II center/BAR plots. 1A. Zone areas with generalized representation of mineralogical character for each subgroup. 1B. Location of the S-asteroids' subgroup relative to mineralogical zones (M. Gaffey et al., 1993). 23

Figure 5. Fundamental vibrational modes of simple molecules and ions. Arrows indicate direction of motion of each atomic component of the molecule; the length of the arrow indicates the magnitude of displacement. "+" indicates motion upward and "-" indicates motion downward, perpendicular to the plane of the page. (**a).** Linear XY_2 molecule such as CO_2. **(b)** Bent XY_2 molecule, such as SO_2 or H_2O. **(c)** Planar XY_3 molecule, such as carbonate ion. 31

Figure 6. Common tetrahedral phyllosilicate structure. Blue pyramids represent Si-O tetrahedron. O atom occupies each pyramid point and surrounds an Si atom. Sheets constructed of tetrahedron rings have an Si:O ratio of 2:5. Layers are constructed when a cation is bonded between sheets. Cation is commonly a metal, such as Fe^{+2}, Mg^{+2}, or Al^{+3}. 32

Figure 7. Octahedral sheet structure, SiO tetrahedron sharing edge. Octahedral sheet structures commonly incorporate a cation. 33

Figure 8. A. Phyllosilicate with 1:1 structure. B. Phyllosilicate with 2:1 structure. Purple layers indicate Octahedral structure, and green layers are tetrahedral structures. Yellow spheres are OH molecules or O atoms. Retrieved from *Mineralogy: Phyllosilicates* (1997). 34

Figure 9. Visible and near-infrared spectra of four hydrated carbonaceous chondrites. The hydrated carbonaceous chondrites lack intense features throughout the NIR due to concentrations of carbon. However, meteorites do show subtle features related to hydrated secondary minerals. Spectra gathered from NASA's PDS Geosciences Node Spectral Library. 53

Figure 10. A visible and near-infrared spectra of two anhydrous carbonaceous chondrites. Both meteorites exhibit two subdued features throughout the NIR, indicating concentrations of

olivine and pyroxene. Spectra gathered from NASA's PDS Geosciences Node Spectral Library..... 54

Figure 11. A visible and near-infrared spectra of eucrite ALHA76005. Intense 1000- and 2000-nm features are the result of pyroxene; the smaller feature redward of 1000-nm is produced by feldspar (indicated by the arrow). Spectra gathered from NASA's PDS Geosciences Node Spectral Library. 55

Figure 12. A visible and near-infrared spectrum of three ordinary chondrites. The pyroxene feature is present, though the 1000-nm feature is extended redward due to the presence of olivine. The extension of the 1000-nm feature is more intense in the L and LL groups as they contain a higher concentration of olivine. Spectra gathered from NASA's PDS Geosciences Node Spectral Library. 55

Figure 13. The final starpack used to model atmospheric extinction and features produced by HD32092. HD32092 was used as a solar analog for (13) Egeria. 60

Figure 14. A. Fitted continuum (red line) placed over an absorption feature in 13 Egeria spectrum (green line). B. Extracted raw curve (red line) with a ratioed polynomial curve fitted to the raw curve (green line). Determining at what point the polynomial raw curve's derivative is equal to zero determines where the tangent is zero and, therefore, the center of the polynomial fit..... 65

Figure 15. VNIR spectrum of (1) Ceres, produced by normalizing and combining SMASS II Visible CCD spectrum (R. P. Binzel et al., 1993), and near-infrared spectrum, observed and provided by Dr. Fieber-Beyer (personal communication, 2020). 68

Figure 16. The red line indicates the 8^{th} degree polynomial function calculated from (1) Ceres' spectrum. The R-squared value between the polynomial fit and (1) Ceres' spectrum was determined to ~0.9495, and the root mean squared error is ~0.005. 69

Figure 17. VNIR spectrum of (13) Egeria, produced by normalizing and combining SMASS II Visible CCD spectrum (R. P. Binzel et al., 1993), and near-infrared spectrum, observed and provided by Dr. Fieber-Beyer (personal communication, 2020). 71

Figure 18. The red line indicates the 21^{st} degree polynomial function calculated from (13) Egeria's spectrum. The R-squared value between the polynomial fit and (1) Ceres' spectra was determined to be ~0.9495, and the root mean squared error is ~0.005. Due to the steep and narrow 1.14- and 1.9-µm features, the polynomial fit was poor from approximately 1.2-1.5-µm, which contributed to the large root mean square error and poor R^2 value. 72

Figure 19. VNIR spectrum of (19) Fortuna produced by normalizing and combining SMASS-II Visible CCD spectrum (R. P. Binzel et al., 1993), and near-infrared spectrum observed and provided by Dr. Fieber-Beyer (personal communication, 2020). 74

Figure 20. The red line indicates the 14th degree polynomial function calculated from the spectrum of (19) Fortuna. The R-squared value between the polynomial fit and (19) Fortuna's spectrum was determined to be ~0.99472, and the root mean squared error is ~0.005. 75

Figure 21. VNIR spectra of (84) Klio, produced by combining and normalizing SMASS-II visible CCD data (R. P. Binzel et al., 1993), and IRTF SpeX NIR data acquired and calibrated and uploaded to the planetary data science system (Reddy & Sanchez, 2016). 76

Figure 22. The red line indicates the 12th degree polynomial function calculated from the spectrum of (84) Klio. The R-squared value between the polynomial fit and (84) Klio's spectrum was determined to be ~0.97913, and the root mean squared error is ~0.0055.. 77

Figure 23. VNIR Spectra of (130) Elektra, produced by combining the SMASS-II visible CCD data VNIR spectra of (84) Klio, produced by combining and normalizing SMASS-II visible CCD data (R. P. Binzel et al., 1993), and IRTF SpeX NIR data acquired and calibrated and uploaded to the planetary data science system (Reddy & Sanchez, 2016) 78

Figure 24. The red line indicates the 14th degree polynomial function calculated from the spectrum of (130) Elektra. The R-squared value between the polynomial fit and (130) Elektra's spectrum was determined to be ~0.993, and the root mean squared error is ~0.006. 79

LIST OF TABLES

Table 1. Band Center measurements of materials expected to exist on the surface of G-class asteroids. Electron transitions in Fe bearing minerals would indicate the presence of an oxidized phyllosilicate. OH-Vibrational transitions would be an indication of hydrated minerals such as phyllosilicates. 43

Table 2. General Lithologies of major chondritic meteorite groups. Modified from Ruben (1997). 48

Table 3. General lithologies of major achondritic meteorite groups. Modified from Rubin (1997). 51

Table 4. Features measured in 5 G-class asteroids all values are reported in microns (μm). Header indicates the features name, while the value listed in each objects row indicates the features center position. POSSIBLE meaning a feature may be present but was not measurable. 67

Table 5. Physical characteristics of the studied asteroids. 86

LIST OF EQUATIONS

Equation 1. A. Removing solar and atmospheric features from the target's reflectance spectrum for each wavelength. In this case, the standard star is equivalent in flux distribution to the Sun. B. Removing solar and atmospheric features from an asteroid's reflectance spectrum for each wavelength, when the standard star does not have a sun-like flux distribution. The local standard star must be divided by a solar analog star that was observed on the same night to remove discrepancies in the stellar flux distribution (Gaffey, 2002). 61

ABSTRACT

This study investigates the visible and near-infrared (VNIR) spectral properties (0.4-2.5-μm) of five Tholen G-class asteroids. Spectral features relating to hydrated Fe- or Mg-rich minerals have been identified at 0.7-μm, 0.95-μm, 1.4-μm, 1.9-μm, and 2.3-μm, while spectral features that may be related to CH or NH compounds were identified at 1.14-μm and 1.25-μm. (1) Ceres lacks features related to hydrated minerals and is spectrally disparate from the other four investigated asteroids. (13) Egeria, (19) Fortuna, (84) Klio, and (130) Elektra all exhibit at least two measurable features that may be related to hydrated minerals. (19) Fortuna, (84) Klio, and (130) Elektra each exhibit similar spectral slope and feature intensity, while (13) Egeria has a bluer slope and more intense features. These differences may be related to (13) Egeria's higher density, surface particle size, or the effects of space weathering.

CHAPTER I: INTRODUCTION

The protoplanetary disc that eventually developed into our solar system formed when a nebula consisting of interstellar dust and gases began to collapse inward and rotate due to the conservation of angular momentum (Cameron, 1962; Cassen & Moosman, 1981; Hoyle, 1960; Laplace, 1835; Shu et al., 1987). As the early solar system condensed, the inner rocky planets - Mercury, Venus, Earth, and Mars - acquired enough mass to kick-start geologic evolution (Kleine et al., 2002). The energy provided by gravity and radiometric isotopes within the condensing planets provided enough heat to metamorphose, melt, ionize, and differentiate the accreted material (Allégre et al., 1975; Papanastassiou & Wasserburg, 1975; Wetherill, 1980). These geologic processes produced the diverse planets and moons that populate our solar system today but also destroyed the original protoplanetary materials. However, small bodies that were condensing in conjunction with their planetary neighbors lacked the mass and energy required to sustain long-term geologic activity. While many asteroids and meteorites do show signs of thermal evolution system (Adams, 1974; Binzel et al., 1997; Mittlefehldt et al., 2003), most asteroids did not have the mass, isotope concentration, and insulation to sustain planetary-wide geologic cycles. Therefore, small bodies have remained relatively unchanged since the early solar system (Keil, 2000). These small bodies now reside in multiple relatively stable orbital repositories: the Oort Cloud, the Kuiper Belt, the Main Belt, and Jupiter's Trojans (Pfalzner et al., 2015). The asteroids located in the main asteroid belt between Mars and Jupiter collectively hold a mass of ~$4.008 \cdot 10^{-4}$ $M_{\oplus}$, or less than half a percent of Earth's total mass (Pitjeva & Pitjev, 2018). The material in the asteroid belt likely represents the only inner solar system material that was produced during the early solar system.

Through mineralogic and petrologic investigations of terrestrial rocks and minerals, it has

become apparent that the atomic repeating lattices, which compose minerals, can only manifest in a narrow pressure-temperature range (Bragg, 1937; Sorby, 1858). Meteorites, fragments of extraterrestrial bodies that intersect our planet's orbit and land on Earth, show that many mafic minerals found on Earth were being condensed from the protoplanetary disc and incorporated into accreting bodies (Keil, 2000; Rubin, 1997). To determine the surface composition of asteroids, planetary scientists use photometers and spectrographs to investigate the Sun's light reflected from those asteroids. It quickly became apparent that asteroids exhibit a broad range of reflected properties (Chapman et al., 1975; Gehrels, 1970; McCord et al., 1970). To easily organize and convey an asteroid's major spectral properties, asteroid taxonomic classifications were produced. Taxonomic classifications allow an asteroid's spectral or photometric properties to be described with a short title that efficiently conveys what unique properties were present in any given group or class. These taxonomic classes resemble classification schemes of stellar spectral types, though while stellar spectral classes convey information such as a star's temperature and luminosity, asteroid taxonomic classes are only reliable at conveying the spectral properties of any given asteroids and make no association to composition or physical properties. Details and histories of taxonomic classifications will be discussed in detail in Chapter 2.6.

1.2: THE SCIENTIFIC SIGNIFICANCE OF ASTEROIDS AND METEORITES

Since Earth's geologic processes have long since destroyed all the original protoplanetary material, meteorites are the only accessible and abundant material that provides information on the early solar system's composition (Patterson, 1956). However, meteorites alone impart very little information on their location of formation in the solar system. By determining a genetic link

between asteroids and meteorites, a greater understanding of the structure, temperature gradient, and chemical gradient of our system's protoplanetary disc can be ascertained.

Protoplanetary disks orbiting distant stars have been, and continue to be, a subject of interest (Fedele et al., 2018; Fukagawa et al., 2006; Kataoka et al., 2016), and we can learn a great deal about the solar system and planet formation by investigation of these infant systems. However, these observations can only serve as anecdotal evidence of the formation of our solar system. To better understand the solar system's granular chemistry and structure during its protoplanetary phase, we must study material formed during that period. Since the main belt asteroids, near-Earth asteroids, and their meteorite fragments are the most accessible and abundant deposit of ancient material, a substantial amount of research has been undertaken to relate asteroids to meteorites (Bottke et al., 2010; Burbine et al., 2001; Chapman, 1976; Fieber-Beyer and Gaffey, 2020; Gaffey and Gilbert, 1998; Noonan et al., 2019). The research presented in paper aims to investigate the VNIR spectra of Tholen G-class asteroids for absorption features related to minerals that are present in carbonaceous meteorites' spectra. While there have been studies attempting to relate the G-class asteroids to carbonaceous meteorites using spectral curve matching and broad features (Burbine, 1998; Hiroi et al., 1996), an investigation identifying, measuring, and relating subtle absorptions within the VNIR spectral ranges of G-class asteroids to possible surface minerals has not yet been completed.

1.3: PURPOSE

The Tholen G-class asteroids are classified from their eight-color photometric properties between 0.3- and 1.1-μm (Tholen, 1984). Since the establishment of the Tholen classification, spectrometers and photometers capable of resolving incident light with much greater fidelity and covering broader wavelength regimes have become common observational instruments. This

study will utilize spectroscopic observations in the visible and near-infrared spectral regime (VNIR) (0.4-2.5-μm). The VNIR spectral range was chosen for detailed analysis because likely C-complex surface minerals, such as phyllosilicates and mafic silicates, have been shown to produce compositionally diagnostic features that are relatively resistant to the effects of space weathering in the VNIR (Chilton et al., 2019; De Angelis et al., 2016; DeMeo et al., 2009; Ferrari et al., 2019; Gaffey, 2002; S. Gaffey, 1993; King et al., 1992). The VNIR spectral regime has also shown disparate features between the G-class asteroid population (Burbine, 1998; Fieber-Beyer, unpublished IRTF observations, 2020; Vilas & Sykes, 1996). This difference could be an indication of non-homogenous surface composition amongst the G-class asteroid population.

The first purpose of this study is to determine what spectral features are present and common amongst five G-class asteroids: (1) Ceres, (13) Egeria, (19) Fortuna, (84) Klio, and (130) Elektra. Then, a secondary purpose of this study will be to relate the spectral features observed in the asteroids to spectral features produced by common meteorite minerals. Dr. Tholen and many investigators following him have stressed that the asteroids belonging to a specific spectrographic classification are not necessarily composed of similar surface material (Tholen, 1984; Tholen & Barucci, 1989). This study will investigate the spectral and likely mineralogical diversity of the G-class asteroids by using instruments of much greater fidelity, utilizing the visible and near-infrared spectral regime.

1.4: PROBLEM STATEMENT

Recent spectroscopic analysis shows disparate features amongst the G-class asteroid population in the visible and near-infrared spectral range. This study aims to determine what spectral properties are common amongst the G-class asteroids in the visible and near-infrared

spectral ranges, while also attempting to interpret what surface minerals may be related to the spectral features present.

1.5: THESIS STRUCTURE

Chapter I introduces the broad topic of asteroid investigations, such as how meteorites are related and why studying asteroids is paramount in understanding the formation of the solar system. Section 1.3 details the two purposes of this study, as well as provides background into the G-class asteroids, and section 1.4 is a concise problem statement so the reader can clearly understand what issues this study aims to resolve. Chapter II provides an in-depth literature review detailing the broader investigations and observation techniques of asteroids, an overview of asteroid taxonomies, as well as an in-depth review of studies related to G-class asteroids, their relation to other C-complex asteroids, and investigations into possible surface minerals. The chapter ends with a brief review of meteorite classifications. Chapter III details the methods used to acquire and measure the VNIR spectra of all five asteroids investigated in this study. Chapter IV reports the results of the investigation and discusses the results and implications for disparity amongst the G-class, as well as the relations between the observed spectral features and possible surface minerals. Chapter V concludes the study by highlighting key findings in the asteroid spectrum and their implications for surface minerals and the G-class's geologic evolution. Chapter V ends with a brief commentary on important future work that should be undertaken for investigations into the G-class asteroids.

CHAPTER II: LITERATURE REVIEW

2.1: A BRIEF HISTORY OF ASTEROID INVESTIGATIONS

Ernst Chladni published a book in 1794 (Chladni, 1794) proposing the possibility that meteorites were derived from larger bodies in the solar system, rather than condensing as small chunks that periodically fell from space or clouds. At the time of publication, Chladni's explanations were largely ignored and occasionally ridiculed because no object capable of producing meteorites had been observed (McSween, 2006). In 1801, astronomer Giuseppe Piazza accidentally discovered asteroid (1) Ceres (Serio et al., 2002). Though originally thought to be a slow dim comet, it quickly became apparent that this object had orbital properties similar to that of a planet between Mars and Jupiter (Peebles, 2000). This discovery caused much excitement, as it solved the mystery of the missing planet, hypothesized to exist due to the now-defunct Titus-Bode law, which is a formulaic prediction of spacing between planets in any given solar system. The formula suggests that, extending outward, each planet should be approximately twice as far from the Sun as the proceeding planet. (McSween, 2006).

In next year, 1802, asteroid (2) Pallas was discovered and correctly identified as a second missing planet by Henrich Olbers while attempting to locate (1) Ceres (Peebles, 2000) - though, (2) Pallas was first recorded in 1779 by Charles Messier but was mistaken for a star (Bourtembourg, 2012). Olbers hypothesized that (1) Ceres and (2) Pallas were fragments of an early planet that had been destroyed by a massive impact. Due to these discoveries, Olbers agreed with Chladni that meteorites were fragments of the same exploded planet (Cunningham, 2017). The hypothesis that the asteroid belt is a remnant of a destroyed planet proved to be popular and was the consensus amongst astronomers and geologists throughout the 19th and the first half of the 20th century (Cunningham, 2017; McSween, 2006). The idea of a cataclysmic

event destroying an entire planet also aligned well with catastrophism, which was a prevalent geologic doctrine in the 18th and 19th centuries (Lutgens et al., 2012). The discovery of new asteroids continued with the discovery of (3) Juno and (4) Vesta by the end of 1807 (Peebles, 2000), and by the end of the 19th century over 400 asteroids had been identified (Pilcher, 1979). It had become apparent that an area between Mars and Jupiter contained a large population of small bodies with similar orbits, and by the 1850s this region was being referred to as the asteroid belt (Humboldt, 2015; Mann, 1853).

In December of 1891, Max Wolf was the first to discover an asteroid, (323) Brucia, using photography, which would quickly revolutionize asteroid identification. Continuing his exploration Wolf discovered 13 asteroids in 1892 alone, and it was not uncommon for him to identify multiple asteroids in a single exposure (Peebles, 2000). These technological advances led to the discovery of over 1200 asteroids between 1900 and 1950 (Pilcher, 1979). During the second half of the 20th-century, advances in optics, computer processing, and automation only increased the rate of asteroid identification. However, up until this point, asteroids remained moving specks of light and were regarded as the "vermin of the sky" because they were occasionally captured in the foreground of astronomical data (Binzel et al., 1991; Peebles, 2000). While photometric measurements of bright stars had been conducted since the mid-19th century, asteroids remained much too dim for photometric analysis. Though, in the 1950s, with the invention of Cs-Sb photocathodes, photometers quickly became useful for observing dim objects such as asteroids (Miles, 2007). This technology eventually led to the first compositional study of an asteroid in 1970 (McCord et al., 1970). Asteroids were no longer specks of light but physical bodies, with measurable compositions and unique features. With a greater understanding of an asteroid's photometric properties, it quickly became apparent that the

asteroid belt was not homogenous in composition, nor did it exhibit a composition that would be expected of a differentiated planet that had been destroyed. These discoveries shattered the century-old assumption that the asteroid belt was once a single planet. Planetary scientists instead adopted a model first proposed by Otto Schmitt in 1944 (McSween, 2006), which was that the asteroid belt is a region of halted planetary condensation mostly due to the gravitational forces between Jupiter and the Sun.

2.2: ASTEROID BELT STRUCTURE

Scenes from popular science fiction have led many to assume that the asteroid belt is a dense hostile zone, where at any time a protagonist's spaceship could be crushed between two city-sized asteroids. In reality, the asteroid belt is much less dense and chaotic; on average, the probability of impact between any two asteroids in the main belt is $2.85 \pm 0.66 \times 10^{-18}$ km^{-2} yr^{-1} (Farinella & Davis, 1992). The distribution of asteroids is not constant throughout the solar

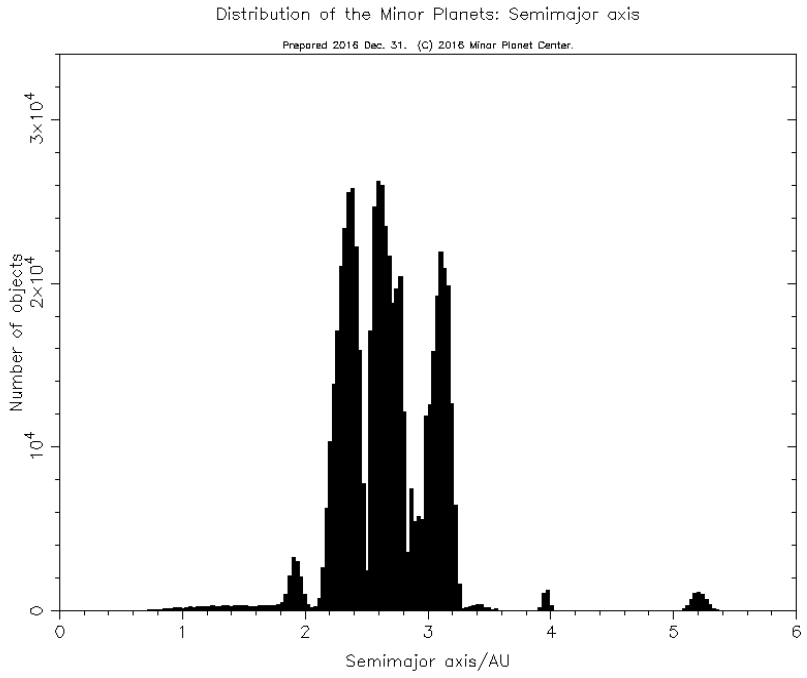

Figure 1. The distribution of asteroids as a function of semi-major axis. The histogram shows areas of high asteroid density and low density even within the main asteroid belt - areas of low density are orbital resonances (IAU-MPC A, 2020).

system, or even within the main belt. If one plotted a histogram of asteroids as a function of the semi-major axis (Figure 1), it becomes apparent that some orbits harbor large numbers of asteroids while other orbits are devoid of asteroids (Beatty, 1990; Wisdom, 1983).

The asteroid belt's structure is heavily influenced by gravitational resonances. Orbital resonances occur when the orbiting bodies regularly exert a gravitational influence on each other, commonly occurring when the body's orbital periods are related by a ratio of small integers. Jupiter's resonances have the greatest influence on the asteroid belt, and these resonances are identified by their orbital ratio (Figure 2). However, resonances with Saturn, and to an extent Mars, also influence the structure of the asteroid belt (Nesvorný & Morbidelli, 1998; Wisdom, 1983). When an asteroid enters an orbit with a resonance, it is much more likely to be ejected

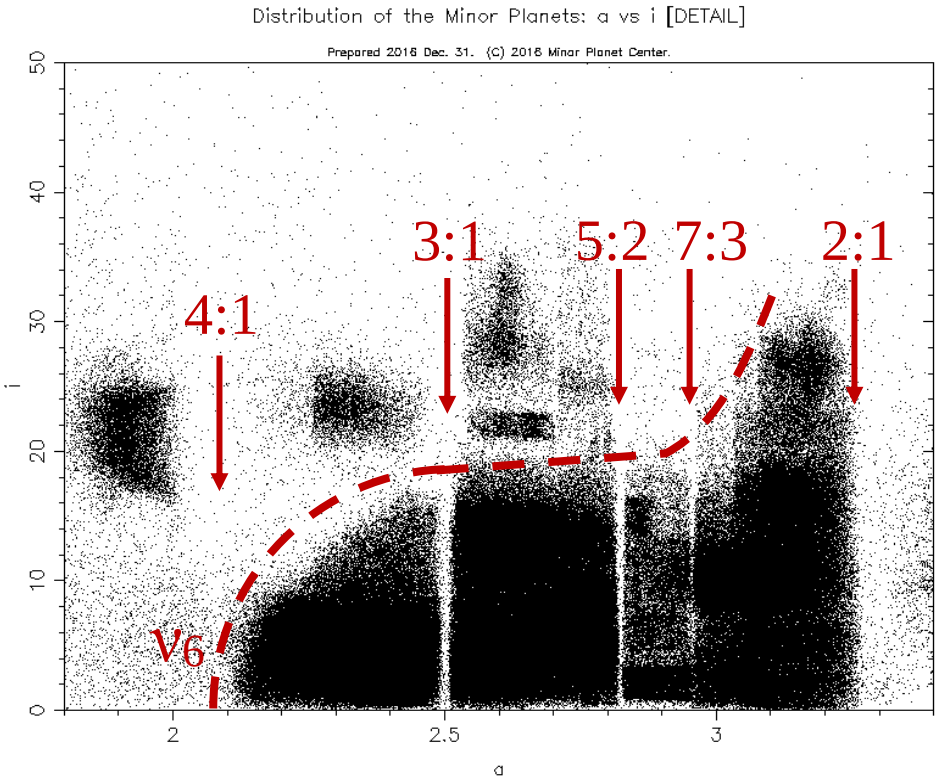

Figure 2. Scatter plot of asteroids with semimajor axis vs. inclination. Modified to identify the approximate location of the 3:1, 5:2, 7:3, and 2:1 orbital resonances (Known as the Kirkwood Gaps) as well as the ν_6 secular resonance. (IAU-MPC, 2020).

from that orbit, leading to areas being cleared of asteroids. These gaps were first observed by astronomer Daniel Kirkwood (1867). Kirkwood correctly identified Jupiter's orbital resonance as the reason why areas were relatively asteroid free, and today these gaps are referred to as the Kirkwood gaps (Ferraz-Mello, 1994; Wisdom, 1983).

Secular resonances also affect the structure of the asteroid belt. A secular resonance occurs when the orbital precession is synced with that of another body (Brouwer & Woerkom, 1950; Williams, 1969). Asteroids in secular resonances undergo gravitational perturbations, much like at orbital resonances, leading to an exclusion of objects within resonances. The most significant resonance is the ν_6 (Figure 2), which corresponds to the orbital precession of Saturn (Froeschle & Scholl, 1986).

2.3: OBSERVING ASTEROIDS

An asteroid in the main asteroid belt viewed from Earth will appear as a point of light indistinguishable from the stars in the background. However, asteroids move along, or near, the ecliptic plane as they orbit the Sun. Therefore, asteroids will appear to move at a faster pace and usually in a different general direction than the background stars do, much like the planets do. For this reason, the first asteroids were mistaken for missing planets. The first campaigns to identify asteroids were conducted by identifying bodies along the ecliptic plane and manually measuring the movement of the object over some time. With the advent of photography, asteroids and comets could be identified by taking wide-field images hours or minutes apart and identifying points that had moved a greater distance, or in a different direction, than the stars that surrounded them. Identifying and measuring an asteroid's orbit was the extent of asteroid investigations until the advent of highly sensitive photometers in the 1950s (Miles, 2007). With modern observational equipment and techniques, asteroids can be tracked with high precision for

hours, allowing for light from even faint asteroids to be collected at a signal-to-noise ratio, which is advantageous to scientific investigations.

2.3.1: PHOTOMETRY

Astronomical photometry is the process of measuring an observed object's light intensity. The light is collected via a telescope and measured using a photometer. Many modern photometers utilize charge-coupled devices (CCD), which convert light to energy by the photoelectric effect with a much greater light-gathering ability than photographic plates have (Beletic, 2005). Photometry collects light and measures the light intensity across the entire observed spectral range. The range of observed light can be controlled using an astronomical filter. Broadband filters are commonly used to collect light of a controlled spectral regime, such as the Johnson U, B, and V filters, though narrow-band filters can be used to investigate the intensity of an isolated spectral location. Photometric measurements can be used to identify spectral intensity disparities in an observed astronomical object. Photometry was and continues to be utilized to investigate broad spectral characteristics of astronomical objects, and the early asteroid taxonomies are based on photometric observations. Although the Tholen Taxonomy (1984) is based on eight color narrow-band photometric measurements, however, the current study will utilize spectroscopic measurements, which will be discussed in the following section.

Photometric measurements of a target can also be observed across an extended period. The photometric intensity can be plotted with respect to time to produce a photometric light curve. This process has been used in stellar observations to accurately measure flux output in variable stars (Brydon, 1940; Russel, 1912). In the last few decades, lightcurve observations have also been used to identify exoplanets using the transit method, which identifies a planet from the stars photometric measurements by identifying the drop in observed intensity as the

planet crosses between the star and the observer (Sasselov, 2003). When studying asteroids, or other minor bodies in the solar system, photometric lightcurves are an effective tool for modeling the orbital period, orbital axis, and general shape of minor bodies. Determining the time between lightcurve peaks gives an estimated period of rotation (Russel, 1906). The difference of brightness between the minima and maxima in the lightcurve of the asteroid can also be used as an indication of the shape of the asteroid. For example, an asteroid with a nearly spherical shape will have a less pronounced brightness difference, while an asteroid with a less spherical shape or with pronounced peaks, and valleys will cast more shadows and produce a lightcurve with a larger difference in reflected light intensity as the body rotates about its axis. Recent studies of photometric lightcurve properties using sophisticated models have been capable of producing detailed asteroid shape models (Kaasalainen & Torppa, 2001; Viikinkoski et al., 2017).

2.3.2: SPECTROSCOPY

Spectroscopy is a technique used to study the light intensity as a function of its wavelength, rather than to study the light across a spectral range like photometry does. The first astronomical spectrographic measurements were recorded by Isaac Newton in which he observed the distribution of sunlight after passing through a prism and realized that sunlight, and all white light, is composed of an entire array of colors (Newton, 1704). Early spectrographs utilized glass prisms to refract light into a spectrum. In the early 1900s, high-quality spectral gratings capable of refracting light of a lower intensity and with greater detail were introduced and have since been a main staple in astronomy investigations (Hearnshaw, 2014). An absorption spectrum is created when light interacts with low-energy matter, such as an interplanetary dust cloud or a planet's atmosphere (Carroll & Ostlie, 2017). Electrons associated with atoms in the low energy matter will absorb light of specific wavelengths, creating an absorption, or a drop in intensity, at

that wavelength's location in the spectrum. This study utilizes absorption spectroscopy in the visible and near-infrared spectral regime (0.4-2.5-μm) to determine surface mineral chemistry.

Another type of spectral investigation, ramen spectroscopy, involves the study of the interaction between radiation and molecular vibrations. Spectroscopy in the mid-infrared regime commonly produces features when a photon with energy levels in the mid-infrared is absorbed by a molecule. Ramen spectroscopy differs from absorption spectroscopy as the former measures the light scattering after an incident photon that has much greater energy than the vibrational energy of the target molecule. The incident photon loses part of its energy to the molecular vibrations, and the remaining energy is scattered, with reduced frequency. Therefore, the vibrational energy of the studied molecule can be determined by observing the difference in energy between the incident photon and the scattered photon. Although some vibrations can be measured accurately in both infrared and ramen spectroscopy, ramen spectroscopy is best at measuring the energy levels of symmetric vibrations of polar molecules (Larkin, 2011).

An emission spectrum is produced when ionized high energy matter emits electromagnetic radiation. Emission spectroscopy was first reported by Melvill (Melvill, 1756; Watson, 1952), who observed emission patterns after adding salts to alcohol burners. Unlike an absorption spectrum, which exhibits a decrease in flux, an emission spectrum will have emission lines, which are an increase of flux. Emission lines are caused by ionized electrons emitting photons to return to a neutral state. Much like absorption spectroscopy, the location of emission lines can be used to determine the chemistry of the body emitting electromagnetic radiation (Angström, 1855; Tennyson, 2005).

2.4: CRYSTAL FIELD THEORY

The absorption features observed in spectroscopic observations are the result of the light of a specific wavelength being absorbed or altered by matter with which the light interacts. The matter could include minerals on the surface of the asteroid, Earth's atmosphere, the solar atmosphere, or interplanetary dust and debris. When investigating an asteroid's spectrum, we are only interested in the interaction between the recorded electromagnetic radiation and the minerals on the asteroid. The reduction processes, detailed in Chapter III, aims to remove the information that may be related to the electromagnetic interactions with any other matter besides the surface of the asteroid.

All minerals are composed of an orderly, repeating, and predictable atomic lattice. Therefore, the interactions between ion electrical fields and the locations of outer electrons (those located in the d and f orbitals) should be predictable (Burns, 1970). Many mineral crystalline lattices are constructed from silicon-oxygen tetrahedrons (silicate minerals) (Bloss, 1971; Papike & Cameron, 1976). The oxygen anions located at the corners of the Si-O tetrahedron act as a ligand (the negatively charged ion within the lattice). The electromagnetic forces that surround each ligand combine with nearby charges to create a "field" that can incorporate an atom (Burns, 1970). In transition metals, electrons partially populate outer orbitals, specifically the d and f orbital shells. When a transition metal is incorporated into the ligand's field, it will share its outer electrons, creating an ionic bond. Since a transition metal's electrons only partially populate their outer orbitals, the electromagnetic influences of the ligands will dictate the position and energy level of the shared electrons (Burns, 1970). When incorporated into the atomic lattice, the transition metal has little control over its shared electrons; therefore, the position and energy level of the aforementioned electron can be greatly

affected by interactions with electromagnetic radiation (Burns, 1970). These interactions produce the “energy bands” observed in a spectrum when a shared electron is energized by absorbing the electromagnetic radiation, allowing that electron to move to a higher energy level. The electron will re-emit the absorbed energy as it moves back to a stable state. However, the re-admitted energy is rarely captured as it is expelled in random directions. If the expelled photon were collected, it would produce an emission band, however, since it is rarely expelled in the same direction as the reflected electromagnetic radiation, the collected spectrum will exhibit an absorption band at the expelled electron’s energy level.

The location, shape, and intensity of the absorption feature in the spectrum are directly related to the electron’s positions, and the electron’s position is dictated by the ligand’s electrostatic field, which is determined by the geometry in the atomic lattice (Burns, 1970). Many minerals have unique crystalline lattices, so the location and geometry of a spectrum’s absorption can be attributed to a specific mineral. However, many minerals share similar atomic structures and exhibit similar chemical bonds, therefore producing features with similar locations and geometries. For example, similar absorption features are viewed in phyllosilicate minerals, as many of the absorptions are produced by O-H vibrations (S. Gaffey, 1993; Hunt & Ashley, 1979; Hunt, 1979). A great deal of research has been conducted in identifying and attributing absorptions to specific electronic configurations. (Many of the studies on the crystal field properties of natural minerals before 1970 were compiled into a book by Burns [1970] with a second edition following [Burns, 1993]). The process of identifying minerals through absorption bands can be further complicated by impurities in the mineral. In natural minerals, these atomic lattices will contain atoms either as constituents or an impurities. Certain types of impurities or concentrations can deform the crystalline lattice, which will affect the mineral’s chemical and

physical properties as well as the mineral's spectral properties.

Currently, the VNIR spectral regime remains the best means of identifying key absorptions (Cloutis et al., 1986; Gaffey, 2002; M. Gaffey et al., 1993), as many features produced by diagnostic transitions metals (e.g., Fe^{2+}, Fe^{3+}, Ti^{4+}, etc.) and molecular species (e.g., H_2O, OH, CO_3, C-H, etc.) are produced in VNIR wavelengths (M. Gaffey et al., 1993). Many authors have identified that transition metals with oxygen bonds readily produce absorptions throughout the VNIR spectral regimes, and studies related to the current research will be discussed in Sections 2.6-2.9.

2.5: SPACE WEATHERING

Asteroids have remained relatively undisturbed from frequent cataclysmic impacts since the end of the late bombardment period (~4.1-3.8 Ga) (Gomes et al., 2005), though micrometeorites, solar wind, and galactic cosmic ray ion irradiation have continued to interact with the surfaces of atmosphere-less bodies since the formation of the solar system. Much of what we understand from space weathering was originally derived from lunar samples, as determining what physical alterations are occurring as a result of space weathering, for the most part, requires studying physical samples (Adams & Jones, 1970; Hapke, 1970; Noble et al., 2007; Pieters et al., 2000; Hiroi & Sasaki, 2001). The main process driving lunar space weathering is the production of nanophase Fe, which is produced from solar wind interactions with Lunar surface material (Keller & McKay, 1997). The nanophase Fe affects the reflectance spectra by making it appear reddened and darker in the VNIR wavelengths (Adams & Jones, 1970; Morris, 1976, 1978; Wells & Hapke, 1977; Hapke, 2001).

With asteroid flyby and probe missions such as NEAR-Shoemaker and Galileo, it was

confirmed that space weathering is also occurring on asteroid surfaces, though it was unclear to what extent space weathering was affecting remotely-sensed spectral data (Binzel et al., 2004; Chapman, 2004). Investigations using data from asteroid flyby and rendezvous missions showed that surface particle morphology and 1-μm band region of (433) Eros and (243) Ida did differ greatly from what was observed on the space weathered Lunar surfaces (Gaffey, 2010; Murchie et al., 2002). While more investigations into space weathering are necessary, space weathering of S-class asteroid material will likely affect the band slope and feature intensity; however, the band centers remain relatively unaffected (Brunetto et al., 2015; Gaffey, 2010).

In 2010, Hayabusa was the first mission to return asteroid surface grains to Earth. The spacecraft collected surface material from the S-class asteroid Itokawa and confirmed the expected space weathering effects, such as nanophase Fe and iron sulfide inclusions (Noguchi et al., 2011, 2014). While the Hayabusa mission provided insight into the space weathering processes taking place on S-class asteroids, much is still unclear about the effects space weathering has on C-complex (B-, F-, C-, and G-class) asteroids, which are the subject of this investigation. Two missions to collect surface samples of C-class near-Earth asteroids are currently underway. On Dec. 5, 2020, Hayabusa 2 returned samples of C-class asteroid (162173) Ryugo (Chang, 2020b), though currently no technical analysis of the space weathering effects on the collected grains has been published. The second mission, OSIRIS-REx, collected its sample in October 2020 (Chang, 2020a) and is scheduled to return a large sample of surface and near-surface material of C-complex asteroid (101955) Bennu in 2023.

Since the particle interactions known to cause space weathering are well understood, laboratory experiments simulating space weathering have been conducted on carbonaceous meteoric samples, to better understand how an asteroid's spectra may be affected by the effects

of space weathering. The results of artificially weathering carbonaceous meteorites have been relatively unclear and controversial; some report weak reddening trends in the spectral distribution (Lazzarin et al., 2006; Moroz et al., 1996), while others report bluing trends (Hiroi et al., 2004; Nesvorný et al., 2005). The production and destruction of C-H molecules from space weathering have also been investigated. Low energy photons interacting with carbonaceous material have been shown to produce new C-H molecules in the interstellar medium (Muñoz Caro et al., 2001), while high energy ion bombardment has been shown to destroy C-H bonds in interstellar materials (Mennella et al., 2003). It is still unknown whether both, one, or neither of these processes are occurring on C-complex asteroids, as the impact energy of the incident photon is still not fully understood (Brunetto et al., 2015). The ambiguity of the space weathering tests on carbonaceous meteorites may be the result of different types of carbonaceous meteorites being at different stages of the space weathering process. Therefore, the need for meteorites that are analogs to a known asteroid taxon is required to determine space weathering effects on that specific C-complex asteroid (Brunetto et al., 2015).

2.6: ASTEROID TAXONOMIES

Systems for relating asteroids with similar spectral properties and differentiating those with dissimilar properties became necessary as asteroid data collections grew. These systems are referred to as taxonomic classes. A taxonomic classification is an invaluable tool used across all scientific disciplines because such classifications concisely describe the properties of the studied subject whether it is a fundamental particle, animal, molecule, star, asteroid, etc. All asteroid taxonomies categorize the distribution of a photon's energy within some space parameter. There have been multiple asteroid taxonomic classification schemes introduced throughout the last half-century; many utilized different spectral distributions and are based on different criteria.

However, many taxonomic classifications share or have similar categoric labels. Similar labels may or may not have a connection from one classification to another creating confusion.

One-dimensional, visible color properties of asteroids have been studied since their discovery in the early 19th century (Cunningham, 2017). However, one-dimensional spectral characteristics are rarely relevant, as there are far too many minerals present on an asteroid's surface to confidently identify a compositional estimation, let alone determine specific chemical properties (Chapman et al., 1971). The first spectral classifications of asteroids utilized Johnson UBV photometry (Chapman et al., 1971; Gehrels, 1970). UBV photometry analyzes the U-B and B-V color indices to create a two-color plot, which separates asteroids into two groups, C (carbonaceous) and S (silicate). While C and S classification titles would appear to describe mineralogical properties, the two classes are only descriptive of the spectral characteristics and not chemical analysis (Tholen & Barucci, 1989).

Around the same time as Gehrel's (1970) UBV classification scheme, investigations using a greater number of filters were being conducted on individual asteroids. The first of such studies was conducted by McCord et al. (1970), which utilized narrow-band interference filters to measure the spectral reflectivity of Vesta from 0.3-1.1-μm. While this technique produced data with a fidelity high enough to conclude that Vesta's surface composition was similar to basaltic achondrites, such an observational technique was not deployed in large-scale surveys or useful for asteroids with faint magnitudes due to equipment limitations of the time.

2.6.1: CMZ AND BOWELL TAXONOMIES

One of the earliest taxonomic classification schemes that extended beyond the asteroid UBV properties was the CMZ classification (Chapman et al., 1975). The CMZ classification

analyzed broad-band radiometry near 10- and 20-μm, visible and near-infrared spectrophotometry, the B-V color, and the radiometric albedo of 110 asteroids. Chapmen concluded that more than 90% of the studied bodies fall into two broad compositional groups, designated by C and S, though a handful of objects were classified as U (unclassified). The CMZ taxonomy was later augmented to include 5 classes by Bowell et al. (1978). Bowell et al.'s updated version of the CMZ taxonomy used much of the same data as the CMZ taxonomy but added the U-B color and the BEND spectrophotometric parameter. Bowell et al.'s updated CMZ taxon studied 523 asteroids and classified 190 asteroids as type C, 141 as type S, 13 as type M, 3 as type E, and 3 as type R. Falling outside of the five classes, 55 asteroids were designated U.

2.6.2: THOLEN ASTEROID TAXONOMY

From 1979 to 1983, the eight-color asteroid survey (ECAS) was conducted (Zellner et al., 1985). ECAS utilized eight photometric bands between 0.3-1.1-μm to collect photometric data on 589 asteroids. ECAS was a massive success, as it collected spectral measurements of nearly 50% of the known asteroids at the time. The ECAS survey included a substantial number of targets and higher quality data than previously available; this data provided new means of asteroid taxonomic classification and spurred the second generation of taxonomic schemes.

The Tholen Taxonomy (Tholen, 1984) was produced by conducting principle component analysis of the ECAS data. Of all the asteroid photometric distribution collected from the ECAS survey, 95% contained two principle components, allowing most of the broad-band asteroid data to be classified from two absorption features, one in the ultraviolet and the other in the infrared. Fourteen asteroid classes were identified (A, B, C, D, E, F, G, M, P, Q, R, S, T, V) with the C-class being closely related to the B, F, and G classes. Plotting a 2-dimension dendritic diagram (Figure 3), the C-class core group exhibited three distinct separated populations that branched

out from the core; these branches were identified as the sub-classes of the C taxonomic classes. The C-class, and its subclasses, are low albedo objects that exhibit an ultraviolet feature blueward of 0.4-μm but lack a secondary infrared feature redward of 0.4-μm.

The G-class, the taxonomic class of interest in this study, is established in Tholen's Taxonomy. The G-class is differentiated from the C-class by having a steeper ultraviolet feature, likely related to Fe^{2+}-Fe^{3+} iron charge transfer in surface minerals (Feierberg et al., 1985). While compositional speculation has been proposed for taxonomic classifications, the Tholen Taxonomic class is based solely on observed spectral properties, not on an inferred composition. An asteroid belonging to the G-class only means that its spectral properties in the ECAS survey were measured to be within the limits of the G-class. While it may be possible that many G-class asteroids do share a common composition, that does not mean that all G-class objects are of the same composition (Tholen, 1984).

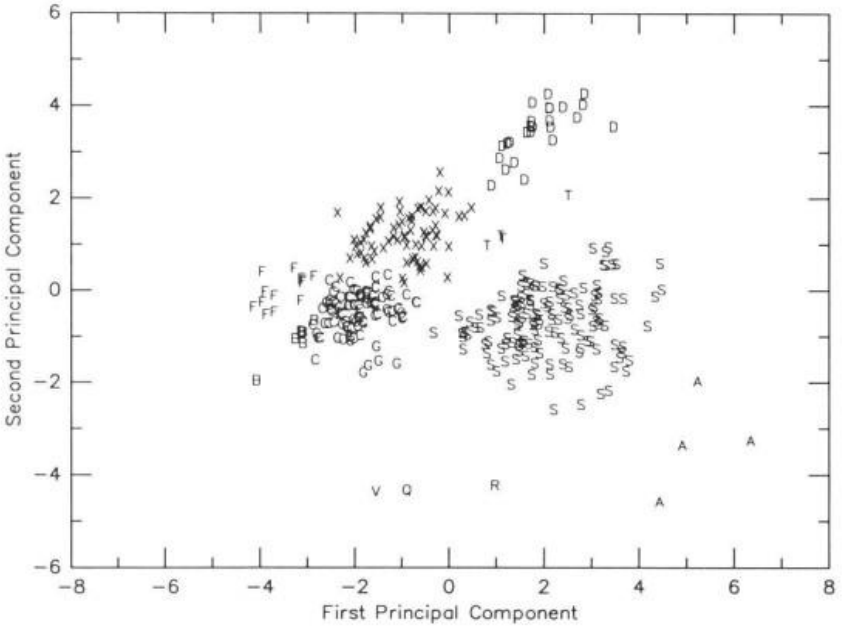

Figure 3. Two-dimensional plot from Tholen's classification for 405 asteroids. Each asteroid is labeled with its taxonomic class, though the E, M, and P objects are labeled as X because they are spectrally degenerate (Tholen, 1984).

2.6.3: BARUCCI TAXONOMY

Barucci et al. established a second ECAS-based taxonomy in 1987. Barucci's taxonomy utilized G-mode analysis (Coradini et al., 1977), a statistical method to automatically classify a set of *N* samples with *M* variables. The Barucci Taxonomy identified the same nine groups as Tholen's taxonomy did, though the C class is subdivided into three groups based on their albedo rather than principle component analysis (Barucci et al., 1987).

2.6.4: POST ECAS TAXONOMY

There have been multiple influential and broadly accepted asteroid taxonomies since the ECAS and IRAS-based taxonomies of the 1980s. The following taxonomies pioneered techniques and utilized data that are relevant to this study, as well as introduced nomenclature that will be referenced later in later sections. However, these taxonomies are not directly related to this study. Therefore, the following section will only briefly cover the notable taxonomies.

The Tedesco Taxonomy utilized three components - the ECAS ν-χ band, the Johnson U-V color, and IRAS Albedo data. Tedesco's taxonomy used a classification algorithm that placed 96% of the 357 sampled asteroids into 11 taxonomic classes. The classification relied on examining stereo pairs of two-dimensional plots containing three-dimensional data. If any given asteroid fell within two different classification clusters, the nomenclature would indicate the discrepancy by having a multiple letter designation (Tedesco et al., 1989).

By the 1990s, it had become apparent that the S-class was spectrally diverse and included several distinct sub-types representing a diverse range of mineral mixtures and chemistries. Gaffey et al. (1993) devised a subclassification of the S-class asteroids to further distinguish the spectral variations within the S-class. Using the asteroid's visible to near-infrared spectral

parameters, seven subclassifications [S(I) – S(VII)] were produced. The classification relies on the properties of the two silicate bands (Band I and Band II) and the ratio of Band II's area divided by Band I's area (BAR). Figure 4 details each subclassification's location on the Band I center and the Band II/BAR plots.

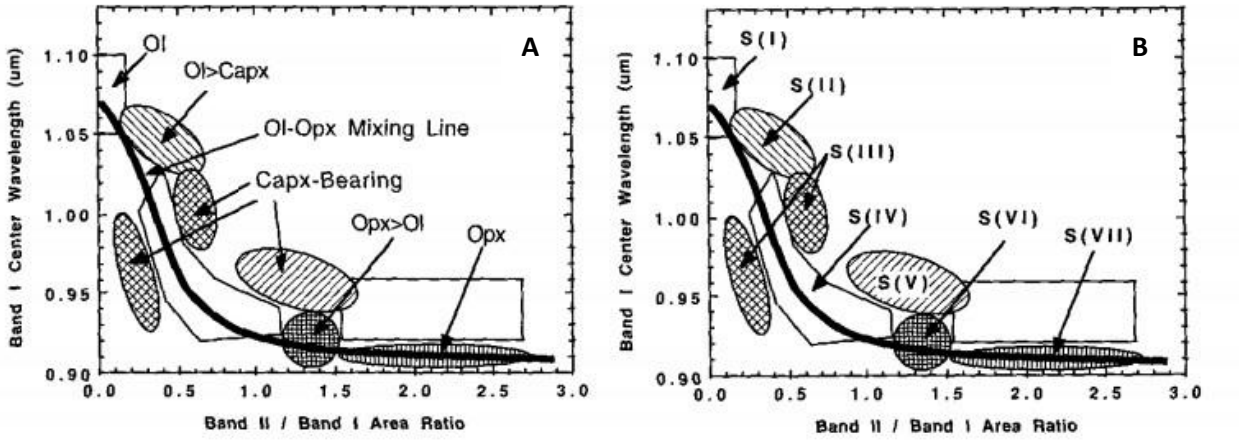

Figure 4. S-complex zones for each asteroid on Band I Center – Band II center/BAR plots. 1A. Zone areas with generalized representation of mineralogical character for each subgroup. 1B. Location of the S-asteroids' subgroup relative to mineralogical zones (M. Gaffey et al., 1993).

The Small Main-Belt Asteroid Spectroscopic Survey (SMASS II) was initiated by MIT in 1991 (Binzel et al., 1993; Xu et al., 1995), and collected CCD spectra from 0.4-1.1-μm of 1447 asteroids. Bus and Binzel (2002) produced the Bus taxonomy, utilizing the SMASS II data. The Bus taxonomy consists of the S-, C-, and X-groups, which were commonly identified in preceding taxonomies. These three groups are further divided into 26 classes - 13 single letter classes (A, B, C, D, K, O, Q, R, S, T, V, L, and X) and 13 multi-character classes with intermediate spectral characteristics (Cb, Cg, Cgh, Ch, Ld, Sa, Sk, Sl, Sq, Sr, Xc, Xe, and Xk). The Bus Taxonomy inherited its framework from the Tholen Taxonomy and maintained much of the same structure and labels, as the authors intended it as a successor rather than an entirely new

system. The taxonomy uses principle component analysis and the spectral distribution slope to identify unique spectral components for each taxon.

While much of the Tholen Taxonomy framework was preserved in the Bus Taxonomies, multiple taxonomic classes were modified, removed, or separated. The modification that is most relevant to this study is the removal of the Tholen G-class, (1) Ceres was instead classified as a C-class under the Bus taxon criteria, and (13) Egeria, (19) Fortuna, (84) Klio, and (130) Elektra were classified as a Ch-class. The members of the Cgh- and Ch-classes are differentiated from the C-class by the presence of a 0.7-μm feature, which is generally attributed to hydrated minerals. The Bus taxonomy was based only on spectral absorption features, as they are least affected by space weathering (Gaffey, 2002) and are one of the most reliable indicators of an asteroid's surface composition. However, it should be emphasized that the Bus Taxonomy is wholly based on spectral properties and should not be associated with surface composition.

In the early 2000s, asteroid spectral measurements extending into the near-infrared became more accessible as new telescopic instruments such as SpeX (Rayner et al., 2003) were introduced. An updated version of the Bus taxonomy was introduced by Demeo et al. (2009) to utilize the NIR spectral measurements. The extended Bus Taxonomy contained 24 classes, removing the Ld-, Sk-, and Sl-classes and creating the Sv-class. Much of the structure and classification criteria remained the same between the Bus and Extended Bus taxon, but the principle components were extended to include 41 data points between 0.4 and 2.5-μm.

2.7: G-CLASS CHARACTERISTICS

A dynamical study of 2355 main-belt asteroids to determine the total theoretical fragment delivery efficiencies through either the 3:1 mean motion resonance or the ν_6 secular resonance

was completed by Farinella et al. (1993). It was determined that a significant proportion of near-Earth asteroids and meteorites could be derived from very few bodies in the asteroid belt, with most material being supplied by large asteroids near large resonances. Out of the 11 most likely asteroids to supply material to Earth-crossing orbits, three were G-class asteroids: (1) Ceres, (13) Egeria, and (19) Fortuna, which is a significant revelation, because, even though the G-class is a small class, it is likely that Earth's meteorite catalog does contain meteorites deriving from G-class asteroids. Therefore, having a comprehensive understanding of G-class mineralogy and spectral properties will be paramount in relating carbonaceous meteorites to parent asteroids.

The study most relevant to this investigations was authored by Burbine (1998), in which he compared the VNIR spectral properties of three G-class asteroids ([1] Ceres, [13] Egeria, and [19] Fortuna) to the CM chondrites to determine if G-class asteroids were the parent asteroids to CM-chondrites. Burbine produced VNIR spectra (~0.4-2.5-μm) for each asteroid by combining and normalizing the ECAS survey (Zellner et al., 1985) and the 52-color survey (Bell et al., 1995), as well as utilizing CCD spectra for (13) Egeria and (19) Fortuna when only comparing visible wavelengths. (1) Ceres' spectrum exhibited a weaker UV feature when compared to (13) Egeria and (19) Fortuna; (1) Ceres also lacked a 0.7-μm feature, which is most commonly associated with hydrated minerals. It was determined that (1) Ceres was not spectrally analogous to any CM-chondrites included in Burbine's (1998) study. However, it was determined that (19) Fortuna's VNIR spectrum matched well with the spectra of CM-chondrite Murchinson and LEW 90500, though (19) Fortuna's UV feature is slightly weaker than both meteorites. (13) Egeria's UV spectrum matched well with LEW 90500 bulk powder, though (13) Egeria had a slightly bluer slope in the near-infrared wavelengths. The 0.7-μm band center of LEW 90500 had a slightly longer wavelength (~0.72-μm) than (13) Egeria did (~0.67-μm) and (19) Fortuna (~0.67-

μm). Burbine concluded that the presence of a 0.7-μm absorption feature indicated that (13) Egeria and (19) Fortuna had CM-like compositions, though the wavelength disparities between the asteroids and meteorites studied indicated a difference in phyllosilicate chemistries. Burbine also stressed that the 0.7-μm feature is not uncommon in low albedo asteroids. Surveys indicate that approximately one-half (Barucci et al., 1997) to one-third (Sawyer, 1991) of C-class asteroids contain a 0.7-μm feature. Therefore, the link between CM-chondrites and (13) Egeria and (19) Fortuna could not be inferred solely by the identification of the 0.7-μm feature. Burbine ultimately concluded that fragments of (13) Egeria and (19) Fortuna were likely to be classified as CM-chondrites, though it was highly unlikely that (13) Egeria and (19) Fortuna were the parent asteroids of all CM chondrites.

The 52-color survey and the ECAS survey data utilized in Burbine's (1998) study lacked the distribution detail that is capable of being produced by modern infrared spectrographs such as SpeX (Rayner et al., 2003). Due to instrumental limitation, only the broad 0.7-μm feature was identified in (13) Egeria's and (19) Fortuna's spectra, and much of the analysis relied on curve matching, which can be unreliable for compositional investigations as it has been reported that an asteroid's NIR spectral slope can be affected by both space weathering (Gaffey, 2010; Sanchez et al., 2012) and grain size (Adams & Filice, 1967). Even though Burbine (1998) did test multiple meteorite grain sizes to mitigate the effects of space weathering, absorption feature analysis is still regarded as a more reliable indication of surface mineralogy (Gaffey, 2002). Even though Burbine (1998) could not conclusively determine whether CM chondrites and G-class asteroids were linked, it did show that within the G-class there are large enough spectral disparities in the VNIR to indicate that some G-class asteroids may be promising analogs to some CM-chondrites while other G-class asteroids may not be. The results reported in this

investigation will build upon Burbine's (1998) findings by identifying and measuring subtle absorptions not identified by Burbine in (1) Ceres, (13) Egeria, and (19) Fortuna, as well as two other asteroids - (84) Klio and (130) Elektra - and determine what minerals may be related to the features identified.

Hiroi et al. (1993) conducted a study heating CM-chondrite material to determine if the C, G, F, and B asteroids represented a thermally metamorphosed analog to the CM-chondrites. The study relied on curve matching the heated CM-chondrite material's UV feature to the UV feature of the studied asteroids. Hiroi et al. concluded that virtually all large C, G, B, and F asteroids are thermally metamorphosed to some degree and that the G- and C-class asteroids were most likely heated between 600° and 1000° C.

Hirio et al.'s conclusion was later refuted by Vilas and Sykes (1996), as Hirio et al.'s study only relied on the UV feature strength and did not consider other spectral features. Vilas and Sykes proposed that many low albedo asteroids could not be representative of highly metamorphosed asteroids, as the 0.7-μm feature would disappear when CM-chondrites were heated to temperatures greater than ~400° C. Since many C-class asteroids (and their corresponding subclasses G, B, and F) contained the 0.7-μm feature, these asteroids could not have been heated to the 600° - 1000° C temperature as suggested by Hiroi et al. (1993). Rather than the C-, B-, G-, and F- asteroids represent "cores" and "mantle" portions of metamorphosed parent bodies, Vilas and Sykes concluded that the C-, B-, G-, and F- asteroids instead contain objects with two separate histories. The first history involves large asteroids (diameters > ~50 km), which consistently exhibited the 0.7-μm feature and likely represent large homogenous rubble piles, which were produced by repeated collisional destruction while still being gravitationally bound. Smaller asteroids have a different history. They are likely ejected

fragments of large parent asteroids, which was indicated because small asteroids (diameters < ~ 50 km) tended to be more diverse in spectral properties, indicating that they were representative of compositionally different units exposed from the parent asteroid's interior. The dichotomy of spectral properties between small and large diameter asteroids was later affirmed by Hiroi et al. (1996) and Fornasier et al. (2014), who identified a strong correlation between C-complex asteroids' sizes and the presence of hydrated features.

The 0.7-µm feature has been of interest to those studying C-complex asteroids, as it is commonly associated with $Fe^{2+} \rightarrow Fe^{3+}$charge transfer in oxidized iron minerals, which are a result of aqueous alteration (Calvin & King, 1995; Vilas, 1994). This feature has also been identified in laboratory reflectance spectra of terrestrial serpentines and chlorites (King & Clark, 1986). As shown by Vilas and Sykes (1996), the 0.7-µm feature will diminish when the material undergoes heating > 400° C. The presence of the 0.7-µm feature indicates that the temperatures reached by the minerals now at the surface of the asteroid were hot enough to mobilize water, but not hot enough to cause melting or recrystallization of the surface material. Low temperature (< 320 K) alterations of primary mafic minerals driven by liquid water likely produced hydrated minerals such as phyllosilicates, sulfates, oxides, carbonates, and hydroxides. The energy source for heating and mobilizing water in primordial asteroids was likely the ^{26}Al decay (Fornasier et al., 2014).

The 3.0-µm absorption feature is also commonly associated with water molecules and OH incorporated in crystalline lattices (Berg et al., 2016; Feierberg et al., 1981; Jones et al., 1990; Lebofsky, 1978, 1980; Milliken & Rivkin, 2009; Vilas, 1994). A strong correlation between the presences of the 0.7-µm band and the 3.0-µm band has been identified, indicating that both features strongly suggest the presence of hydrated minerals and/or aqueous alteration

(Fornasier et al., 2014; Vilas, 1994). Approximately 65% of the C-complex asteroids contain features associated with hydrated minerals (Fornasier et al., 2014), though the distribution of hydrated features amongst the C-complex is not uniform. Vilas (1994) identified asteroids with hydrated features using data from the ECAS survey, two CCD data sets, and IR photometry. Vilas determined that the abundance of hydration increases from P → B → C → G class. There was a linear correlation identified between mean albedos and percentages of asteroids testing positively for hydration in low-albedo asteroid classes. It was also determined that asteroids testing positive for hydration features are concentrated between 2.6 and 3.5 AU, which is the range dominated by the C-complex asteroids. Vilas's conclusion was later affirmed by Rivkin et al. (2003) and Fornasier et al. (2014), who determined that Vilas's aqueous alteration gradient (P→B→C→G) held true when including more asteroids. Fornasier et al. also noted that all six G-class asteroids included in his study contained hydrated features, though a smaller heliocentric range of 2.3 – 3.1 AU was identified for aqueously altered asteroids when compared to the range suggested by Vilas (1994). It should be mentioned that neither (1) Ceres nor (2) Pallas was included in either study, as their large sizes are atypical of the main-belt population.

2.8: (1) CERES - EVIDENCE FOR HYDRATION

Dwarf planet (1) Ceres, the largest body in the asteroid belt, has been the subject of many investigations since it was first discovered in 1801. In the mid to late 1970s, its 3.0-µm absorption feature was identified and correlated to hydration (Lebofsky, 1978, 1980). Feierberg et al. (1981) correlated the 3.0-µm band in (1) Ceres' spectrum to either free water ice or interlayer water molecules in clay minerals and determined that (1) Ceres' surface has a much higher concentration of clay minerals when compared to 2 Pallas and 324 Bamberga. Feierberg et al. also speculated that the presence of hydrated salts and ices are responsible for (1) Ceres'

relatively high albedo and contribute to the intensity of the 3.0-μm feature. However, more recent studies, which will be discussed in the following section, have instead suggested that hydrated minerals, such as phyllosilicates, have a greater contribution to the 3.0-μm band.

2.9: INVESTIGATIONS INTO POSSIBLE SURFACE MINERALS OF C-COMPLEX ASTEROIDS

By the end of the 20th century, the vital role spectroscopy would have in remotely investigating the geochemistry of other bodies in our solar system had become apparent, and a need for spectral measurements of geologic materials arose. S. Gaffey (1993) conducted a study compiling and investigating spectroscopic measurements in the UV, VIS, and NIR ranges of a diverse array of geologic minerals and molecular components. The study not only detailed at what wavelengths materials produce absorption features but also documented the specific atomic mechanism causing the absorption. The study investigated compounds of interest to planetary scientists - such as ices, volatiles, and organics - but also investigated mineral assemblages - such as hydrates, hydroxides, oxides, silicates of all varieties, carbonates, sulfides, evaporates, and metals. The relevant results of S. Gaffey's study will be detailed in the following chapters and will be included in Table 1. One major motif of S. Gaffey's study, though, is that many of the features observed in the spectra of geologic material are produced by the same molecules and components within different materials. These molecules most commonly include ions of transition elements (such as $Fe^{2+ \text{ or } 3+}$, Al^{2+}, Mg^{2+}, and Mn^{2+}) and molecules included in multiple types of materials (such as NH, CH, OH, SO, CO, etc.) The listed atoms, molecules, and more are commonly responsible for producing absorptions, as they readily promote electron transition between atoms in the crystal lattice, such as $Fe^{2+} \rightarrow Fe^{3+}$ charge transfer producing the 0.7-μm feature (Vilas & Sykes, 1996), as well as commonly exhibit vibrational transitions (Figure 5). Vibrations of any given frequency absorb light of the same frequency. Since frequency is

directly related to wavelength ($\nu = c/\lambda$), the frequency dictates the location of the absorption feature in the spectrum. Several factors affect the vibrational frequencies, such as cation and anion valence, the mass of atoms affected, bond strength, and bond type. Therefore, even though an absorption may be produced by the same type of molecular activity, the absorption may appear at slightly different wavelengths depending on the material being investigated.

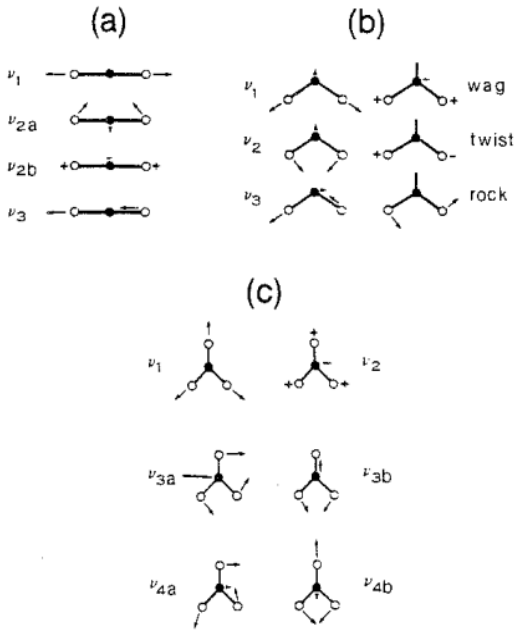

Figure 5. Fundamental vibrational modes of simple molecules and ions. Arrows indicate direction of motion of each atomic component of the molecule; the length of the arrow indicates the magnitude of displacement. "+" indicates motion upward and "-" indicates motion downward, perpendicular to the plane of the page. **(a).** Linear XY_2 molecule such as CO_2. **(b)** Bent XY_2 molecule, such as SO_2 or H_2O. **(c)** Planar XY_3 molecule, such as carbonate ion.

Figure and caption retrieved from S. Gaffey (1993).

Spacecraft missions such as DAWN, OSIRIS-Rex, and Hayabusa have refreshed the interest of the planetary science community in investigating the spectral properties of possible surface minerals on C-complex asteroids. Much of the scientific community has identified phyllosilicate minerals to be responsible, at least in part, for the hydration features identified in C-complex asteroids.

2.10: PHYLLOSILICATES AND HYDRATED MINERALS

Phyllosilicate minerals encompass a variety of chemistries and chemical endmembers - including serpentine, chlorite, hydroxides, and complex clay minerals. Phyllosilicate minerals are composed of two types of atomic "sheets" tetrahedral and octahedral. Tetrahedral sheets are constructed of SiO_4 tetrahedra that share three corners with neighboring tetrahedra. Tetrahedral sheets have a general formula of Si_2O_5 (Figure 6). However, Al^{3+} and Fe^{3+} may substitute for Si, creating charge imbalances. Octahedral sheets are constructed of octahedra of oxygen and hydroxyl ions linked laterally and sharing edges. The centers of octahedra are commonly occupied by a cation, which can dictate the mineral type (Figure 7).

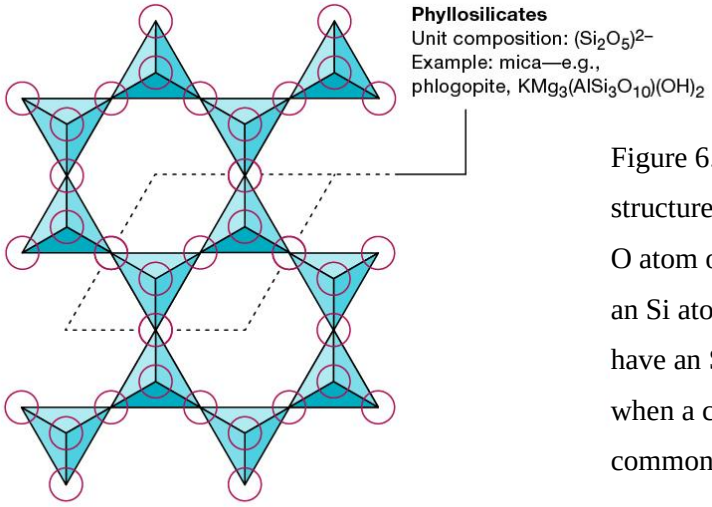

Figure 6. Common tetrahedral phyllosilicate structure. Blue pyramids represent Si-O tetrahedron. O atom occupies each pyramid point and surrounds an Si atom. Sheets constructed of tetrahedron rings have an Si:O ratio of 2:5. Layers are constructed when a cation is bonded between sheets. Cation is commonly a metal, such as Fe^{+2}, Mg^{+2}, or Al^{+3}.

Figure retrieved from ("Phyllosilicate," 2018).

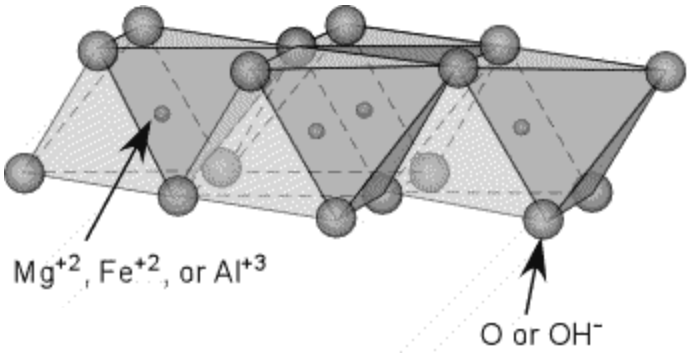

Figure 7. Octahedral sheet structure, SiO tetrahedron sharing edge. Octahedral sheet structures commonly incorporate a cation.

Figure retrieved from (Klein et al., 1993).

Tetrahedral and octahedral sheets can be joined by sharing apical oxygen and hydroxyl groups. A 1:1 layer exists when a tetrahedral sheet is bonded with an octahedral sheet (Figure 8a); a 2:1 layer occurs when an octahedral sheet is between two tetrahedral sheets (Figure 8b). These layers can then be bound to another layer group either through Van der Waals forces or interlayer cation attraction. When sheets contain a large charge imbalance, due to substituted cations in the sheet structure, it is more likely for sheets to be bonded by interlayer cations or through other polar molecules, such as NH^{3+} (S. Gaffey, 1993).

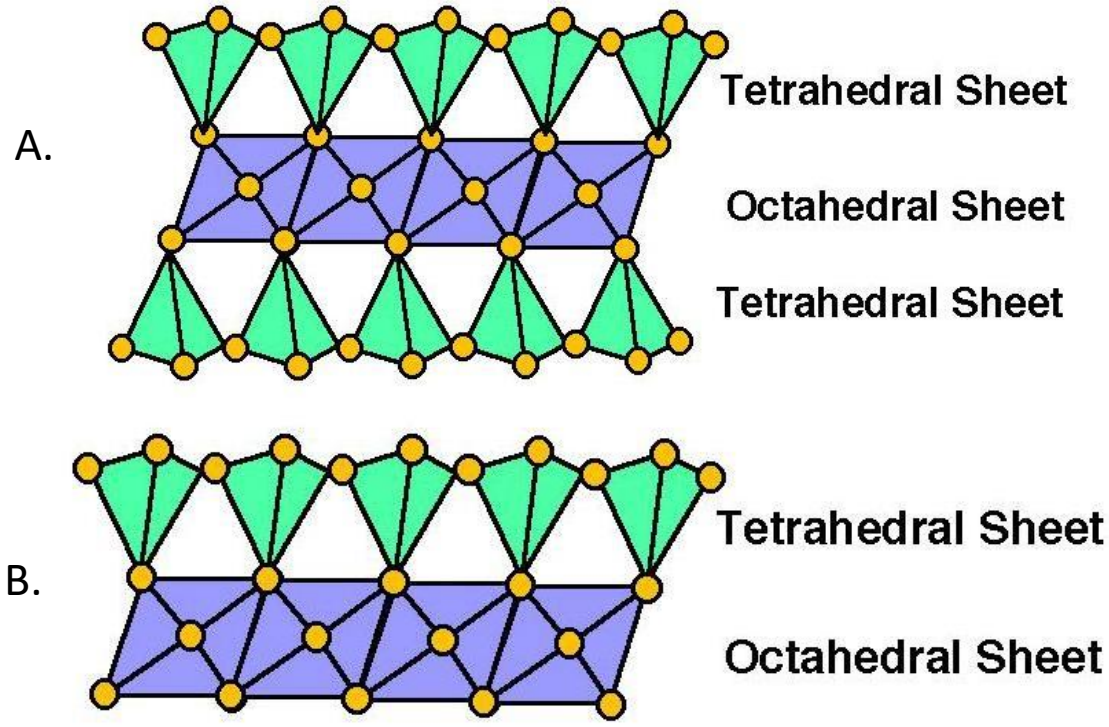

Figure 8. A. Phyllosilicate with 1:1 structure. B. Phyllosilicate with 2:1 structure. Purple layers indicate Octahedral structure, and green layers are tetrahedral structures. Yellow spheres are OH molecules or O atoms. Retrieved from *Mineralogy: Phyllosilicates* (1997).

Most tetrahedral phyllosilicate crystal lattices contain an OH^- (hydroxyl) ion at the center of the tetrahedra ring that composes the sheets. The sheets are then bonded together by an interlayer of cations, commonly Fe^{+2}, Mg^{+2}, or Al^{+3}. The presence of the OH^- within the phyllosilicate crystalline lattice, and its ability to harbor interlayer H_2O molecules, is the reason for its association with the 3.0-µm feature (Jones et al., 1990). As stated earlier, the 0.7-µm band is also associated with $Fe^{2+} \rightarrow Fe^{3+}$charge transfer in oxidized iron minerals. This process can occur readily in oxidized Fe-rich phyllosilicates (Vilas & Gaffey, 1989). Therefore, the presence of the 3.0- and 0.7-µm bands is considered a clear indication of hydration and a likely phyllosilicate mineral. The absence of the 0.7-µm feature while the 3.0-µm feature is present has

been observed, most notably in (1) Ceres. Fornasier (2014) suggested that this situation could occur when the surface minerals are either iron-poor, all Fe^{2+} has been converted to Fe^{3+}, or the minerals have experienced mild heating (400° C < T < 600° C) after aqueous alteration, which had also been documented by Vilas and Sykes (1996). While the 3.0-µm feature was not included in the spectral distribution range investigated in the current study, it is still an important factor to consider when attempting to identify possible surface minerals.

A study on the spectra of altered terrestrial geologic material was completed by Hunt and Ashley (1979). Their investigation's purpose was to determine if VNIR spectroscopy was reliable at detecting and identifying clay minerals. Two general types of transitions were identified in the sample minerals that reliably produced absorptions, electronic transitions in iron-bearing minerals, and vibrational transitions in clay and water-bearing minerals. Electronic transitions in iron-bearing minerals produced absorptions at 0.43-, 0.65-, 0.85-, and 0.93-µm, while vibrational transitions of clay and OH/H_2O bearing minerals produced features at 1.4-, 1.75, 1.9, 2.2, and 2.35-µm.

An investigation to understand the effects heating has on phyllosilicate minerals was conducted by Ostrowski et al. (2010). The study focused on continuum plots (1.0-1.75-µm slope against the 1.8-2.5-µm slope), as C-asteroid spectra are relatively featureless. It was determined that heating kaolinite and montmorillonite to ≥ 700 °C would move their continua slopes into the C-asteroid region, whereas heating chlorite and serpentine to the same degree would move their slopes to the CM chondrite region. Ostrowski et al.'s results indicate that the CM chondrites and C-class asteroids (excluding [1] Ceres) both represent excavated interior samples, which agrees with the results of Vilas and Sykes (1996). C-class asteroids are akin to dehydrated montmorillonite and CM chondrites, representing dehydrated serpentine and chlorite, both of

which have been previously identified in CM chondrites (Akai, 1988; Cloutis et al., 2011; Lauretta et al., 2000).

Vilas & Gaffey (1989) investigated 16 low albedo asteroid spectra between ~0.4-1.0-μm for absorption features. Absorption features were compared to the absorption features produced by CM2 and CI1 carbonaceous meteorites, and it was determined that the absorptions are likely related to iron phyllosilicate minerals. The identified asteroid features were weak, with the strongest having an absorption intensity of 5%. Many of the asteroid features were similar to those seen in CI1 and CM2 meteorites; however, the asteroid's features are generally one-third to one-half as strong as the meteorites' features. Meteorite types 1 or 2 are considered to be aqueously altered primitive material (*i.e.* having not undergone substantial metamorphism either by heating or pressure). Therefore, type 1 and 2 chondrite mineralogy are most likely the results of low-temperature aqueous alterations of original metallic and silicate material. An alteration sequence proposed by Vilas and Gaffey (1989) starts with anhydrous parent material similar to CV3 chondrites (type 3 indicating little to no alteration [Weisberg et al., 2006]). Metal materials are altered to form an iron-rich tochilinite. Olivine alters to magnesium serpentine, and tochilinite reacts with serpentine to form an iron-rich cronstedtite (a 1:1 phyllosilicate).

The alteration sequence proposed by Vilas and Gaffey (1989) would also be detectable in the asteroid's albedo, due to tochilinite's tendency to act as an opaque mineral, if in the initial stages of aqueous alteration. If tochilinite is a major surface component, a large drop in albedo should occur. However, if organics and kerogen compounds were already ubiquitous, this decrease will be minimal. This process would also likely overpower any surface absorption features. As the process continues and Fe phyllosilicates form, the phyllosilicates should become more prominent as a result of the lower absorbance due to the decrease in tochilinite.

While a consensus has grown around phyllosilicate minerals being responsible for many of the spectral absorptions identified in the C-complex asteroids, there is still much debate about what specific types of phyllosilicate are present on these bodies. In (1) Ceres alone, ammoniated phyllosilicates (De Sanctis et al., 2015; King & Clark, 1986), mixtures of carbonates and oxidized iron clays (Carry et al., 2008; Rivkin et al., 2006), and mixtures of brucite and carbonates (Milliken & Rivkin, 2009) have all been proposed as possible surface minerals responsible for the 3-µm absorption feature observed in (1) Ceres' spectrum. With the DAWN probe's arrival to (1) Ceres, carbonate and sulfate deposits have been confirmed to exist in craters (Longobardo et al., 2019; Tosi et al., 2018); the low lying carbonate beds are likely deposited when briny material is sublimated (Nathues et al., 2015), much like evaporate deposits found on Earth.

With the identification of hydrate and carbonate deposits, De Angelis et al. (2016) conducted a laboratory study on the spectral properties produced by brucite, carbonate, and clay mixtures in the 0.2-5.1-µm spectrographic range. Brucite [$Mg(OH)_2$] is a hydroxide mineral that is a relatively uncommon mineral on Earth, but it is a common aqueous alteration product between periclase, an Mg-rich ultramafic mineral, and Mg-carbonates, such as dolomite (Bowles, 2021). Brucite can also be produced with the phyllosilicate mineral serpentine when Mg-rich olivine is aqueously altered (Frost & Kloprogge, 1999). These two alteration sequences make brucite a prime candidate for a secondary phase mineral if aqueous alteration is prevalent on, or within, C-complex asteroids. De Angelis et al. (2016) determined that a diagnostic absorption related to brucite occurred at ~2.45-µm, while other main absorptions are identifiable at 0.95- and 3.05-µm. However, the 0.95-µm feature was not visible in mixtures with less than ~50% brucite and was only pronounced when brucite was as high as 100-80% and carbonates as

low as 10%. De Angelis et al. concluded that due to the lack of features between 0.9-2.5-µm their results ruled out the presence of brucite occurring ubiquitously and in abundance on the surface of (1) Ceres.

Before De Angelis et al.'s (2016) study, Beck et al. (2015) investigated the evolution of brucite absorption features as temperatures decreased. Beck et al.'s study investigated spectra between 0.50-4.00-µm and identified absorptions, at room temperature, at 1.30-, 1.36-, 1.395-, 2.10-, 2.47-, 2.70-, 2.84-, and 3.06-µm. The brucite samples were then cooled down to 50 K. Beck et al. identified shifts in band position at 1.36-µm and 1.39-µm when temperatures decreased. More importantly, the intensity of features at 2.82-µm and 3.06-µm microns decreased when exposed to low temperatures. However, the current study is only investigating the VNIR spectral ranges; therefore, the drops in intensity at longer wavelengths are not relevant to this research. Beck et al. also concluded that brucite cannot account for the 3.06-µm feature, which was the same conclusion reached by De Sanctis et al. (2016). It should be noted that Beck et al. (2015) only studied pure brucite rather than a mixture of components like De Sanctis (2016), therefore; De Sanctis' study (2016) is likely representative of actual surface chemistries, and features identified in Beck et al.'s study (2015) may have been subdued by the properties of other surface components.

2.11: AMMONIATED MINERALS

Ammonia (NH_3) is an important molecule for understanding the formation of organic compounds and volatiles in the early solar system and planetary bodies. For example, N isotopic analysis of ancient rock formation in Western Australia, with an age of ~2.7 Ga, revealed an ammonia-rich environment at the time of deposition, which is a likely indicator of early biologic processes (Stüeken et al., 2015). Multiple recent studies have been investigating absorption

features produced by possible ammoniated surface minerals. Minerals that form in an environment with an excess of ammonia, such as carlsbergite (CrN), have been identified in meteorites (Harries et al., 2015); therefore, ammonia that is free or incorporated into minerals may be detectable through spectrographic investigations. Free ammonia has been documented to produce absorptions at fundamental frequencies denoted by ν and subscript, with ν_1 = 3.29-µm, ν_2 = 5.95-µm, ν_3 = 3.18-µm, and ν_4 = 7.14-µm (Harlov et al., 2001; Stinchcomb & Barker, 1929). While all the documented fundamental frequencies fall outside the spectral range of the current study, overtones and asymmetric stretching combinations of free NH_4 does produce absorptions at ~1.05-, ~1.3-, ~1.56-, ~2.02-, and ~2.12-µm (Bruno & Svoronos, 2005; Busigny et al., 2004; Herzberg, 1945; Mookherjee et al., 2002), all of which are within the spectral range of the current study.

Ammoniated phyllosilicates (phyllosilicates containing an NH_3 molecule or NH_4^+ ion) have been suggested as possible surface group minerals by multiple authors and studies. King et al. (1992) suggested ammoniated saponite, a smectite/clay mineral, as a possible surface minerals responsible for the 3.0-µm absorption feature rather than a small but significant amount of H_2O frost/ice, which was proposed by Feierberg et al. (1981). King et al. (1992) found that the 3.07-µm absorption that contributes to (1) Ceres' 3.0-µm band is much too narrow to be caused by the presence of H_2O ice on the surface of (1) Ceres. Multiple mixtures of ammoniated phyllosilicates were compared to (1) Ceres' 3.0-µm feature, and ammoniated saponite was identified as the best fit. Saponite is a trioctahedral smectite that is produced when mafic minerals are hydrothermally altered (Weaver & Pollard, 1979). Ammoniated saponite would be produced when the free H_2O responsible for aqueous alteration contains ammoniated ions. Ammoniated smectite has been reported to be present as a secondary aqueous alteration product

in CV and CI carbonaceous chondrites (Zolensky & McSween, 1988), as well as saponite being identified in at least one unusual CM2 chondrite (Brealey, 1995). De-ammoniation of smectite has been recorded to occur when T > 400 K (Chourabi & Fripiat, 1981). Since phyllosilicates are not likely to be produced in the protoplanetary nebula environment, a secondary heating event is likely responsible for the production of ammoniated phyllosilicates. If a secondary heating event did occur, it likely did not exceed 400 K, which would indicate that minimal secondary thermal metamorphism likely occurred near (1) Ceres' surface.

The DAWN mission provided high resolution surface observations providing opportunity to better understand (1) Ceres' surface chemistry. The DAWN probe entered orbit around (1) Ceres in March 2015 after leaving Vesta in 2012 and orbited the dwarf planet for more than three years, completing its mission at the end of 2018 (Russell et al., 2016). Scientific measurements of (1) Ceres from the DAWN probe began in December 2014 during its approach to the dwarf planet (Ciarniello et al., 2017). Utilizing the spectrographic instruments of the DAWN probe, De Sanctis et al. (2015) investigated the spectra of (1) Ceres from 0.4-5.0-μm from distances of ~82,000 to 4,300 km from the surface. De Sanctis et al. reported that features related to ammoniated phyllosilicates were detected across the entire surface of (1) Ceres, though at some locations the features were subdued. The features identified and compared were located at 2.72-, 3.1-, 3.3- to 3.5-, and 3.95-μm. By comparing mixtures of ammoniated clay minerals, Mg-carbonates, and organic components to the observed spectral distribution of (1) Ceres, it was determined that ammoniated phyllosilicates are ubiquitous on the surface of (1) Ceres, yet there may be surface regions with lower concentrations. De Sanctis et al.'s findings have since been affirmed by multiple studies (Ammannito et al., 2016; Tosi et al., 2018).

No detectable water ice was reported, and daytime surface temperatures of (1) Ceres were measured to be 180 - 240 K at a heliocentric distance of 2.86 AU. This range of temperatures is generally incompatible with widespread surface ice on (1) Ceres' surface environment. However, protected localized occurrences could survive sublimation, thus resulting in the thin layer of water vapor detected around (1) Ceres (Küppers et al., 2014). The lack of surface hydration contradicts the earlier assumption by King et al. (1992) that ammoniated phyllosilicates were produced via direct hydrous alteration of mafic primary minerals. However, later studies have identified an abundance of ammonia-rich organics incorporated in CI, CM, and CR chondrites (Pizzarello & Williams, 2012). If the surface of (1) Ceres contains similar ammoniated organic abundances as the aforementioned carbonaceous chondrites, De Sanctis et al. (2015) suggest that ammoniated phyllosilicates could have been produced through cation exchange capacity, which has been investigated as a viable ammoniation method by Borden and Giese (2001). Cation exchange can occur when the ammoniated organics and surrounding secondary phyllosilicates are heated to temperatures of 300 – 400° C. De Sanctis et al. (2015) noted that common clay minerals, specifically smectite, and montmorillonite could readily incorporate ammonia via cation exchange. Nevertheless, De Sanctis et al. were not able to identify the specific phyllosilicate bearing ammonia, in part due to the lack of NH_4^+ -phyllosilicate spectra in the literature.

With the likely identification of ammonia-bearing minerals on (1) Ceres, a need for detailed studies on the spectral properties of ammoniated minerals arose. Berg et al. (2016) investigated a variety of ammonium-bearing minerals, both natural and synthetic, including the following: chlorides, nitrates, feldspars, palagonitic soils, carbonates, phyllosilicates, and

sulfates. Berg et al. identified a host of absorptions relating to ammonia molecule overtones, combinations, or interactions within the studied minerals.

As for the band centers relevant to this study, absorption features were detected in the 1.05-1.08-µm region, 1.25-1.37-µm region, 1.5-1.6-µm region, and 2.12-2.34-µm region, with the specific band center being dependent on the mineral chemistry. Since Berg et al. identified multiple absorptions in the 1-2.5-µm range, the absence of absorptions between 1-2.5-µm on (1) Ceres could be used as an argument against the presence of ammoniated minerals on the surface of (1) Ceres, as the diagnostic NH_4 overtones and combination modes produce absorptions throughout this range. However, multiple minerals/compounds investigated by Beck et al. (2015) produced weak features in this range. Another explanation is that ammoniated minerals may only represent a minor component of (1) Ceres' surface composition; therefore, only the stronger 3.0-µm feature remains visible, while the subtle, shorter features are subdued by more abundant opaque mineral assemblages.

Following Berg et al.'s (2016) study, Ferrari et al. (2019) conducted a similar study, though only focusing on ammoniated phyllosilicate group minerals. Ten different ammonia-bearing phyllosilicates were investigated for related absorptions. Multiple instruments were utilized, allowing for a spectral range from 0.2-µm to 14-µm to be investigated. Reflectance spectra of ammoniated clays showed bands near 1.56-, 2.05-, 2.12-, 3.06-, 3.25-, 3.55-, 4.2-, 5.7-, and 7.0-µm that were related to nitrogen complexes in the mineral. It was also determined that Fe-, Na-, and Ca-smectites easily accepted NH_4^+ ions while other phyllosilicate minerals, particularly types with limited expansions between the tetrahedron layers (illite, mica, antigorite, sepiolite), did not readily accept NH_4^+ ions. Mixtures of ammonium-bearing smectite with a Mg-bearing phyllosilicate, such as serpentine, produced spectra with strong similarities to (1) Ceres'

spectrum, further supporting other studies concluding that smectite is the ammonia-bearing phyllosilicate on (1) Ceres' surface. Ferrari et al.'s (2019) results also imply that a global aqueous alteration phase occurred in (1) Ceres' past, during which smectite was produced. However, their study was not able to ascertain whether the ammoniation process occurred at the same time of aqueous alteration, as suggested by King et al. (1992), or during a later heating event, as suggested by De Sanctis et al. (2015). Table 1. details the absorption features relevant to this research that have been identified in past studies.

Table 1. Band Center measurements of materials that are expected to exist on the surface of G-class asteroids. Electron transitions in Fe-bearing minerals would indicate the presence of an oxidized phyllosilicate. OH-Vibrational transitions would indicate the presence of hydrated minerals such as phyllosilicates.

Interaction/Material		**Feature wavelength (μm)**					
Electron Transitions in oxidized Fe Bearing minerals		0.43[a]	0.65[a]	0.7[b]	0.85[a]	0.94[a]	
OH-Vibrational Transitions		1.4[a]	1.75[a]	1.9[a]	2.2[a]	2.35[a]	2.72[c]
Ammoniated clay Minerals		~1.3[f]	1.56[d,f]	2.05[d,f]	2.12[d,f]		
Organics	CH	1.1-1.2[e]	1.4[e]	1.75[e]	2.2-2.4[e]		
	NH	1.1[e]	1.2[e]				
	OH	0.9[e]	1.4[e]	1.21[e]			

a. (Hunt & Ashley,1979), b. (Vilas & Sykes, 1996), c. (De Sanctis et al., 2015), d. (Ferrari et al., 2019), e. (S. Gaffey, 1993), f. (Berg et al., 2016).

2.12 METEORITE CLASSIFICATION REVIEW

Unlike asteroid classifications, which rely on remotely sensed spectrographic or photometric information, the classification of meteorites is based on the mineralogic properties and, for some groups, the degree to which the meteorite has been affected by metamorphic or

aqueous alteration. Meteorite classifications have evolved to account for the discovery of unique meteorites and as more accurate and detailed scientific investigations became practical. The current meteorite classification scheme is based on both G. Rose's classification, which was used to classify the University of Berlin's meteorite collection, and Maskelyne's classification, which was developed to classify the British Museum's collection (Breznia, 1904; Bischoff, 2001; Weisberg et al., 2006). Maskelyne's classification categorized meteorites as either siderites (irons), siderolites (stony-irons), or aerolites (stones). While Rose's classification scheme was the first to split stones into chondrites and achondrites, with chondrites exhibiting chondrules and achondrites lacking chondrules. During the 20th century, multiple classification schemes were introduced to advance Rose's and Maskelyne's original classifications, with the current classification schemes largely based on Prior's (1920) classification, which was modified by Mason (1967). The current classification scheme for meteorites has three major divisions: undifferentiated chondrites, differentiated achondrites, and primitive achondrites. Each division contains classes, clans, and groups. While the iron meteorites exhibit many distinct and scientifically significant properties, the stony meteorites are most significant to the current study, and they will be focused on in the following section.

2.12.1 CHONDRITES

The chondrites are subdivided into three major classes - the ordinary chondrites, enstatite chondrites, and carbonaceous chondrites - which all contain subclassifications referred to as clans and groups. Major lithologic properties of each chondritic type can be found in Table 2. The ordinary chondrites are almost entirely composed of primary mafic minerals, such as olivine, pyroxene, feldspars, and metallic Fe-Ni minerals. The ordinary chondrites only have a single clan that includes the H, L, and LL groups. The clan groups are separated by the ratio of

Fe-Ni in metallic minerals (Van Schmus & Wood, 1967), with the H ordinary chondrites exhibiting high levels of Fe-Ni metallic material (~8 vol%), the L ordinary chondrites exhibiting lower levels of Fe-Ni metallic material (~4 vol%), and the LL having extremely low levels of metallic minerals (~2 vol%). The ordinary chondrites also exhibit an increase in average chondrule diameter from H to LL groups. The concentration of Fe in olivine also serves as a diagnostic measurement when differentiating the ordinary chondrites, with the H group having an olivine composition of 16-20 mol% Fa, the L having 23-26 mol% Fa, and the LL having 27-32 mol% Fa. (Weisberg et al., 2006; Van Schmus & Wood, 1967). The ordinary chondrites represent the most common materials in the meteorite collections, massing more than 85% of falls (Weisberg et al., 2006). The ordinary chondrites commonly exhibit large chondrules, as well as a wide range of aqueous and metamorphic alterations (Dodd, 1981), which is commonly referred to as the petrologic type.

The enstatite chondrites formed under highly reducing conditions, as their mineralogy contains very little Fe-silicate material (Keil, 1968). Since Fe is abundant in all other chondrites, the enstatites are an extremely unique class. The enstatite class contains only a single clan that is occupied by the EH and EL groups, which are differentiated by the composition of sulfide minerals (Weisberg et al., 2006), with the EH chondrites being slightly more reduced and having a high concentration of sulfide minerals when compared to the EL chondrites. The EH chondrites also contain a higher concentration of Si in the Ni-Fe metal, with concentrations generally 2-3 wt% as well as a slightly smaller average chondrule diameter at 0.2 mm, while the EL chondrites exhibit less than 1 wt% Si in Ni-Fe metal and a larger average chondrule diameter at 0.6 mm (Weisberg et al., 2006).

The carbonaceous chondrites are subdivided into four clans (CI clan, CM-CO clan, CV-

CK clan, CR clan), which are then subdivided into multiple groups. The CI clan only contains the CI group, the CM-CO clan contains the CM and CO groups, the CV-CK clan contains the CV and CK group, and the CR clan contains the CR, CH, and CB groups. The carbonaceous chondrites are classified by whole-chondrite elemental abundances, normalized for Mg (Weisberg, 2006). Carbonaceous chondrites can range from matrix-rich (CH, CB) to chondrule dominant (CI, CM, CO, CV, and CR) in composition. Some carbonaceous chondrites such as the CM and Cis, exhibit relatively high percentages of water and carbon-hydrogen compounds (i.e., organics) (Wing & Bada, 1991; Ehrenfreund et al., 2001). The O isotope compositions of carbonaceous chondrite groups plot on different continuum near or below the terrestrial fractionation line, indicating that many clans and groups derived from different source material in the protoplanetary environment (Clayton & Toshiko, 1999). Even though carbonaceous chondrites exhibit a broad array of chemistries, they only represent roughly ~4.5% of falls (Weisberg, 2006; Bischoff & Geiger, 1995).

The CI chondrites completely lack chondrules and metal material. They are entirely composed of aqueously altered phyllosilicate-rich matrix material (petrologic type 1), with bulk compositions extremely similar to the solar photosphere. This similarity leads many to assume that the CIs are the most primitive solar system materials (Endress et al., 1996). The CM and CO groups are the most abundant carbonaceous groups and are thought to be related due to their similar size and composition of anhydrous minerals, similar refractory-lithophile-element abundances, and similar O-isotopic compositions of high-temperature minerals (Kallemeyn & Wasson, 1982). The chondrule abundances on average are slightly higher in the CO group at 48 vol%, compared to the CM group at 20 vol%, though the CO group does exhibit a high disparity in chondrule abundance from one CM to another. A higher degree of calcium aluminum

inclusions (CAI) is also present in the CM group at 13 vol% compared to the 5 vol% CAI abundance in CO's (Weisberg et al., 2006). The CV and CK groups show a greater depletion in volatile elements when compared to CO and CM groups. The CV and CK groups are likely related because low petrologic type CK chondrites exhibit chemical, mineralogical, and petrographic similarities to the CV chondrites (Weisberg et al., 2006, Greenwood et al., 2005). These groups also exhibit nearly identical abundances of chondrules (40 vol%), CAI occurrences (10 vol%), and metal (0-5 wt%). (Weisberg et al., 2006). The CV and CK groups can be differentiated by the CK chondrites' having a higher concentration of fayalite and a highly oxidized matrix chemistry.

The CR clan contains the CR, CH, and CB chondrite groups. While these groups have different petrologic characteristics and chemistries, they do share some distinct properties, indicating a genetic relationship. Similar characteristics amongst the CR clan meteorites include being metal-rich, which is relatively rare in the carbonaceous class; being highly depleted of volatile elements; exhibiting similar O-isotopic compositions; having most of their anhydrous minerals being Mg-rich; and containing a heavily hydrated matrix consisting of predominantly phyllosilicate minerals (Weisberg et al., 2006). Major differences between the groups in the CR clan include the metal abundance increases when comparing the CR (5-8 vol%), CH (20 vol%), and CB (60-80 vol%) groups. The matrix abundance follows an inverse trend with CB exhibiting <<1 vol% matrix, CH 5 vol%, and the CR ranging from 30-50 vol% (Weisberg et al., 2006).

As the name suggests, the carbonaceous chondrites contain significant abundances of carbon, though oxides, evaporates, carbonates, hydrated and dehydrated phyllosilicates, and organic compounds have been identified in carbonaceous meteorites (McSween & Richardson, 1977; Endress et al., 1996; Choi et al., 1997; Leshin et al., 1997). Similarly, the Tholen C-

complex asteroids have been confirmed to exhibit an abundance of carbon, water, and organic molecules through both spectroscopic studies and spacecraft missions (details in section 2.7-2.11). Many have assumed that the C-complex asteroids and carbonaceous chondrites are genetically related, and while much work has been done to determine probable parent bodies for the carbonaceous chondrites (Wood, 1967; Burbine, 1998; Gaffey & McCord, 1978; Hiroi et al., 1996; Eschrig et al., 2021), no probable parent asteroid has yet to be determined for any carbonaceous chondrite.

Table 2. General lithologies of major chondritic meteorite groups. Modified from Ruben (1997).

Group	General Lithology
Carbonaceous Chondrites	
CI	Aqueously altered, chondrule-free; volatile-rich
CM	Aqueously altered; minichondrule-bearing
CR	Aqueously altered; primitive-chondrule-bearing; metal-bearing
CV	Large chondrules; abundant CAIs; partially aqueously altered
CK	Large chondrules; darkened silicates
CH	Microchondule-bearing; volatile poor
Ordinary Chondrites	
H	High total iron
L	Low total iron
LL	Low total iron; low metallic iron
Enstatite Chondrites	
EH	High total iron; highly reduced; minichondrule-bearing
EL	Low total iron; highly reduced; moderately sized chondrule.

2.12.2 ACHONDRITES

Table 3 details the general lithologies for the groups found in both types of achondrites, primitive and differentiated. The primitive achondrites exhibit whole-rock chemical compositions and O-isotopic values that align well with chondritic characteristics. Some primitive chondrite groups also exhibit relic chondrules. It is most likely that the primitive achondrites are representative of primary chondritic material that has undergone metamorphism and either partial or extensive melting, resulting in the destruction of the original chondrites (Prinz et al., 1983). The primitive achondrite term does lack a concise definition, though in recent years many have accepted the definition suggested by Prinz et al. (1983) and Weisberg et al. (2006) which defines primitive achondrites as meteoric material that has exceeded solidus temperature inside the parent body, inducing partial melting but not crystalizing from a melt. Or, if the material was crystallized from a melt, it was derived from parent bodies that had not reached differentiation equilibrium, resulting in the meteorite retaining chemistries extremely similar to that of chondritic material.

Differentiated achondrites, on the other hand, did solidify from a melt on a differentiated parent body, which results in the meteorites exhibiting chemistries that are not consistent with chondritic chemistries. The HED meteorites (howardites, eucrites, and diogenites) almost certainly derived from the same parent body, with (4) Vesta and the V-type asteroids being the most probable parent bodies (Burbine et al., 2001; Ruzicka et al., 1997; Gaffey, 1997). The eucrites are representative of pyroxene-rich basaltic melts, and the diogenites are representative of igneous material formed in the lower crust of (4) Vesta, most likely in a plutonic structure. The howardites link the eucrites and diogenites, as they consist of brecciated material containing fragments of both meteorites, which likely represent the impact ejecta that formed after a

catastrophic disruption event between (4) Vesta and another asteroid.

Another achondrite, the aubrite group, is highly reduced and exhibits similar whole-rock chemistry to the enstatite chondrites and has mineral occurrences similar to the enstatite chondrites (Rubin, 1997). This similarity indicates that the enstatite chondrites and the aubrites share a parent body or primordial material source. The ureilite group is one of the most enigmatic meteorite groups, consisting of a carbonaceous-like matrix with calcic, chromian olivine, and low-Ca pyroxene scattered throughout (Goodrich, 1992). The angrites are basaltic meteorites, consisting mostly of augite with occurrences of olivine and antlerite (Rubin, 1997). The Brachinites are very similar to primitive achondrites and consist almost entirely of olivine (75-98 vol%), with occasional occurrences of clinopyroxene and orthopyroxene (Nehru et al., 1992).

Table 3. General lithologies of achondritic meteorite groups. Modified from Rubin (1997).

Group	General Lithology
Primitive Achondrites	
Acapulcoites	Chondritic abundances of plagioclase and troilite; medium-grained
Lodranites	Subchondritic abundances of plagioclase and troilite; coarse-grained
Wononaites	IAB-silicate-related
Differentiated Achondrites	
Eucrites	Basaltic
Diogenites	Orthopyroxene
Howardites	Brecciated mixtures of basalts and orthopyroxene
Angrites	Fassaitic-pyroxene-bearing basalts
Aubrites	Enstatite achondrites
Ureilites	Olivine-,pyroxene-, carbonaceous-matrix-bearing
Brachinites	Equiangular; olivine-, clinopyroxene-, and orthopyroxene-bearing

2.12.3 METEORITE SPECTRAL FEATURES

While we can easily study the geochemistry and lithology of meteorites in laboratories on Earth, the same is not true for asteroids within our solar system. Therefore, the spectral distribution of meteorites must be investigated to determine what mineral assemblages and properties are detectable in meteorite spectra as studies into meteorite spectra can then better inform those looking to determine what minerals are producing diagnostic or detectable features in the spectra of asteroids. Unlike asteroids, meteorites are susceptible to terrestrial weathering, which affects the chemistry and lithology of the meteorite - including H_2O features at approximately 1.9-µm, the oxidization of any Fe metallic material, and the production of

secondary phase minerals such as phyllosilicates and evaporates (Rubin, 1997). Space weathering on asteroids must also be considered when comparing meteorite spectra to asteroids spectra. While studies have attempted to simulate space weathering of meteoritic material (see Chapter 2.5), the effects of space weathering on many asteroid and meteorite types remains uncertain. For the reasons stated, curve matching is a relatively poor tool at determining likely meteorite parent bodies, and genetic links should instead be based on mineralogic analysis of the spectral distribution.

The hydrated carbonaceous chondrites (Figure 9) are all dominated by a semi-conductive opaque phase (carbon), resulting in the spectra of carbonaceous chondrites having very low albedo and subdued features or an absence of features altogether. Both C1 and C2 hydrated carbonaceous chondrites are dominated by aqueously altered secondary minerals and lack spectral bands related to pyroxene and olivine in the VNIR (Gaffey, 1976). However, some hydrated carbonaceous meteorites, such as CM2 Murchison, and CM2 Mighei, do show subtle features indicative of hydrated minerals (Figure 9).

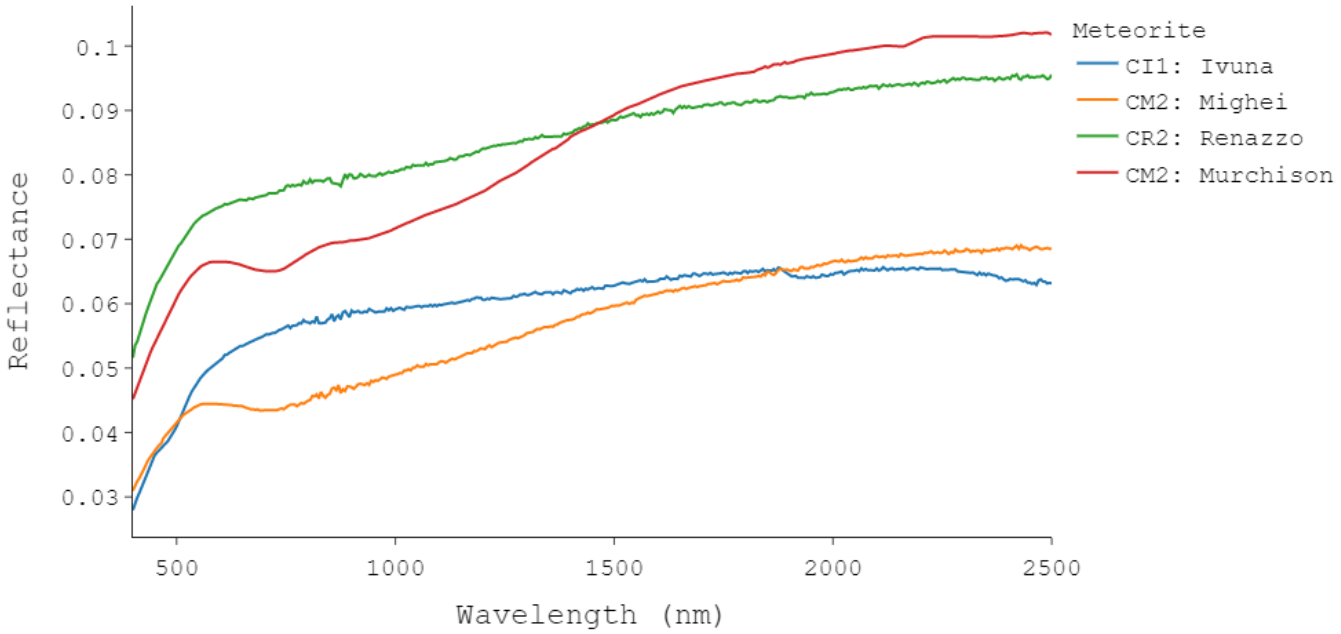

Figure 9. Visible and near-infrared spectra of four hydrated carbonaceous chondrites. The hydrated carbonaceous chondrites lack intense features throughout the NIR due to concentrations of carbon. However, meteorites do show subtle features related to hydrated secondary minerals. Spectra gathered from NASA's PDS Geosciences Node Spectral Library.

The anhydrous carbonaceous chondrites contain concentrations of carbon, resulting in the reduction of spectral features. However, the primary mafic minerals exhibit more intense features in the VNIR when compared to the secondary aqueous minerals that dominate hydrated carbonaceous chondrites. The common primary mafic minerals (olivine, pyroxene, and feldspar) have relatively low optical densities in the visible and near-infrared regions, except when absorption features occur (Gaffey, 1976). The low optical densities result in the production of intense features centered near 1000-nm (1.0-µm) and 2000-nm (2.0-µm). The two C3 chondrites, shown in Figure 10 do show slightly defined pyroxene-olivine bands, indicating a higher concentration of primary mineral assemblages than the hydrated carbonaceous meteorites do.

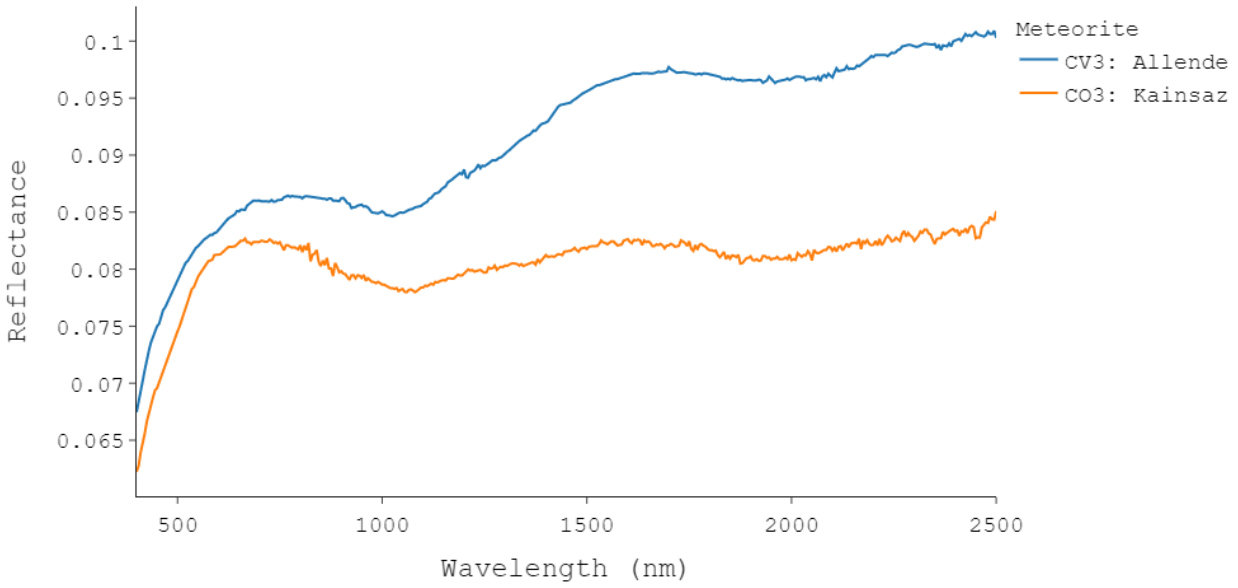

Figure 10. A visible and near-infrared spectra of two anhydrous carbonaceous chondrites. Both meteorites exhibit two subdued features throughout the NIR, indicating concentrations of olivine and pyroxene. Spectra gathered from NASA's PDS Geosciences Node Spectral Library.

In meteorites that lack opaque mineral phases, the primary mafic minerals' spectra are more intense. Eucrites are composed almost entirely of pyroxene; they show a strong symmetric pyroxene curve with a subtle additional feature related to feldspar redward of 1000-nm (Gaffey, 1976) (Figure 11). Ordinary chondrites also exhibit stronger absorption features than the carbonaceous chondrites do, but due to an abundance of olivine, the 1000-nm feature is extended redward. Since the displacement of the 1000-nm feature is correlated with the olivine concentration, the displacement is minimal in the H ordinary chondrites and maximized in L chondrites (Figure 12) (Gaffey, 1976).

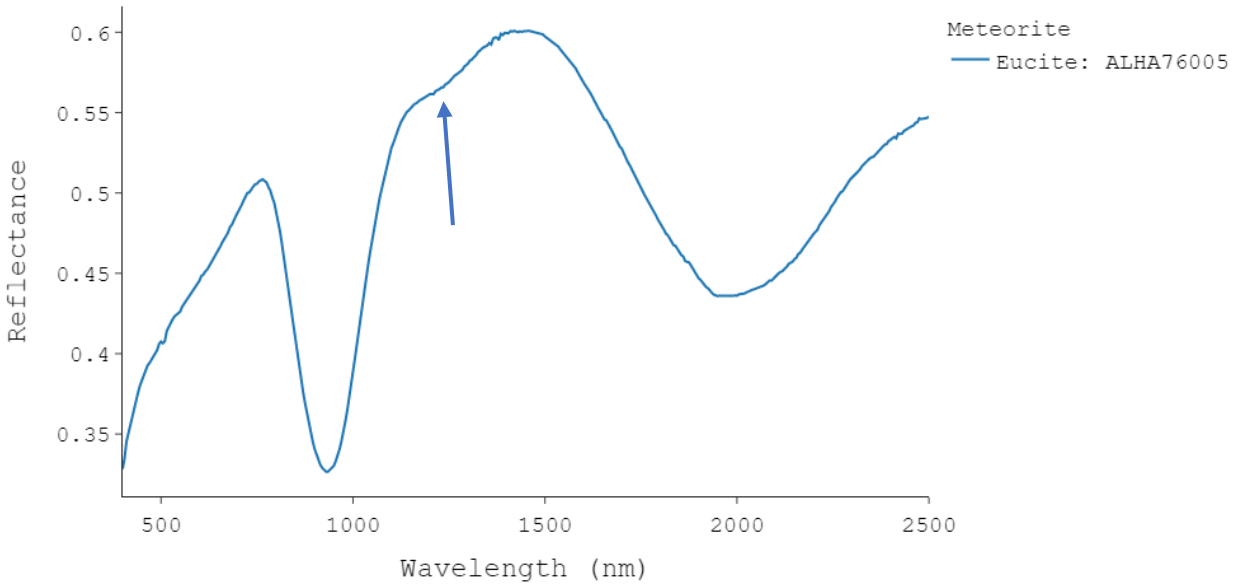

Figure 11. A visible and near-infrared spectra of eucrite ALHA76005. Intense 1000- and 2000-nm features are the result of pyroxene; the smaller feature redward of 1000-nm is produced by feldspar (indicated by the arrow). Spectra gathered from NASA's PDS Geosciences Node Spectral Library.

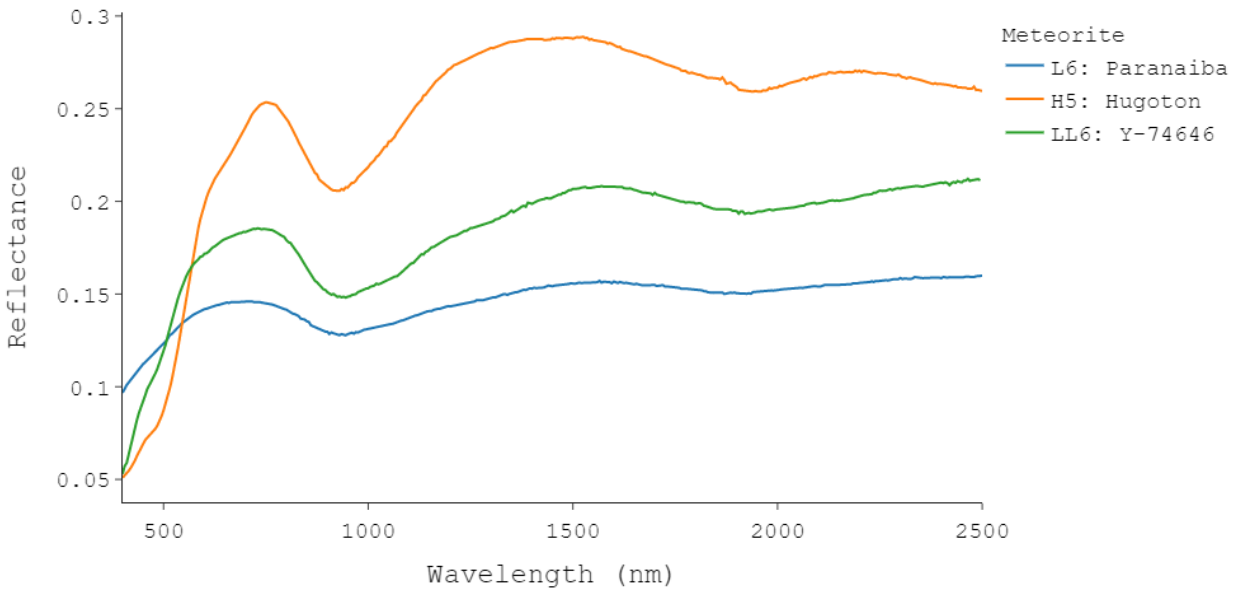

Figure 12. A visible and near-infrared spectrum of three ordinary chondrites. The pyroxene feature is present, though the 1000-nm feature is extended redward due to the presence of olivine. The extension of the 1000-nm feature is more intense in the L and LL groups, as they contain a higher concentration of olivine. Spectra gathered from NASA's PDS Geosciences Node Spectral Library.

CHAPTER III: METHODS

3.1: TARGETS

The Tholen G-class asteroids consist of approximately 30 asteroids, and five of the G-class asteroids were selected for this study: (1) Ceres, (13) Egeria, (19) Fortuna, (84) Klio, and (130) Elektra. Asteroid (1) Ceres is the largest known body in the main asteroid belt, with a diameter of 95 km and an average heliocentric distance of 2.77 AU (Park et al., 2016). (1) Ceres is undoubtedly the most studied G-class asteroid due to its bright apparent magnitude and the DAWN mission, which orbited (1) Ceres from March 2015 until the end of its mission in October 2018. From its vantage point, the DAWN probe collected data responsible for the discovery of approximately 130 high albedo geologic deposits, known as faculae, which are likely evaporate minerals deposited during the sublimated or water-brine mixtures. The largest of these deposits is located at the base of Occator crater (Nathues et al., 2015). The evaporate deposits - along with spectral investigations (Ciarniello et al., 2017), thermodynamic models (Castillo-Rogez & McCord, 2010), and geologic features (Chilton et al., 2019; Krohn et al., 2016, 2018) - indicate that (1) Ceres is most likely a partially differentiated dwarf planet (Russell et al., 2016). While there is little doubt that the interior of (1) Ceres has a significant amount of water content, there is still uncertainty on how much water ice remains near the surface and whether the concentration of water has drastically altered the surface mineralogy of (1) Ceres. The DAWN Mission has shown that (1) Ceres is much more geologically diverse and active compared to the dusty, dry asteroids once assumed to be the norm in the asteroid belt, which only presses the need for further investigation into other members of the G-class asteroid population.

(13) Egeria, (19) Fortuna, (84) Klio, and (130) Elektra have yet to be visited by an interplanetary probe; therefore, all of the information collected on these planetesimals has been collected via instrumentation on Earth. While much can be ascertained from remote observations, little can be determined about any given asteroid's surface texture or structure. These asteroids possess a much lower mass and diameter than (1) Ceres does. It is possible that the smaller G-class asteroids did not congregate enough mass or energy to drive the geologic activity that was observed on (1) Ceres by the DAWN probe. If the processes occurring on (1) Ceres produced extensive evolution of the surface mineralogy of (1) Ceres, there are likely to be spectroscopically disparate features between (1) Ceres and its less massive G-class members.

3.2: OBSERVATIONS AND DATA COLLECTION

All asteroids included in this study were previous targets of the Small Main-Belt Asteroid Spectroscopic Survey II (SMASS-II), which observed 1341 main-belt asteroids and collected spectra encompassing the visible wavelength regime. All SMASS-II observations were conducted by the Michigan-Dartmouth-MIT Observatory at Kitt Peak, Arizona, on either the 1.3-m McGraw-Hill telescope or the 2.4-m Hiltner Telescope between 1993 and 1999. Both telescopes used the Mk III Long Slit CCD spectrograph capable of acquiring spectra from 0.435-0.925-μm (Bus & Binzel, 2002). The SMASS-II observations were able to produce spectra with resolutions as high as 0.001-μm per pixel, providing a far greater amount of spectroscopic details and information than the 8-channel photometric data originally used to classify the G-class asteroids did (Tholen, 1984). All reduced SMASS-II spectra were retrieved from the NASA Planetary Data System's archive.

For the current study, the NIR spectroscopic observations of all asteroids were conducted using the 3-m NASA Infrared Telescope (IRTF) atop Mauna Kea, Hawai'i. All IRTF

observations utilized the SpeX Spectrograph in low-resolution mode, which is capable of acquiring spectra from 0.68-2.52-μm, with a resolving power of ~250 when using a 0.8" slit (Rayner et al., 2003). All IRTF observations were obtained when airmasses were below 2.0 and conducted in asteroid-local standard star sets, meaning a local standard star within the same or very similar airmass was observed before and after the asteroid observations. The standard star observations will be used to create a model of atmospheric extinction at the airmass of the target.

The observations of (1) Ceres, (13) Egeria, and (19) Fortuna were conducted by Dr. Sherry Fieber-Beyer on July 21, 2016. The spectrum of (1) Ceres was reduced at an earlier date by Dr. Fieber-Beyer and provided as a finalized spectrum. (13) Egeria and (19) Fortuna were provided as raw spectra and required reduction for this study. The technique used will be discussed later in this chapter. The spectra for (84) Klio and (130) Elektra were collected by Dr. Vishnu Reddy in 2003 and 2012, respectively (Reddy, 2016). The reduced spectra for both objects were retrieved from the NASA Planetary Data System's archive.

3.3: ASTEROID SPECTRUM REDUCTION

As stated in the previous section, asteroids (1) Ceres', (84) Klio's, and (130) Elektra's NIR spectra were provided as calibrated spectra. However, (13) Egeria's, and (19) Fortuna's NIR spectra were provided as raw IRTF spectra that required reduction to remove atmospheric absorption features and to calibrate wavelengths. The reduction process used in this study is detailed in Gaffey, 2002; 2003), though a detailed explanation follows.

3.3.1: STARPACK CREATION

To remove the atmospheric absorption features at the asteroid's airmass, a star exhibiting the same spectral properties as the Sun (solar analog) is observed within the same airmass range

as the asteroid. The solar analog's acquired spectra are utilized to create a model of the atmospheric features, known as a starpack. The starpack is created in SpecPR (Spectrum Processing Routine), authored by Clark (1980, 1993) and modified by Gaffey (2003). The first step in starpack creation is determining the correct offsets for each observation group of individual spectra acquired under the same telescope geometry (observation set). As the telescope orientation changes, subtle instrument flexure occurs, causing photons of any particular wavelength to strike slightly different locations on the array detector. If left uncorrected, these offsets can propagate through to the final spectrum, creating distortions great enough to affect the composition analysis, and even the spectral taxon classification of the object (Gaffey, 2002).

To correct for slight spectral deviations, each observation set requires a slight offset of less than one pixel. This offset is performed in SpecPr by assigning an observational set as a reference set; then the subsequent observational sets are offset manually through trial and error until the correct offset is determined. The correct offset is identified when spectral discontinuities are minimized, and water vapor features remain below the continuum of the spectra. With the offset flux distributions, the slope and the intercept of the linear least-squares fit can be used to compute the effective flux of the standard star at any airmass within an appropriate interval. The set of slopes and intercepts for all wavelengths of the observations is termed a "starpack" (Figure 13) (Gaffey, 2002).

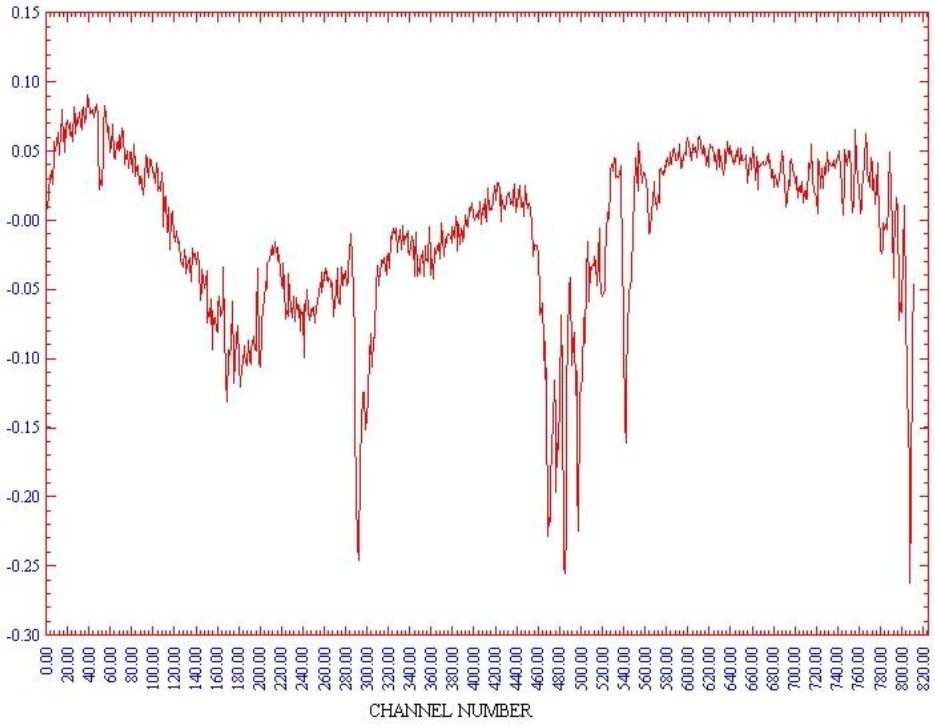

Figure 13. The final starpack used to model atmospheric extinction and features produced by HD32092. HD32092 was used as a solar analog for (13) Egeria.

3.3.2: ATMOSPHERIC CORRECTIONS

The photons collected by the spectroscopic equipment not only carry the information of the reflected asteroid surface, but also carry information from our Sun, Earth's atmosphere, and any other matter the photons may have interacted with before being collected by the spectrograph. Since the observed standard star produces the same flux distribution as the Sun does, and the photons emitted travel through the same density of atmosphere as the asteroid's photons do, the starpack contains the same information as the asteroid flux distribution, except for the information derived from the asteroid. To create a flux distribution that only contains information related to the reflectance of the target asteroid, the quotient of the target's collected flux distribution and the flux distribution of the standard star is determined. Therefore, any

contribution in the asteroid flux related to the atmosphere and solar flux will be canceled, resulting in a flux distribution containing information solely relating to the target's reflectance (Equation 1.A.) (M. Gaffey, 2002). Where a solar analog is not available in the immediate area of the asteroid during observations, a standard star with similar spectral properties can be observed. To correct the flux distribution of the local standard star, the local standard star must also be divided by a sun-like flux distribution. This process is detailed in Equation 1.B.

$$\mathbf{1.A.}\quad Reflectance_{\lambda}\,(Target) = \frac{Flux_{\lambda}\,(Target)}{Flux_{\lambda}(Standard\ Star)}$$

$$\mathbf{1.B.}\quad Reflectance_{\lambda}\,(Target) = \frac{Flux_{\lambda}\,(Target)}{Flux_{\lambda}(Standard\ Star)} * \frac{Flux_{\lambda}(Standard\ Star)}{Flux_{\lambda}(Solar\ Analog)}$$

Equation 1. A. Removing solar and atmospheric features from the target's reflectance spectrum for each wavelength. In this case, the standard star is equivalent in flux distribution to the Sun. B. Removing solar and atmospheric features from an asteroid's reflectance spectrum for each wavelength, when the standard star does not have a sun-like flux distribution. The local standard star must be divided by a solar analog star that was observed on the same night to remove discrepancies in the stellar flux distribution (Gaffey, 2002).

As discussed in Chapter 3.3.1, instrument flexure, caused by the telescope movement, will result in photons of any particular wavelength striking a slightly different location on the detector. Thus, when dividing the target's flux distribution by the standard star's flux distribution, the target's flux distribution must be offset in relation to the standard star. This process occurs manually and follows the same criteria for offsetting standard star observations (detailed in Chapter 3.3.1). Due to asteroid integration times being much greater than stellar integrations, telescope tracking can introduce a non-trivial amount of instrument flexure between each integration while tracking the target. Consequently, each target observation must be offset individually, rather than applying a single offset value to the entire observation set. When the

discussed processes are completed, each asteroid integration will be individually representative of the asteroid's surface reflectance.

3.3.3: PRODUCTION OF NIGHTLY AVERAGE SPECTRUM

While integrating on a target, several events can affect the final reflectance spectrum. These could include cosmic ray strikes on the sensor, a fleeting cloud, a short wind gust, and more. While the spectral reduction discussed in the earlier sub-sections of this chapter attempts to mitigate these effects, much of the time it is impossible to remove the discrepancies that are produced from short-lived events that only affect a small proportion of the integrations. To correct for events that only caused discrepancies in a fraction of the integrations, an average spectrum of the nightly observations of any given target is produced.

Generally, there are 10-20 integrations per target per night. After creating a reduced reflectance spectrum for each integration (discussed in Chapter 3.2.1), the reduced spectra are combined to create a spectral average of the observations. Any data point greater than 2.0-σ from the average is not considered, which will remove any major disparities in a single spectrum. After we produce the nightly average spectrum for all observations, the spectrum is scrutinized for any discrepancies. The discrepancies could include large flux spikes, features that rise above the continuum, major discontinuities, or generally noisy sections. If a discrepancy is identified in an individual reduced spectrum, that spectrum will not be included in the next round of averaging. After removing the reduced reflectance spectra with disparities (commonly 3-5), a second nightly average spectrum is produced, keeping the 2.0-σ deviation. Then the process of identifying discrepancies is repeated, and another nightly average is produced. This process continues until a nightly average spectrum that has minimal noise and no major discrepancies are present in the spectrum. Commonly this occurs when only 3-6 of the reduced reflectance spectra

remain. It should be noted that the purpose of this process is not to arbitrarily remove reduced reflectance spectra until a handful of the most similar of spectra remains. The goal of this process is to remove any features that are not common amongst the nightly average. This pruning of spectra ensures that the features present in the final nightly average are representative of the target's reflectance properties and are not influenced by short-lived external events that affected a small number of integrations. The processes involving averaging and calculating discussed in this section are conducted using SpecPR.

3.3.4: SPECTRAL NORMALIZATION

Once the final nightly average spectrum ("NIR spectrum" from here on) is created, the visible spectrum, collected during the SMASS-II survey, can be combined and normalized creating a VNIR spectrum. The NIR spectrum data is extracted from SpecPR into a text file containing three columns of data containing wavelength, flux, and error, respectively. The IRTF spectral data is now in the same format that the SMASS-II archived data is. Simply appending the SMASS-II data to the IRTF will result in a spectrum with the SMASS-II portion being offset in the flux-dependent axis from the IRTF. This offset is due to the observed albedo being dependent on the telescope's light-gathering ability, observing conditions, and the target's orientation.

To correct for the offset, a range of five wavelength points and their corresponding flux measurements that are in the center of the overlap between the two spectra are selected. For this study, the center of the overlap commonly occurred around 0.8-μm. The mean flux of the five wavelength points is calculated, and the quotient of the mean NIR and the mean visible flux is the normalization constant. A visible spectrum with flux normalized to the NIR spectrum is produced by summing the normalization constant and the flux for each wavelength. The

normalized VNIR spectrum is produced by appending the normalized visible spectrum and the NIR spectrum.

3.4: BAND CENTER MEASUREMENTS

After the VNIR spectrum is normalized and reduced, it can be investigated for absorption features in the spectrum. An absorption feature is produced when electromagnetic radiation is absorbed rather than reflected when interacting with an electron. The absorption of electromagnetic energy with a discrete wavelength results in a reflectance spectrum with a drop in intensity at that is at the wavelength's location in the flux distribution; the wavelength of the absorption feature is proportional to the energy of the electromagnetic radiation. The energy absorbed by the is dictated by the chemistry and atomic structure of the reflected material. The location of absorption features is one of the most robust indicators of chemistry, as band centers are relatively resistant to the effects of space weathering, unlike other spectral properties such as spectral curve matching (Gaffey, 2002; Lantz & Clark, 2012).

To measure an absorption feature in SpecPR, a continuum is fit across the length of the feature, connecting the spectral continuum at each end of the feature and encompassing the feature (Figure 14A). Any point below the fitted continuum is extracted as the raw curve. The raw curve contains all the minute spectral deviation in flux that is expected in a final spectrum. This noise makes it extremely difficult to calculate the feature's center. To reduce the effects of noise in the raw curve, a polynomial fit is calculated to smooth out the raw curve function (Figure 14B). Ideally, the polynomial fit will only contain a single location where a tangent has a slope of zero. If the polynomial fit contains more than one point with a tangent slope of zero, the dimensions of the raw curve must be modified to only contain the desired features curve. The point along the polynomial fit with a derivative of zero is then calculated; this point corresponds

to where the tangential slope is zero, therefore the bottom of the polynomial fit.

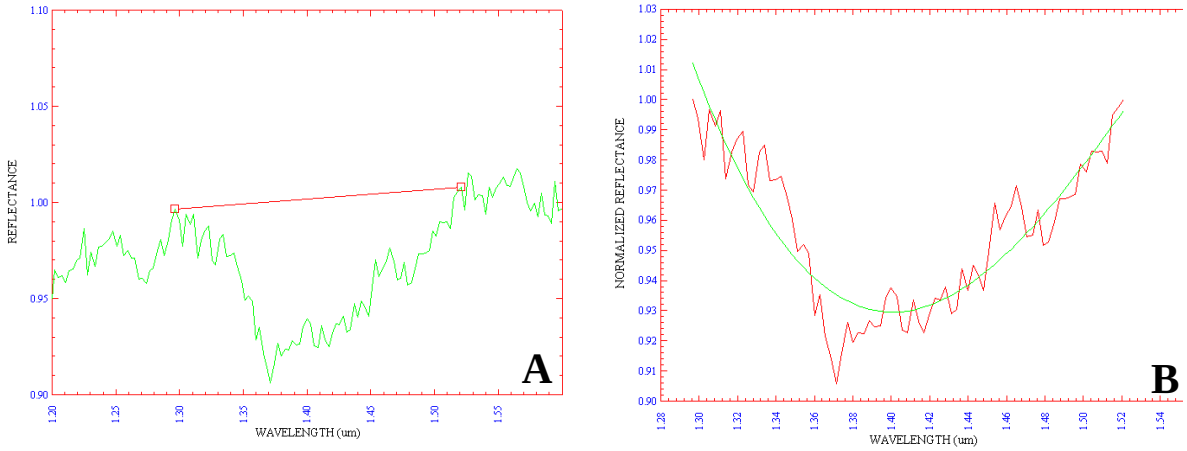

Figure 14. A. Fitted continuum (red line) placed over an absorption feature in (13) Egeria spectrum (green line). B. Extracted raw curve (red line) with a ratioed polynomial curve fitted to the raw curve (green line). Determining at what point the polynomial raw curve's derivative is equal to zero indicates where the tangent is zero and, therefore, where the center of the polynomial fit is.

The first polynomial fit center rarely corresponds to the center of the raw curve being measured. Therefore, the first polynomial fit that aligns with the calculated center does not correspond to the center of the feature. To refine the alignment of the polynomial fit, the boundaries of the polynomial fit must be "walked" toward the center by slightly narrowing the wavelength range being considered to calculate the polynomial fit. After each "step" in the "walk" towards the center of the raw curve, a new polynomial fit is calculated. After several steps decreasing the range of the polynomial fit, the polynomial fit should extend through the center of the raw curve both in the y and x-axes, though not be so constrained that no curve can be calculated. At this point, the center of the polynomial fit will correspond to the center of the raw curve, and, by association, be equal to the center of the measured feature. The number of steps required to match the raw curve and the polynomial fit is unique to each feature; spectral properties, such as the overall feature wavelength range, the spectral noise, and the overall feature shape will affect the steps required. Commonly the number of steps is anywhere between

5 and 20. To determine the error of the feature center location, the standard deviation of the polynomial fit is calculated using all the polynomial fit attempts calculated while walking in the feature. The SpeX spectrograph and Mk III CCD spectrograph have a reported wavelength discrepancy of 0.01-μm (Rayner et al., 2003). Therefore, if the calculated standard deviation is lower than the accuracy of the spectrograph, a deviation of 0.01-μm is reported.

CHAPTER IV: RESULTS

All NIR spectra were gathered using the 3-meter NASA Infrared Telescope facility and the SpeX spectrograph. Observational techniques, reduction methods, and spectral measurement techniques are detailed in Chapter III. All NIR spectra were normalized and combined with SMASS II CCD spectra (Binzel et al., 1993) to create a VNIR spectrum from ~0.4-2.5-μm. Table 4 lists absorptions measured in each spectrum.

Table 4. All values of features that were measured in 5 G-class asteroids are reported in microns (μm). The header indicates the feature's name, while the value listed in each object's row indicates the feature's center position. "POSSIBLE" indicates that a feature may be present but was not measurable.

Feature:	(1) Ceres	(13) Egeria	(19) Fortuna	(84) Klio	(130) Elektra
0.7	NONE	0.69 ± 0.01	0.70 ± 0.01	0.69 ± 0.01	0.74 ± 0.01
0.95	NONE	0.95 ± 0.01	0.94 ± 0.01	POSSIBLE	0.92 ± 0.01
1.14	NONE	1.13 ± 0.01	1.14 ± 0.01	POSSIBLE	POSSIBLE
1.25	NONE	1.27 ± 0.01	POSSIBLE	NONE	1.22 ± 0.05
1.4	NONE	1.40 ± 0.01	1.44 ± 0.01	POSSIBLE	NONE
1.9	NONE	1.90 ± 0.01	POSSIBLE	NONE	POSSIBLE
2.3	NONE	NONE	POSSIBLE	POSSIBLE	2.33 ± 0.01

The following sub-sections will detail the properties of each asteroid's spectrum and attempt to correlate the spectral properties to the spectral properties of minerals published in past research.

4.1: (1) CERES

(1) Ceres' VNIR spectrum (Figure 15) does not contain an absorption feature at 0.7-µm, like all other asteroids in this study do, though it still contains the steep UV slope attributed to G and C taxon asteroids. In the NIR range, (1) Ceres exhibits a single broad feature that extends from ~0.8 – 2.5-µm. (1) Ceres' slope between ~0.8-2.5-µm is slightly red in the available spectral distribution range. An 8th-degree polynomial regression of (1) Ceres' spectrum was calculated and used to determine that (1) Ceres' spectrum has an R^2 value of ~0.9495 and a root mean squared error of ~0.005 (Figure 16).

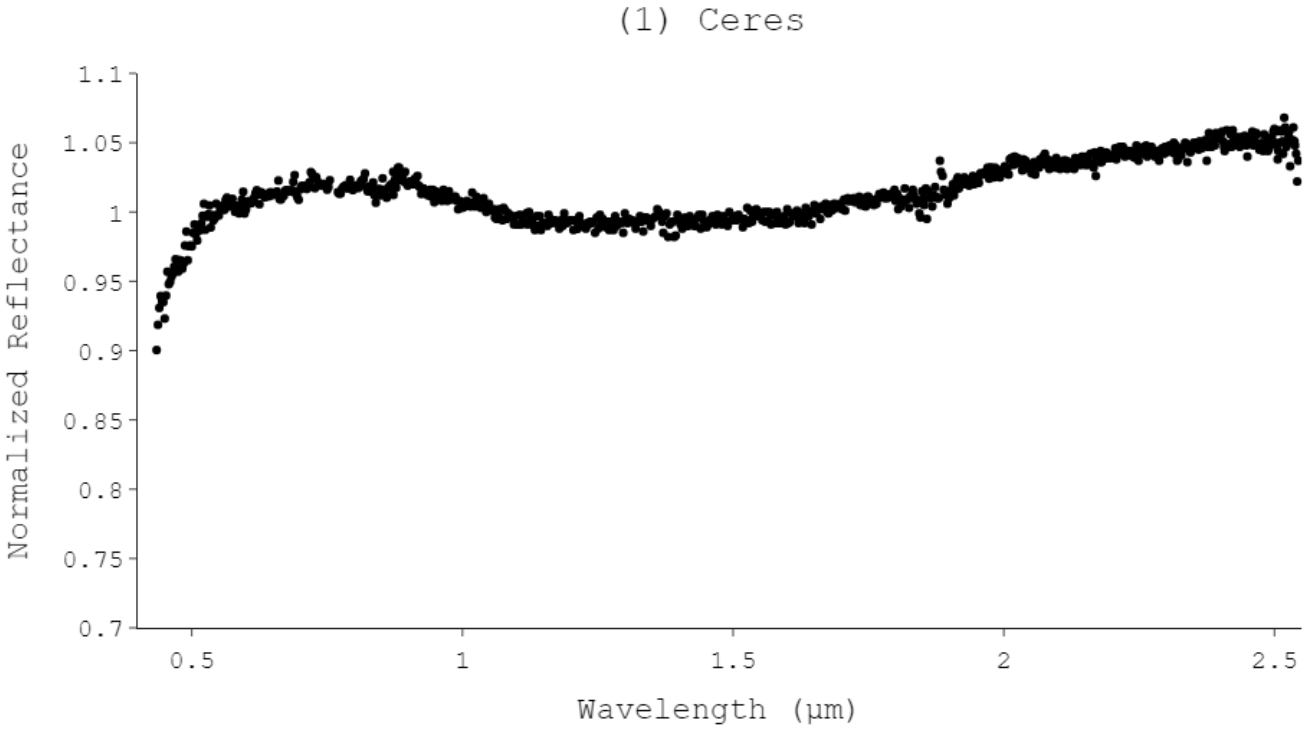

Figure 15. VNIR spectrum of (1) Ceres, produced by normalizing and combining SMASS II Visible CCD spectrum (R. P. Binzel et al., 1993), and near-infrared spectrum was observed and provided by Dr. Fieber-Beyer (personal communication, 2020).

Spectrum contains steep UV feature associated with the G-class asteroids, followed by broad NIR feature between (~0.8-2.5-µm).

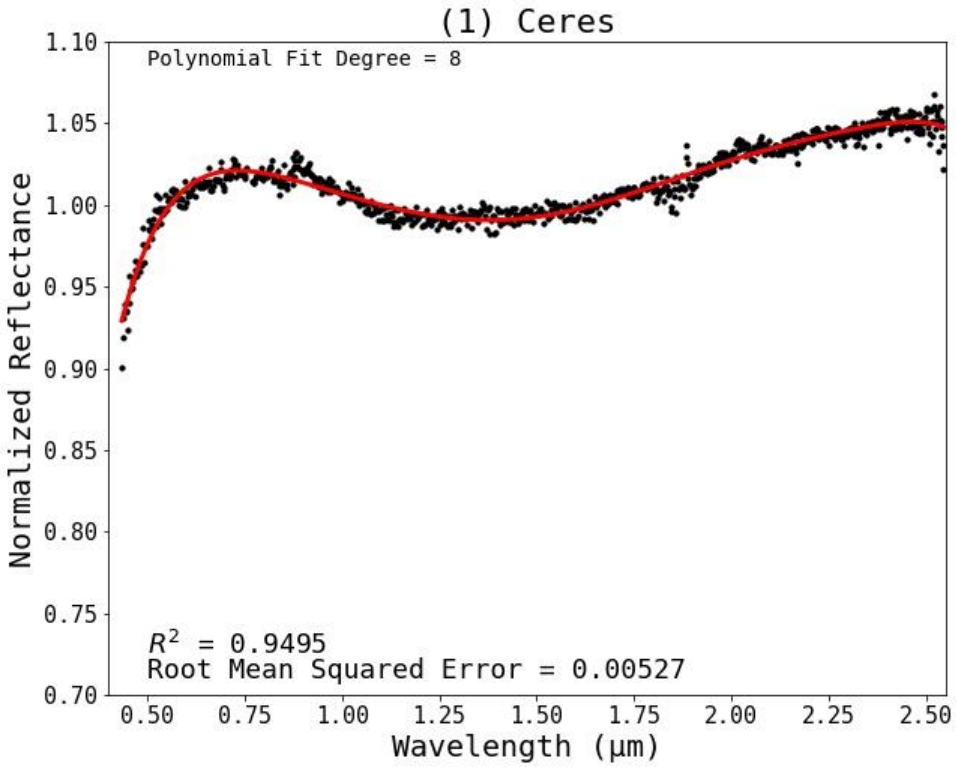

Figure 16. The red line indicates the 8th degree polynomial function calculated from (1) Ceres' spectrum. The R-squared value between the polynomial fit and (1) Ceres' spectrum was determined to ~0.9495, and the root mean squared error is ~0.005.

The lack of a 0.7-μm feature in (1) Ceres' spectrum likely indicates limited oxidized iron phyllosilicate electron transfer occurrence (Vilas & Sykes, 1996). A weak 0.6-μm absorption was identified by Vilas et al. (1993), which could be associated with oxidized iron minerals. However, this feature was not identifiable in the (1) Ceres spectrum presented in this study and was not reported in recent visible spectrographic investigations via the DAWN probe (Rousseau et al., 2020). The single broad feature between ~0.8-2.5-μm is rarely mentioned in other studies, as the features located at and around 3.0-μm are the most diagnostic features on (1) Ceres in the near-infrared. Many recent studies have agreed that the features around 3.0-μm are most likely related to ammoniated phyllosilicate minerals such as ammoniated smectite, montmorillonite,

chlorites, or serpentine (Beck et al., 2015; De Angelis et al., 2016; De Sanctis et al., 2015; King et al., 1992). Visible and NIR spectral measurements collected by the DAWN VIR spectrometer confirm that the 0.4-0.8-µm slope is consistent with either ammoniated or Mg-bearing phyllosilicate minerals (Ammannito et al., 2016; Rousseau et al., 2020). The region between 1.2-2.5-µm is dominated by OH and H_2O vibrational transitions in aqueously altered minerals (Hunt & Ashley, 1979). If phyllosilicate minerals are responsible for the 3.0-µm features, it would be expected that features could be identified within the aforementioned spectral range. However, (1) Ceres only contains a broad feature extending from ~0.8-2.5-µm. It has been suggested that this feature is produced by magnetite deposits (Larson et al., 1979). Magnetite can be produced when Si is stripped from the $Fe_3Si_2O_5(OH)_4$ component of serpentine (Frost & Beard, 2007), making serpentine a viable alteration product on (1) Ceres. With measurements from the DAWN mission, both magnetite and carbon have been identified as possible surface materials on (1) Ceres (Marchi et al., 2019). Therefore, the magnetite and opaque carbon deposits may be responsible for masking the weaker OH and H_2O vibrational features created by phyllosilicates between 0.8-2.5-µm.

4.2: (13) EGERIA

(13) Egeria's VNIR spectrum (Figure 17) contains the typical G-class steep UV slope. A 21st-degree polynomial fit was applied to (13) Egeria's spectrum (Figure 18). The R^2 value between the polynomial fit and (13) Egeria's spectrum was determined to be 0.9486, and the root mean squared error was calculated to be ~0.15. The narrow and steep features at 1.4- and 1.9-µm were modeled poorly by the polynomial fit, which is likely the reason for the poor root mean squared error. The UV feature reaches a relative maximum at ~0.6-µm, after which is a broad and relatively shallow absorption centered at 0.69 ± 0.01-µm. A red slope follows the 0.69-µm feature, with a subtle feature centered at 0.95 ± 0.01-µm roughly halfway up the slope. The

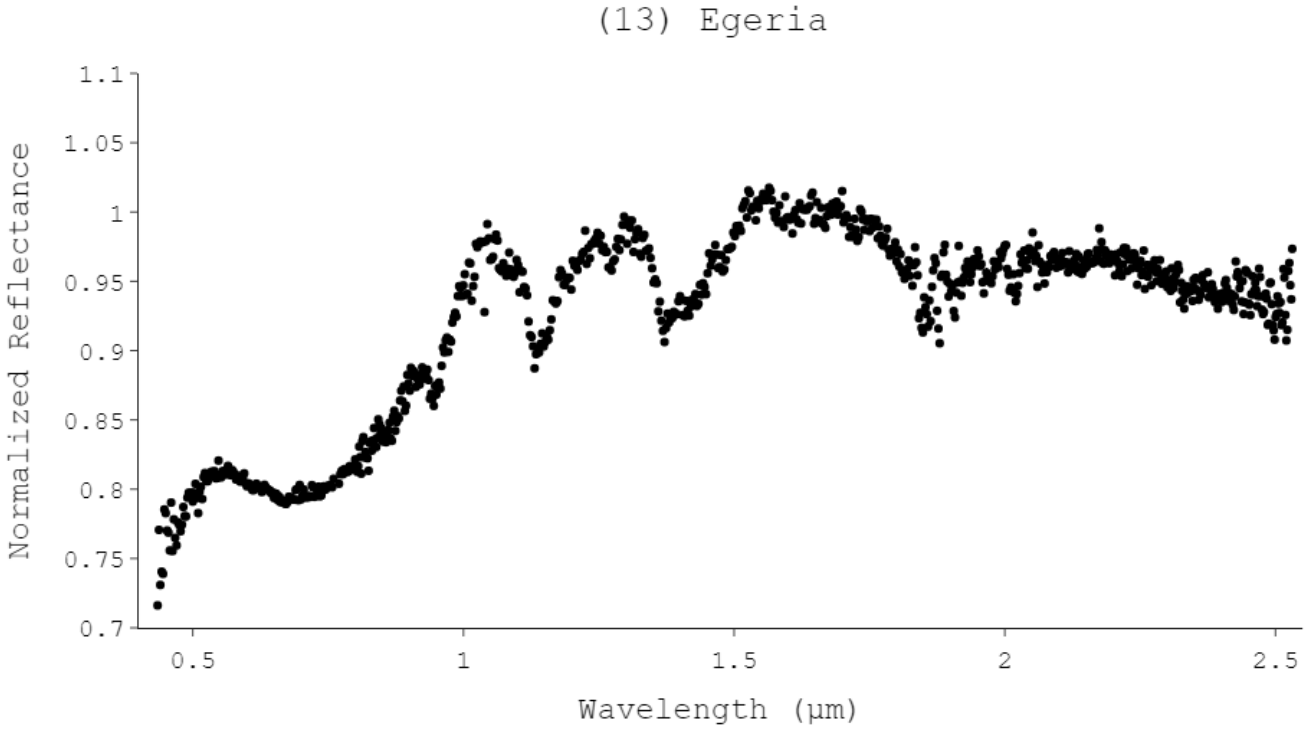

Figure 17. VNIR spectrum of (13) Egeria, produced by normalizing and combining SMASS II Visible CCD spectrum (R. P. Binzel et al., 1993), and near-infrared spectrum, observed and provided by Dr. Fieber-Beyer (personal communication, 2020).

Multiple features are present in (13) Egeria's spectrum, and the calculated band centers are listed in Table 5.

second red slope reaches a maximum at ~1-µm, and after this point the continuum remains relatively flat throughout the distribution. Multiple deep features are exhibited throughout the spectral range from 1- to 2-µm, with band centers at 1.13 ± 0.01, 1.27 ± 0.01, 1.40 ± 0.01, and 1.89 ± 0.01-µm (Table 4).

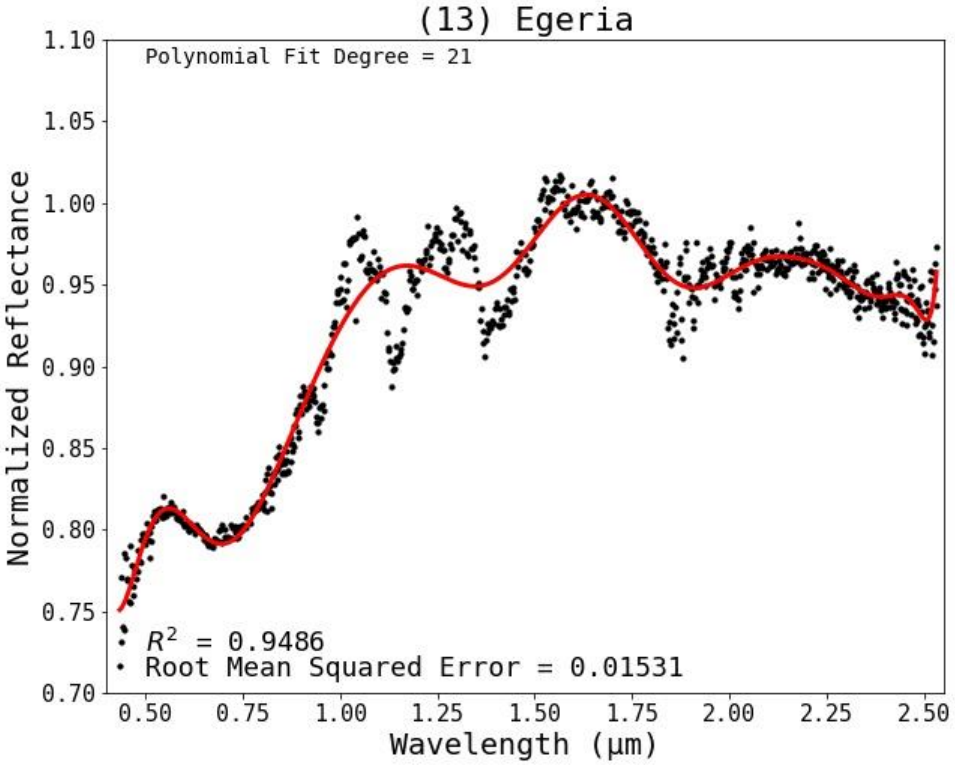

Figure 18. The red line indicates the 21st degree polynomial function calculated from (13) Egeria's spectrum. The R-squared value between the polynomial fit and (13) Egeria's spectra was determined to be ~0.9495, and the root mean squared error is ~0.005. Due to the steep and narrow 1.14- and 1.9-µm features, the polynomial fit was poor from approximately 1.2-1.5-µm, which contributed to the large root mean square error and poor R^2 value.

(13) Egeria's 0.7-µm band indicates that oxidized iron phyllosilicates are present on the surface (Vilas & Sykes, 1996), with the 0.95-µm feature being indicative of another iron hydroxide goethite [$Fe^{3+}O(OH)$] (Hunt & Ashley, 1979). While the 1.40- and 1.90-µm are two common telluric absorption features, they are also frequently expressed by hydrated minerals.

Most commonly, the 1.4- and 1.9-µm features are produced by interlayer OH or H_2O within phyllosilicate minerals and are specifically related to OH vibrational transitions (Hunt & Ashley, 1979). The 1.4-µm feature appears to be a combination of two features, creating two sharp minima that combine to create a single feature. This characteristic feature has been observed in phyllosilicates (Bruckenthal & Singer, 1987; S. Gaffey, 1993). S. Gaffey's (1993) and Hunt's (1979) investigations found similarly structured 1.4-µm features in two different phyllosilicates, kaolinite and hectorite.

While Vaporized H_2O can produce features at 0.91-µm and 1.14-µm (S. Gaffey, 1993), it seems unlikely that (13) Egeria could sustain a detectable atmosphere containing water vapor or have an active geologic process producing detectable water vapor. Water vapor would also be expected to produce features at 1.87-, 1.32-, and 0.8-µm (S. Gaffey, 1993). However, organic compounds such as CH and NH produce absorptions near 1.14-µm, most notably CH_2 producing a feature whose center varies between 1.1-1.2-µm. The presence of CH indicates an abundance of carbon-bearing organics or carbonates, which have been confirmed to be widespread on another C-complex asteroid, (101955) Bennu (Kaplan et al., 2020). While the presence of NH indicates ammoniated organic materials or molecules incorporated into minerals being widespread on the surface (S. Gaffey, 1993).

4.3: (19) FORTUNA

(19) Fortuna has a typical steep UV slope reaching a relative maxima at ~0.55-µm. (19) Fortuna's spectrum also exhibits a strong feature centered at 0.70 ± 0.01-µm and has a reddened slope throughout. When a linear trendline is fitted to the spectrum, it produces a slope of +0.102. Throughout the VNIR spectral regime, three absorptions are measured, with those in the NIR being subtle features (Figure 19), the calculated absorption centers are listed in Table 4. To determine the overall spread of the spectrum a 14^{th} -degree polynomial regression of (19) Fortuna's spectrum was calculated (Figure 20), which was used to determine that (19) Fortuna has an R^2 value of ~0.99472 and a root mean squared error of ~0.00486.

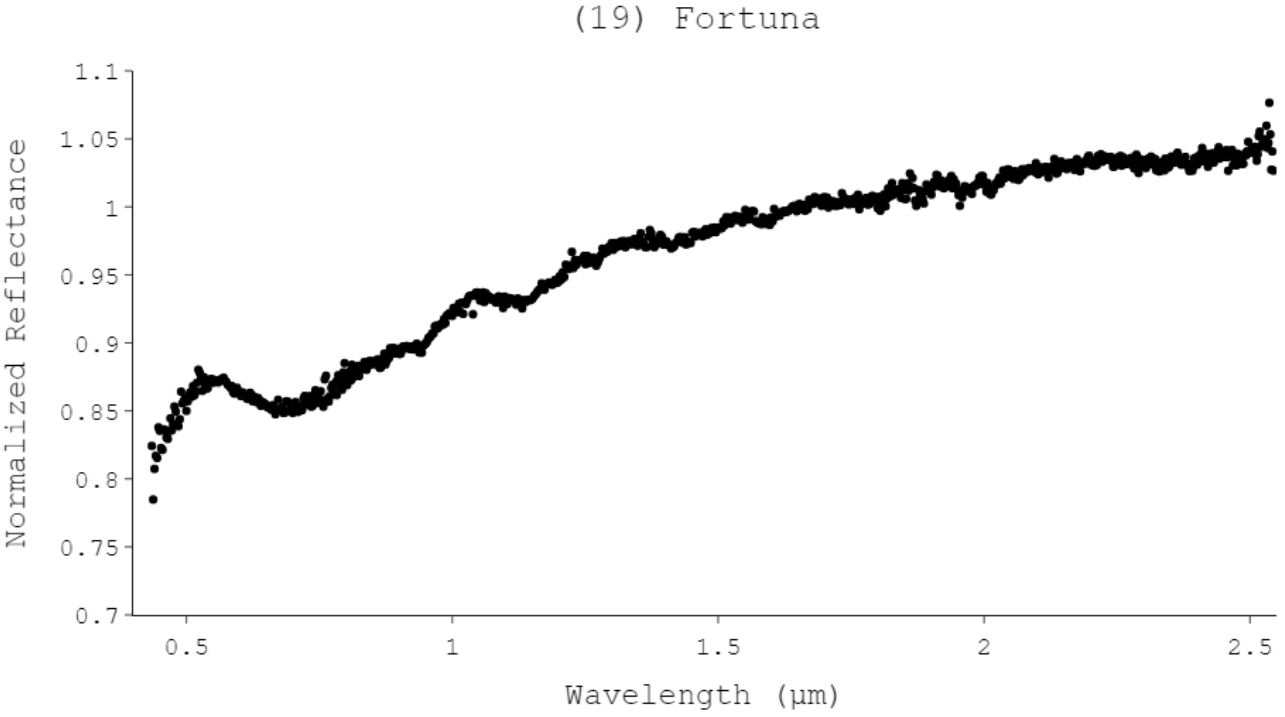

Figure 19. VNIR spectrum of (19) Fortuna produced by normalizing and combining SMASS-II Visible CCD spectrum (R. P. Binzel et al., 1993), and near-infrared spectrum observed and provided by Dr. Fieber-Beyer (personal communication, 2020).

(19) Fortuna exhibits a strong 0.7-µm feature followed by redward slope with multiple shallow features throughout the NIR. Each absorption with calculated center is listed in Table 4.

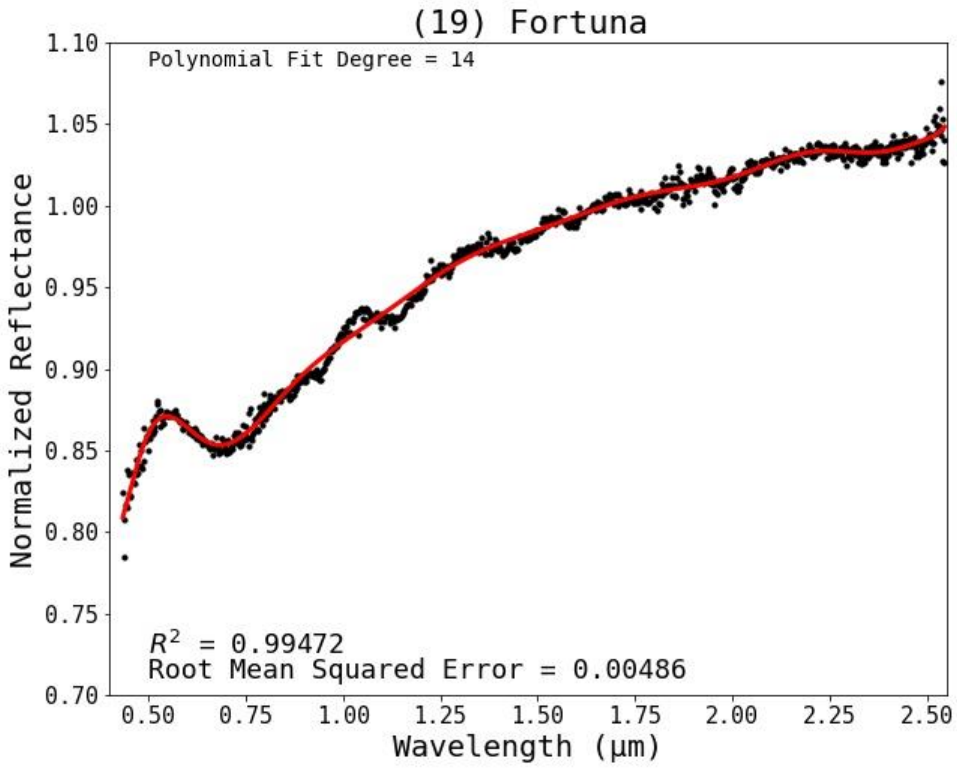

Figure 20. The red line indicates the 14th degree polynomial function calculated from the spectrum of (19) Fortuna. The R-squared value between the polynomial fit and (19) Fortuna's spectrum was determined to be ~0.99472, and the root mean squared error is ~0.005.

While (19) Fortuna exhibits much of the same features as (13) Egeria, (19) Fortuna's spectral features are less intense absorptions and a more prominent reddened slope. The 0.7-μm feature is likely related to hydrated iron phyllosilicates as suggested by Vilas and Sykes (1996). The 0.95-μm feature is also an indication of electron transition in iron-bearing minerals, with goethite having an absorption feature at 0.94-μm (Hunt & Ashley, 1979). The slight 1.14-μm feature may be an indication of NH or CH compounds, either incorporated in minerals or organic molecules (S. Gaffey, 1993). The 1.4-μm feature is likely an indication of OH^- or H_2O incorporated into hydroxide minerals or phyllosilicate group minerals that easily incorporate

hydroxyl molecules and water (S. Gaffey, 1993; Hunt & Ashley, 1979).

4.4: (84) KLIO

(84) Klio contains the steep UV slope followed by a strong 0.7-μm feature that is also exhibited in (13) Egeria and (19) Fortuna. From 0.8- to 1.6-μm, (84) Klio has a slightly shallower slope when compared to (19) Fortuna, and after ~1.6-μm, (84) Klio's spectrum flattens to a neutral slope throughout the rest of the spectrum. The available spectrum may have absorptions at ~0.9-, 1.14-, and 1.4-μm; however, the general noise throughout the continuum

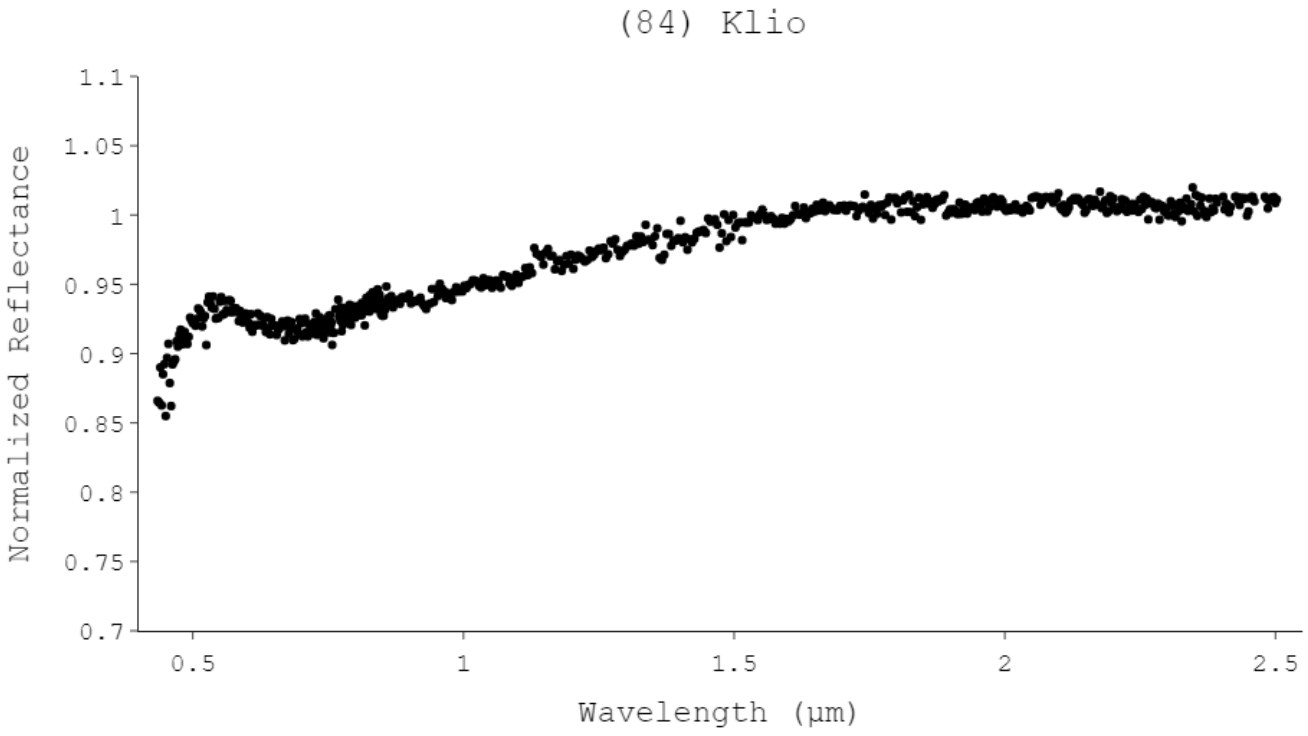

Figure 21. VNIR spectra of (84) Klio, produced by combining and normalizing SMASS-II visible CCD data (R. P. Binzel et al., 1993), and IRTF SpeX NIR data acquired and calibrated and uploaded to the planetary data science system (Reddy & Sanchez, 2016).

(84) Klio exhibits a steep UV slope typical of the G-class followed by a strong 0.7-μm feature. (84) Klio is relatively featureless in the NIR, and the measured feature center is reported in Table 4.

limits our ability to accurately measure features at these locations.

A 12th-degree polynomial regression of (84) Klio's spectrum was calculated (Figure 22) and has an R^2 value of ~0.97913 and a root mean square error of ~0.0055, these values are slightly higher than what was measured in (19) Fortuna, which indicates that (84) Klio spectrum has slightly more noise when compared to (19) Fortuna. (84) Klio's only measurable feature in the available spectrum is a strong feature centered at 0.69 ± 0.1-µm. The strong 0.7-µm feature is consistent with the 0.7-µm feature in both (13) Egeria and (19) Fortuna and is likely also produced by an oxidized iron phyllosilicate exhibiting electronic exchange (Vilas & Sykes, 1996).

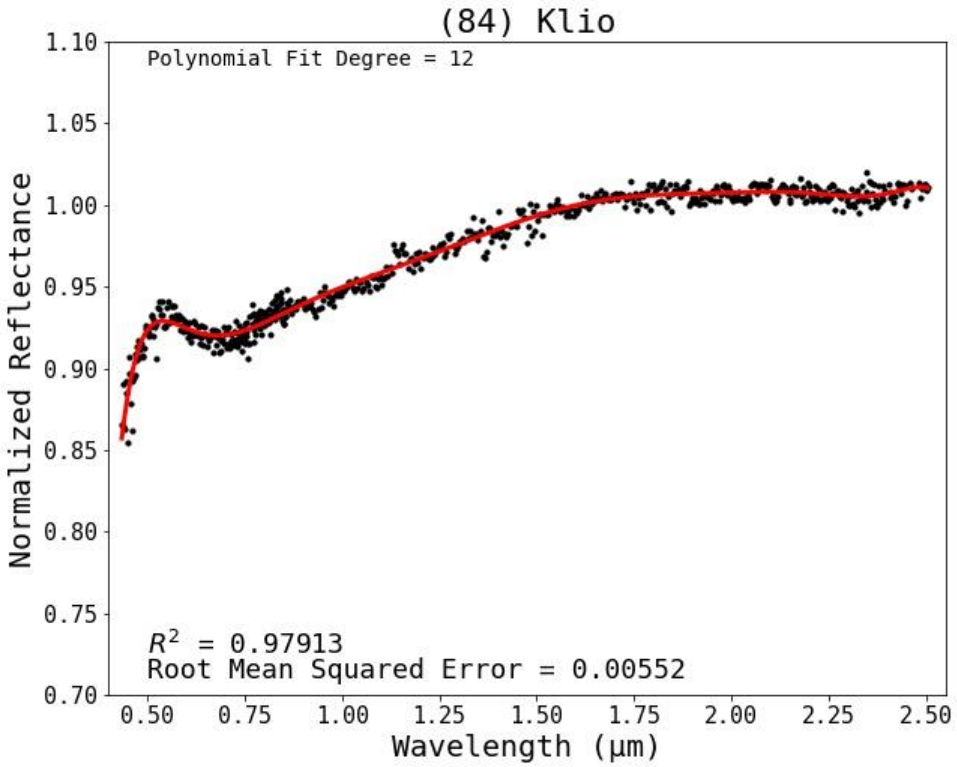

Figure 22. The red line indicates the 12th degree polynomial function calculated from the spectrum of (84) Klio. The R-squared value between the polynomial fit and (84) Klio's spectrum was determined to be ~0.97913, and the root mean squared error is ~0.0055.

4.5: (130) ELEKTRA

(130) Elektra has multiple measurable features throughout the VNIR. The spectrum is similar to (19) Fortuna's and (84) Klio's in both slope and feature intensity. The 0.7-μm feature is shifted slightly redward to 0.74 ± 0.01-μm in (130) Elektra's spectrum, though the 0.95- and the 1.25-μm features are shifted slightly blueward when compared to (13) Egeria's and (19) Fortuna's. The discussed features are located at 0.92 ± 0.01-μm and 1.22 ± 0.05-μm, respectively. (130) Elektra also exhibits a feature centered at 2.33 ± 0.01-μm.

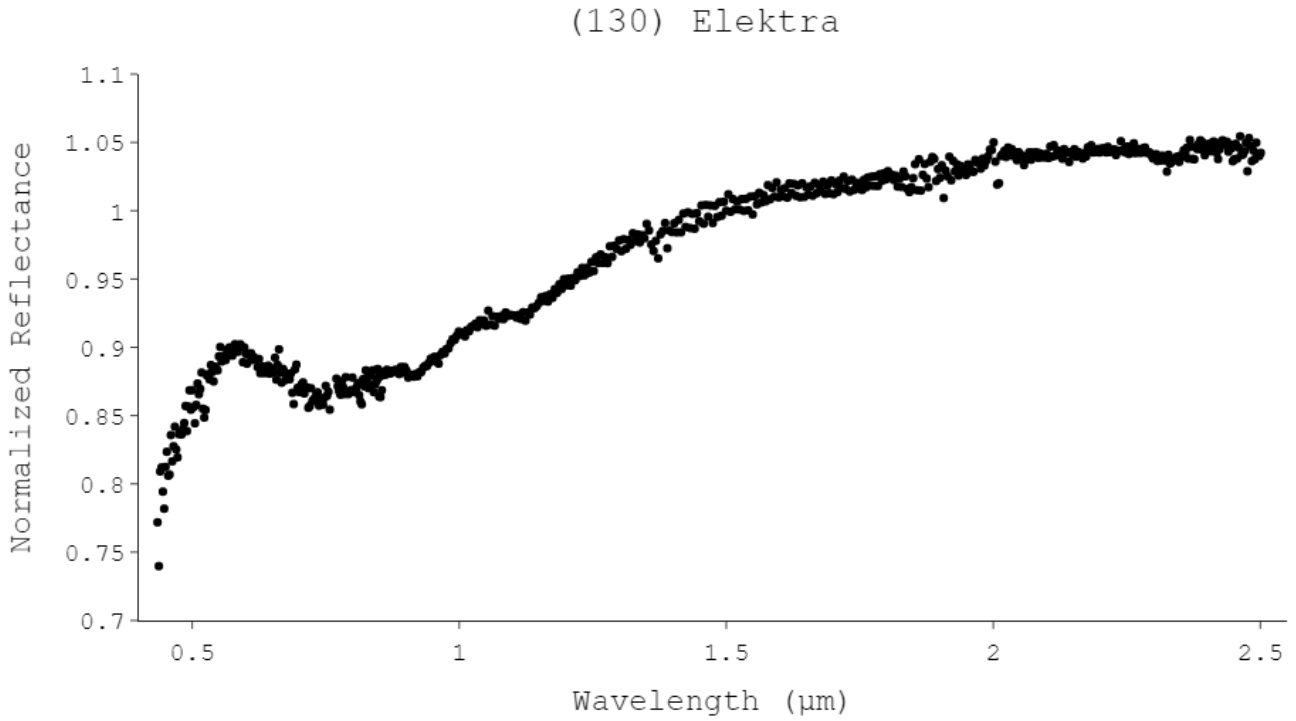

Figure 23. VNIR spectra of (130) Elektra, produced by combining and normalizing SMASS-II visible CCD data (R. P. Binzel et al., 1993), and IRTF SpeX NIR data acquired and calibrated and uploaded to the planetary data science system (Reddy & Sanchez, 2016)

(130) Elektra exhibits a steep UV slope, typical of the G-class asteroids, which is followed by a strong 0.7-μm feature. Throughout the NIR, there are multiple measurable subtle features with the band centers reported in Table 4.

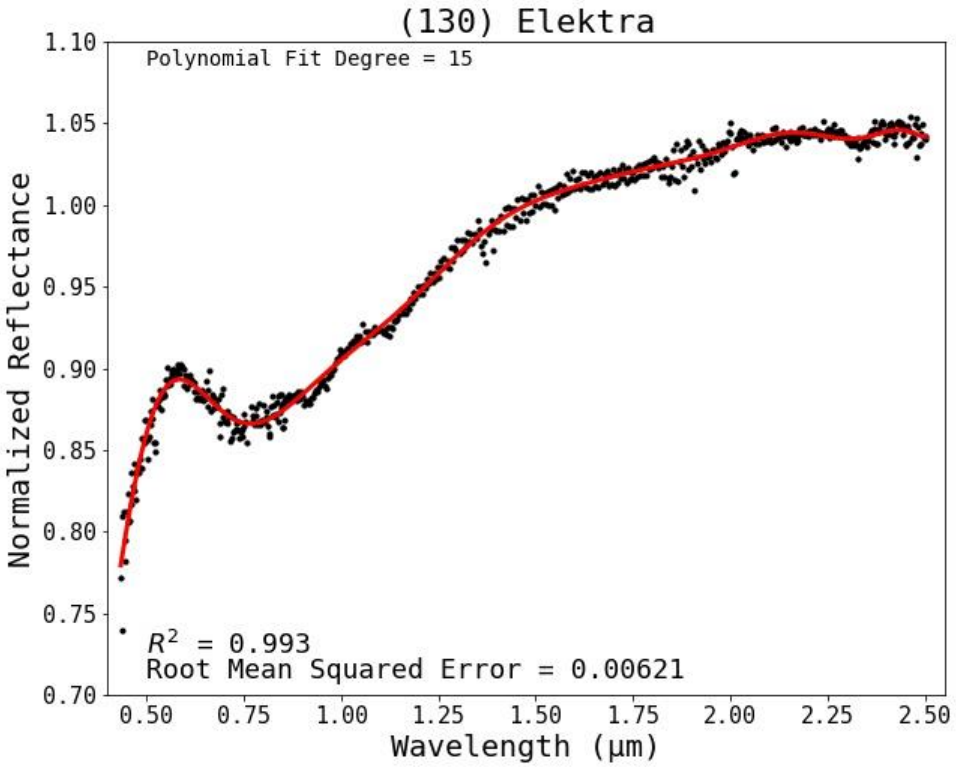

Figure 24. The red line indicates the 14th degree polynomial function calculated from the spectrum of (130) Elektra. The R-squared value between the polynomial fit and (130) Elektra's spectrum was determined to be ~0.993, and the root mean squared error is ~0.006.

A 15th-degree polynomial regression of (130) Elektra's spectrum was calculated (Figure 24), and (130) Elektra's spectrum was determined to have an R^2 value of 0.993 and a root mean square error of ~0.006, these values are higher than what was calculated for (19) Fortuna, which indicates that (130) Elektra's spectrum exhibits higher rates of noise when compared to (19) Fortuna. The feature located at 0.74-μm is still likely produced by an oxidized iron phyllosilicate, as the feature shape and depth are similar to the 0.7-μm feature in both (13) Egeria and (19) Fortuna. King & Clark (1989) reported a shift of approximately 0.04-μm longward in phyllosilicate minerals when the grain size was reduced from 104-105-μm to <30-μm in a laboratory study of serpentine and chlorites. Therefore, subtle features at 0.7- are likely produced

by the same surface products found the asteroids (19) Fortuna and (13) Egeria, though (130) Elektra may have smaller surface mineral grains. A feature at 2.3-µm has been associated with a combination of OH band fundamental stretch within either AL-O-H or Mg-O-H. Hunt & Ashley (1979) observed that when the 2.3-µm feature is present and there is a lack of a 2.2-µm feature, this combination indicates that the 2.3-µm feature is associated with the bending fundamental of Mg-O-H that commonly occurs in the mineral phlogopite, a monoclinic phyllosilicate closely related to biotite with a general formula of $KMg_3(AlSi_3O_{10})(OH)_2$. Notably, phlogopite has been detected in small quantities in CV and Enstatite meteorites (Lorenz et al., 2003; Rubin, 1997).

CHAPTER V DISCUSSION

5.1: 0.7-µm ABSORPTION BAND

The 0.7-µm feature was detected in all asteroids investigated except (1) Ceres. This feature has been investigated thoroughly in multiple studies (M. A. Barucci et al., 1997; Sawyer, 1991; Vilas et al., 1993; Vilas & Gaffey, 1989; Vilas & Sykes, 1996, and more). The 0.7-µm feature has been associated with hydrated minerals more specifically with $Fe^{2+} \rightarrow Fe^{3+}$ electron charge transfer in oxidized iron phyllosilicates (Vilas & Gaffey, 1989). Vilas and Sykes (1996) also determined that the 0.7-µm feature substantially subdues when heated to temperatures above 400 °C, as the hydrated minerals are dehydrated, halting the oxidized iron charge transfer responsible for feature production. (1) Ceres' lacking the 0.7-µm feature indicates that its phyllosilicate minerals have experienced more substantial heating. It is also possible that (1) Ceres' surface minerals have been thoroughly dehydrated through other means, or that the asteroid is devoid of concentrated Fe-phyllosilicate minerals at its surface.

5.2: 0.95-µm ABSORPTION BAND

The 0.95-µm feature was measurable in (13) Egeria, (19) Fortuna, and (130) Elektra and may be present in (84) Klio, though it was absent in asteroid (1) Ceres. While the two common silicates, olivine and pyroxene, have been well-documented in producing a feature between 0.9 and 1.0-µm in S-class asteroids (Gaffey, 2002; Gaffey, 2010; M. Gaffey et al., 1993), these minerals are not likely to be responsible for the aforementioned 0.95-µm absorption feature. As the pyroxene/olivine 1-µm band is almost always associated with a second band near 2-µm, the pyroxene/olivine bands also exhibit a much greater intensity and extend over a wider spectral range than the 0.95-µm feature identified in the studied asteroids does.

S. Gaffey (1993) and Hunt (1977) reported that the second overtone of the O-H stretching modes occurs in the 0.9-µm region in organic molecules, though it is more likely that a hydroxyl-bearing mineral is responsible for the subtle 0.95-µm feature. While the 0.95-µm feature has been related to brucite, a magnesium hydroxide mineral (De Angelis et al., 2016), it was only caused by brucite at extremely high concentrations. Furthermore, the more diagnostic ~2.45-µm feature identified does not appear to be present in any spectrum presented in this study. A more likely hydroxide mineral responsible for the 0.95-µm feature is goethite, which produces an absorption at 0.94-µm and exhibits Fe electron exchange (Hunt & Ashley, 1979). Goethite has also been suggested as a possible source for the ~3-µm feature on other C-complex asteroids, including 24-Themis (Beck et al., 2011).

5.3: 1.14-µm ABSORPTION BAND

The 1.14-µm feature was measured in both (13) Egeria and (19) Fortuna and possibly present (84) Klio and (130) Elektra. This feature was well-defined in (13) Egeria's and (19) Fortuna's spectra. Neither electron transitions nor OH-vibrational transitions have been documented to create an absorption at ~1.14-µm. However, molecules commonly associated with organics, such as CH combinations and NH combinations, have been reported to produce features between 1.1- and 1.2-µm (S. Gaffey, 1993). Ammoniated phyllosilicates have become a prime candidate for the production of the absorptions at the 3.0-µm region on asteroid (1) Ceres (see Chapter 4.7.2). Carbon has also been identified on multiple C-complex asteroids, most notably near-Earth asteroids such as (101955) Bennu (Kaplan et al., 2020). C-H may be produced on asteroids when carbonaceous material interacts with low energy thermal protons, though it is still uncertain if this process occurs on C-complex asteroids (Muñoz Caro et al., 2001). If ammonia and carbon are prevalent on (1) Ceres and other C-complex asteroids, we

should expect these materials to be present on G-class asteroids as well. However, due to a difference in geologic history and physical properties of individual asteroids, ammonia and carbon molecules may be harbored within different materials. For example, organic ammoniated organic molecules were likely produced in the early protoplanetary disc and were incorporated into asteroids along with other materials during accretion (Pizzarello & Williams, 2012). (1) Ceres may have later transferred much of its ammonia from organics into phyllosilicate minerals through processes such as cation exchange capacity, as suggested by De Sanctis et al. (2015). However, smaller G-class asteroids, such as the other four studied, did not exhibit the thermal energy required to transfer ammonia to phyllosilicate minerals, preserving their ammoniated organic molecules.

5.4: 1.25-µm ABSORPTION BAND

A subtle, narrow feature at ~1.2-µm was measured in both (13) Egeria and (130) Egeria. Neither O-H vibrations in phyllosilicates nor electron transfer have been reported to produce a feature near 1.2-µm. S. Gaffey (1993) reported that some CH, NH, and OH combinations produce features near ~1.2-µm, and Berg et al. (2016) also identified that ammoniated sulfates can produce features between 1.23- and 1.27-µm. Ammonia and carbon compounds and minerals have been identified in C-complex asteroids and carbonaceous meteorites. Therefore, the detection of ammonia should be expected in G-class asteroids.

5.5: 1.4-µm ABSORPTION BAND

The 1.4-µm feature was measured in both (13) Egeria and (19) Fortuna and may be present in (84) Klio. Much like the 0.95-µm feature the 1.4-µm feature, is also produced by O-H stretching modes in many hydroxides and hydrated minerals (S. Gaffey, 1993; Hunt & Ashley,

1979; Hunt, 1979; King & Clark, 1989). Sharp narrow features, much like those observed in (13) Egeria, are indicative of phyllosilicate minerals. While the 1.4-µm feature is common to all OH-bearing minerals, its specific appearance and location vary slightly in different minerals and end-members (Hunt & Ashley, 1979; Hunt, 1979; King & Clark, 1989). (13) Egeria and (19) Fortuna exhibit slightly different band centers at 1.40 ± 0.01- and 1.44 ± 0.01-µm, respectively. Hunt (1979) reported that kaolinite's [$Al_2(Si_2O_5)(OH)_4$] 1.4-µm band is composed of three separate minima in close proximity, with the deepest occurring at 1.394-µm and the shallowest occurring at 1.413-µm. Pyrophyllite [$Al_2Si_4O_{10}(OH)_2$] also exhibits similar habits. The Al-phyllosilicate band geometry matches very well with what is observed in (13) Egeria's 1.4-µm spectrum, which appears to be composed of multiple minima and an overall band center at 1.40 ± 0.01-µm.

King and Clark (1989) identified that both serpentine and chlorite group minerals produce bands at 1.4-µm as well, though some chemistries of chlorite produce doublets with a shoulder longward of the main feature. However, the details in the 1.4-µm band produced by chlorite were only resolved in spectra with a resolution of 0.00125-µm and were centered near 1.38-µm. Therefore, it would appear to be unlikely that (13) Egeria's 1.4-µm observed feature shape is the result of chlorite minerals. These band centers coincide with the atmospheric water vapor bands, so residual water vapor information may still be affecting the absorption's band center and shape.

5.6: 1.9-µm ABSORPTION BAND

The 1.9-µm feature was only measured in (13) Egeria. While (19) Fortuna and (130) Elektra did express a higher rate of noise throughout a similar spectral range, there was no measurable feature curve in their spectral distribution. A feature, or noise, can occur in the final spectrum when water vapor information is not fully removed from the spectral distribution

during the spectral reduction process. If it is entertained that the feature observed in (13) Egeria is produced by minerals on the surface of the asteroid, residual telluric features may still be affecting its shape or band center. Much like the 1.4-µm feature, the 1.9-µm feature is produced by O-H group minerals, which commonly occur in phyllosilicate minerals. However, the 1.9-µm feature is always produced by H_2O, regardless if the water is free or incorporated into the mineral's structure. A mineral that readily absorbs water, montmorillonite, produces a strong 1.9-µm feature when saturated. However, other phyllosilicates, such as kaolinite have also been recorded to exhibit a 1.9-µm feature, though at a weaker intensity (Hunt & Ashley, 1979). Regardless of the specific mineral, the presence of a 1.9-µm feature indicates the presence of H_2O.

5.7: 2.3-µm ABSORPTION BAND

A subtle 2.3-µm feature was measurable in (130) Elektra. The 2.3-µm feature has also been associated with the O-H stretch fundamental in hydrated minerals. Hunt and Ashley (1979) reported that this feature is common in phyllosilicate minerals and is usually associated with a feature at 2.2-µm. Hunt and Ashley identified that when the 2.3-µm feature is present in the absence of a feature at 2.2-µm, this situation indicates that the OH-stretching mode is occurring between Mg-O-H, rather than between Al-O-H; such processes commonly occur in phlogopite. This same spectral characterization was later reported to occur in both Mg-rich chlorite and serpentine by King and Clark (1989), indicating that Al-phyllosilicates are more likely to produce absorptions at 2.2-µm and 2.3-µm, while Mg-phyllosilicates commonly produce a single feature at 2.3-µm. Since both kaolinite and pyrophyllite are Al-phyllosilicates, they produce an absorption near 2.2-µm, since (13) Egeria does not exhibit a measurable 2.2-µm feature this would indicate that the 1.4-, and 1.9-µm features are not indicative of Al-rich phyllosilicates such

as kaolinite and pyrophyllites and are instead the result of Mg-rich phyllosilicates such as chlorite and serpentine.

5.8: GEOLOGIC INTERPRETATION OF THE STUDIED ASTEROIDS

Besides (1) Ceres, all asteroids studied shared similar absorption features, and (19) Fortuna, (84) Klio, and (130) Elektra contained similar spectral slopes and band intensity, while (13) Egeria showed much stronger absorptions than the other three asteroids with hydration features did. This inconsistency may be due to differences in either physical properties or surface minerals with dissimilar chemistries. Table 5 details the physical properties of the investigated asteroids.

Table 5. Physical characteristics of the studied asteroids.

Asteroid	Albedo	Dimensions (km)	Mean Density (g/cm^3)
(1) Ceres	0.1132 ± 0.005	975 x 975 x 909 ± 3.6	2.06 ± 0.05
(13) Egeria	0.0825 ± 0.007	208 x 208 x 208 ± 4.150	3.38 ± 1.01
(19) Fortuna	N/A	225 x 205 x 195 ± 6	1.36 ± 0.32
(84) Klio	0.0527 ± 0.002	77.097 ± 1.851	N/A
(130) Elektra	0.0762 ± 0.11	108 x 108 x 108 ± 7.5	1.30 ± 0.30

Table material adapted from the following:

Dimensions and density: Baer, J., Chesley, S., and Britt, D., Eds. (2012) Asteroid Masses V3.0. EAR-A-COMPIL-5-ASTMASS-V3.0. NASA Planetary Data System.

Albedo values: Davis, D.R. and Neese, C., Eds. (2002) Asteroid Albedos. EAR-A-5-DDR-ALBEDOS-V1.1. NASA Planetary Data System.

Vilas (1994) suggests that the Tholen C-complex asteroids represent a spectrum of least hydrated to most hydrated (P → B → C → G). To explain the gradient, Vilas suggests that almost all large asteroids are essentially “rubble piles” that are either the fragmented daughter products of larger shattered asteroids or the shattered gravitationally bound remains of a similar

mass parent asteroid. This suggestion is based on a numerical model presented by Davis et al. (1989) that found that many asteroids with diameters greater than 100 km have likely been collisionally shattered and then gravitationally re-captured as "rubble piles." Since a greater amount of energy and insulation is available near the center of an asteroid, some asteroids may represent different areas along the hydrothermal gradient of a parent asteroid - with hydrated asteroids being representative of the material that was more hydrated and closer to the center, while other asteroids represent material that is less hydrated and closer to the surface. The largest asteroids such as (1) Ceres and (4) Vesta, have likely not been completely shattered and exhibit substantially less hydrated minerals at their surfaces. The results of this study support Vilas's explanation as only (1) Ceres does not exhibit the discussed hydration features, while the other "smaller" asteroids investigated do exhibit hydrated features in the VNIR. These hydrated features are likely associated with hydrated minerals that formed within the interior of an asteroid that was later disrupted as Jupiter's gravitational influence pumped up the eccentricity and inclination of planetesimals within its sphere of influence.

The results of this study confirm that (1) Ceres is spectrally disparate when compared to the other four asteroids in this study. Physically, (1) Ceres also has some key differences, such as a much brighter albedo and dimensions when compared to the other four asteroids (Table 5). The higher albedo indicates more reflective minerals at the surface of an asteroid and reflective minerals such as salts and water ice have been identified on (1) Ceres' surface. These areas are commonly found at the bottom of impact craters, likely effect (1) Ceres' overall albedo (Li et al., 2016). The presence of water ice and evaporate minerals indicates that (1) Ceres contains a "wet" core. Geologic events such as cryovolcanics (Ruesch et al., 2016), landslides, and impacts (Combe et al., 2016) can either expose (1) Ceres' subsurface material or cause it to be

transported to the surface, further altering its surface mineralogy. The described events are likely unique to (1) Ceres due to (1) Ceres' large mass and are not likely to occur on the other asteroids included in this study. More typical G-class asteroids, such as the other four studied, may exhibit hydrated minerals at the surface because they have been shattered and thoroughly mixed while remaining gravitationally bound, resulting in hydrated interior minerals being deposited at and near the asteroids' surfaces. If this is the case, hydrated minerals would be more ubiquitous and evenly distributed at the surface of G-class asteroids when compared to (1) Ceres' surface. Due to (1) Ceres' original non-altered surface minerals remaining concentrated at the surface, the hydrated material likely remains more localized and spectrally obscured in the NIR, which would explain why (1) Ceres does exhibit a 3-µm hydrated feature but lacks more subtle hydrated features between 0.4-2.70-µm.

(13) Egeria exhibits a much higher mean density, though a greater uncertainty, than (19) Fortuna does, which has similar dimensions (Table 2). (13) Egeria's density is also greater than (1) Ceres'; therefore, compaction via condensation cannot alone explain (13) Egeria's high density. (13) Egeria's high density may be caused by either a difference in mineralogy or the construction of the asteroid (i.e., solid rocky planetesimal, rather than a rubble pile). Since surface chemistry largely influences band centers (Gaffey, 2002), and the band centers for features on (13) Egeria are largely comparable to the band centers in (19) Fortuna, (130) Elektra, and (84) Klio, it is unlikely that (13) Egeria exhibits a significant disparity in mineralogy when compared with the other G-class asteroids exhibiting hydrated features. (13) Egeria does exhibits spectral bands with much greater intensity and a flatter slope than the other G-class asteroids with hydration features in the VNIR do. Larger particle size has been shown to increase an absorption feature intensity as the penetration depth of the incident light increases (Cloutis et al.,

2013; Hiroi et al., 1994; Mustard & Hays, 1997). It has also been well-documented that larger surface particles may also result in bluer and darker sloped NIR spectra (Binzel et al., 2015; Cloutis et al., 2011; Johnson & Fanale, 1973), (13) Egeria clearly exhibits a bluer slope past ~1.0-μm when compared to the other hydrated asteroids in this study, so it could be possible that (13) Egeria may exhibit larger surface particles. (13) Egeria being composed of either a single or multiple non-shattered solid hydrated mantle portions could also explain its higher density and more intense features when compared to the other hydrated asteroids in this study. It should be stated that this assumption is highly speculative and calculating an asteroid's density relies on mass and volume estimations, most of which have high uncertainties. Further dynamical studies or future space missions may show that (13) Egeria's density is not abnormally high when compared to similar asteroids, though with the current information available in the literature it would appear to be so.

(19) Fortuna, (84) Klio, and (130) Elektra all exhibit similar spectral slopes and band centers throughout the VNIR spectral range. These asteroids likely represent fine-grained, hydrated surface minerals that have been heavily altered by space weathering, resulting in subtle features and a reddened NIR slope. The hydrated minerals were likely produced in a wet interior of either a larger parent asteroid or a parent asteroid similar in size. The parent asteroid was shattered either through direct impact or gravitational perturbations related to Jupiter. The shattered material that now composes the asteroid remained gravitationally bound, though thoroughly mixed. The material was eventually re-condensed as a loose rubble-pile which explains the relatively low densities exhibited in (19) Fortuna and (130) Elektra. These two asteroids also exhibit a similar albedo, providing more evidence that these asteroids are mineralogically and structurally similar to each other (Table 5). However, (130) Elektra does

exhibit a 0.7-µm band that is approximately shifted 0.05-µm redward and a 2.3-µm band shifted 0.03-µm in the same direction when compared to the other asteroids with hydrated features.

5.9: POSSIBLE SURFACE MINERALS

The 0.7- and 0.95-µm features measured in nearly all asteroids indicate the presence of a Fe-rich hydroxyl or H_2O-bearing mineral. Hematite and goethite both produce a feature near 0.7-µm (Vilas et al., 1994), as well as a feature in the 0.95-µm region, with the hematite centering near 0.85-µm and goethite located at 0.94-µm (Hunt & Ashley, 1979). Spectral measurements of terrestrial goethite do produce a 0.95-µm band that is more intense than the 0.7-µm band (Morris et al., 1985; Townsend, 1987; Vilas et al., 1994); however, this occurrence is not observed in the three asteroids studied with a measurable 0.95-µm feature. The intensity of the 0.95-µm band could be affected by either the other minerals on the surface of the asteroid masking its intensity or by space weathering weakening reddening the features in the NIR. The presence of the 0.7-µm feature in the asteroids with hydrated features also indicates that the Fe-rich phyllosilicate minerals have not yet been heated beyond 400 °C (Vilas & Sykes, 1996).

The 1.4-, 1.9-, and 2.3-µm features are all ubiquitous OH and H_2O vibrations in phyllosilicate minerals, and the 1.4-, and 2.3-µm features are associated with O-H vibration transitions. Aluminum-rich phyllosilicates, such as kaolinite, are not likely to be responsible for the 2.3-µm feature observed in (19) Fortuna, (84) Klio, and (130) Elektra, as the Al-O-H stretch creates features closer to 2.2-µm. However, the Mg-O-H stretch produces a feature centered closer to 2.3-µm (S. Gaffey, 1993; King & Clark, 1989). Mg-rich hydrated minerals - such as serpentine, chlorite, montmorillonite, and brucite - can be produced via aqueous alteration of Mg-rich primary minerals such as olivine (Frost & Kloprogge, 1999). The only asteroid with a pronounced 1.9-µm feature is (13) Egeria, because montmorillonite readily absorbs water, which

is responsible for the 1.9-μm feature, it should be considered as a possible surface component on (13) Egeria. While work has been done to identify the subtle discrepancies between specific phyllosilicate's 1.4-μm feature, much of the differences observed in telescopic observations are too subtle to detect with current spectroscopic resolution (King & Clark, 1989). The 1.4- and 1.9-μm bands are also heavily influenced by atmospheric water vapor. While the reduction aims to remove the information not related to the asteroids, residual information may be capable of affecting the final feature band center or feature shape. While kaolinite spectra may most closely match the 1.4-μm feature seen in (13) Egeria, the lack of a 2.2-μm feature would disqualify a strong presence of kaolinite at the surface of any of the observed asteroids. The slight differences in band centers at 1.4-μm between (13) Egeria and (19) Fortuna seem to suggest slightly different mineral chemistry as well, consistent with the conclusion of Burbine (1998).

While ammoniated phyllosilicates have been suggested as being responsible for the 3-μm band on (1) Ceres (De Sanctis et al., 2015; King et al., 1992), no absorptions related to ammoniated minerals noted by Ferrari et al. (2019) were identified, which is not abnormal for data collected via ground-based instruments. However, absorption bands measured at 1.14- and 1.25-μm may be related to CH or NH compounds in organic materials, which could either be actively produced on the surface of the asteroid by interaction with low energy thermal photons (Muñoz Caro et al., 2001) or be left over from the protoplanetary disc. If this relationship is assumed to be true, then evidence may suggest that ammoniated molecules have not yet been transferred to ammoniated minerals through interlayer cation exchange processes driven by heating (Borden & Giese, 2001).

CHAPTER VI: CONCLUSIONS

This study demonstrates that features can be detected and measured in the VNIR spectral range of G-class asteroids with the IRTF and upgraded SpeX instrument. The identified features at 0.7-μm, 0.95-μm, 1.4-μm, 1.9-μm, and 2.3-μm are relatable to hydrated minerals, with the 0.7- and 95-μm features likely related to similar electronic exchange processes in Fe-rich phyllosilicates, and 1.4-, 1.9-, and 2.3-μm features related to O-H vibration transitions. Features that were not able to be directly related to hydrated minerals were identified at 1.14- and 1.25-μm in (130) Elektra, (13) Egeria, and (19) Fortuna. These features may be related to CH or NH compounds incorporated in organic compounds or surface minerals. Other investigations, covered in this study, have identified ammoniated phyllosilicate minerals to be responsible for the absorptions in the 3.0-μm region of (1) Ceres, as well as high rates of carbon on other C-complex asteroids. Therefore, it should be expected to detect features related to these compounds on other asteroids.

This study shows that (1) Ceres is spectrally disparate from the other four G-class asteroids studied in the NIR spectral regime. This difference is most likely due to (1) Ceres exhibiting dissimilar surface mineralogy and geologic history when compared to the other asteroids studied. Spectral analysis and spacecraft investigations indicate that (1) Ceres does contain ammoniated Mg-rich phyllosilicates at its surface, though the hydration features shortward of 2.7-μm is not detected. This lack of detection could be due to either the features being masked by an opaque surface component that is not present at the same concentration on the other studied asteroids or an indication of phyllosilicate dehydration, which is not likely as the 3.0-μm features are present. A component capable of masking the hydration features in the NIR could be magnetite, which can be produced by further alteration of serpentine or a dark

carbon component. (1) Ceres' hydrated minerals are likely produced in its wet mantle and transported to the surface via cryovolcanics or impact events. (1) Ceres also lacks a 0.7-µm feature, indicating either a poor Fe concentration in hydrated surface minerals or that its oxidized Fe phyllosilicates have been heated beyond ~400 °C resulting in dehydration of oxidized Fe phyllosilicates and production of ammoniated phyllosilicate materials.

The other four asteroids investigated all exhibit strong 0.7-µm features, indicating a much higher concentration of oxidized Fe phyllosilicates. Dynamical models indicate that asteroids > 100 km in size have likely suffered catastrophic impact events due to the gravitational perturbations from Jupiter. The shattering and reconstitution of the material would explain how hydrated minerals were deposited on the surface of G-class asteroids that lack surface processes. Asteroid differentiation would ultimately be halted after recondensation, as the shattered asteroid is more representative of a rubble pile, resulting in a low density and relatively small mass not providing enough energy for further mineral alteration or the asteroids ^{26}Al deposits having been thoroughly depleted. (13) Egeria exhibits a higher density than all other studied asteroids, perhaps due to (13) Egeria being composed of larger surface particles that are mineralogically similar to (19) Fortuna, (84) Klio, and (130) Elektra. However, (13) Egeria's band centers do suggest slightly different chemistry, such as possibly a higher concentration of montmorillonite, as suggested by its 1.9-µm band.

Identifying specific phyllosilicate chemistries from the recorded spectral features is challenging, as many phyllosilicate minerals produce features with similar shapes and band centers. This similarity is because nearly all phyllosilicate absorption features are produced by O-H vibrations and cation electronic exchanges both occur in nearly all phyllosilicate minerals. It was stated earlier that asteroids with a 0.7-µm feature likely have a higher concentration of

oxidized Fe-phyllosilicates. The lack of a 2.2-μm feature accompanying the 2.3-μm feature would indicate that if phyllosilicate minerals are responsible for the measured absorptions, they lack aluminum, which would be expected from alteration products of mafic primary minerals. The phyllosilicate presence on the surface likely represents a high Fe concentration hydroxyl-bearing mineral component such as goethite and hematite, along with an Mg-rich hydrated mineral such as serpentine, chlorite, montmorillonite, or brucite. Spectral resolution limitations of the SpeX spectrograph and atmospheric interference make it impossible to resolve diagnostic discrepancies in the 1.4-μm region, though discrepancies have been identified in spectra with a resolution of 0.00125-μm. However, the positive slope, and subtle absorption intensities of (19) Fortuna, (84) Klio, and (130) Elektra do not match the overall negative slope and strong intensities measured in lab studies of phyllosilicates. These spectral characteristics are heavily affected by space weathering, temperature, and grain size in the NIR spectral regime. Therefore, this study primarily relied on band center measurements for mineral correlations and interpretations. This study's results bolster the findings of Burbine (1998), in identifying that there are major spectral disparities between some G-class asteroid members, as well as evidence for slightly different chemistry between (13) Egeria and (19) Fortuna. This study also agrees with Vilas et al. (1994) that G-class asteroids are likely to include a 0.7-μm feature as well as being representative of highly aqueously altered mafic material.

6.2: FUTURE WORK

While the VNIR spectral regime of the C-complex asteroids had been assumed to be relatively featureless for the past 70 years of scientific investigation, this study shows that with modern spectrographic equipment, and careful data reduction techniques, there is a multitude of information available in the VNIR spectral regimes of the C-complex asteroids. However, only a

small sample of all G-class asteroids was investigated for this study. The entire G-class asteroid population should be investigated to establish what spectrographic properties are representative of the G-class, as well as to identify any other outliers, such as (1) Ceres. These asteroids should also be investigated in longer wavelengths to determine if there is a correlation between the features present between 0.4-2.5-µm and features in the 3.0-µm region. Finally, investigations into the other C-complex asteroids should also be undertaken to determine if features can be identified and correlated with possible surface minerals. This determination may help to bolster or dismiss the assumption that the G-class asteroids are the most hydrated C-complex asteroids, as well as build a greater understanding of C-complex asteroids' chemistries and geologic histories.

REFERENCES

Adams, J. B., & Jones, R. L. (1970). Spectral Reflectivity of Lunar Samples. *Science, 167*(3918), 737. https://doi.org/10.1126/science.167.3918.737

Adams, J. B. (1974). Visible and near-infrared diffuse reflectance spectra of pyroxenes as applied to remote sensing of solid objects in the solar system. *Journal of Geophysical Research (1896-1977), 79*(32), 4829–4836. https://doi.org/10.1029/JB079i032p04829

Adams, J. B., & Filice, A. L. (1967). Spectral reflectance 0.4 to 2.0 microns of silicate rock powders. *Journal of Geophysical Research (1896-1977), 72*(22), 5705–5715. https://doi.org/10.1029/JZ072i022p05705

Akai, J. (1988). Incompletely transformed serpentine-type phyllosilicates in the matrix of Antarctic CM chondrites. *Geochimica et Cosmochimica Acta, 52*(6), 1593–1599. https://doi.org/10.1016/0016-7037(88)90228-1

Allégre, C. J., Birck, J. L., Fourcade, S., & Semet, M. P. (1975). Rubidium-87/Strontium-87 Age of Juvinas Basaltic Achondrite and Early Igneous Activity in the Solar System. *Science, 187*(4175), 436–438. https://doi.org/10.1126/science.187.4175.436

Ammannito, E., Desanctis, M. C., Ciarniello, M., Frigeri, A., Carrozzo, F. G., Combe, J. P., Ehlmann, B. L., Marchi, S., McSween, H. Y., Raponi, A., Toplis, M. J., Tosi, F., Castillo-Rogez, J. C., Capaccioni, F., Capria, M. T., Fonte, S., Giardino, M., Jaumann, R., Longobardo, A., … Russell, C. T. (2016). Distribution of phyllosilicates on the surface of Ceres. *Science*. https://doi.org/10.1126/science.aaf4279

Angström, A. J. (1855). XLVIII. Optical researches. *The London, Edinburgh, and Dublin Philosophical Magazine and Journal of Science*, 9(60), 327–342. https://doi.org/10.1080/14786445508641880

Barucci, M. A., Doressoundiram, A., Fulchignoni, M., Florczak, M., Lazzarin, M., Angeli, C., & Lazzaro, D. (1997). *Search for Aqueous Altered Materials on Asteroids*. *29*, 07.15.

Barucci, M. Antonietta, Capria, M. T., Coradini, A., & Fulchignoni, M. (1987). Classification of asteroids using G-mode analysis. *Icarus, 72*(2), 304–324. https://doi.org/10.1016/0019-1035(87)90177-1

Beatty, J. K. (1990). *The New Solar System* (A. Chaikin, Ed.; 3rd edition). Sky Pub Corp.

Beck, P., Quirico, E., Sevestre, D., Montes-Hernandez, G., Pommerol, A., & Schmitt, B. (2011). Goethite as an alternative origin of the 3.1 μm band on dark asteroids. *Astronomy and Astrophysics, 526*, A85. https://doi.org/10.1051/0004-6361/201015851

Beck, P., Schmitt, B., Cloutis, E. A., & Vernazza, P. (2015). Low-temperature reflectance spectra of brucite and the primitive surface of 1-Ceres? *Icarus, 257*, 471–476. https://doi.org/10.1016/j.icarus.2015.05.031

Beletic, J. W. (2005). Optical and Infrared Detectors for Astronomy. In R. Foy & F. C. Foy (Eds.), *Optics in Astrophysics* (pp. 123–154). Springer Netherlands. https://doi.org/10.1007/1-4020-3437-7_11

Bell, J. F., Owensby, P. D., Hawke, R. B., Brown, R. H., Cruikshank, D. P., & Hartman, W. K. (1995). 52-color Asteroid Survey. EAR-A-RDR-3-52COLOR-V2.1. NASA Planetary Data System.

Berg, B. L., Cloutis, E. A., Beck, P., Vernazza, P., Bishop, J. L., Takir, D., Reddy, V., Applin, D., & Mann, P. (2016). Reflectance spectroscopy (0.35–8μm) of ammonium-bearing minerals and qualitative comparison to Ceres-like asteroids. *Icarus*, *265*, 218–237. https://doi.org/10.1016/j.icarus.2015.10.028

Binzel, R. P., Xu, S., Burbine, T. H., & Bus, S. J. (1993). Small Main-Belt Asteroid Spectroscopic Survey. In *Bull. Amer. Astr. Soc.* (Vol. 25, p. 1135).

Binzel, Richard P., Barucci, M. A., & Fulchignoni, M. (1991). The Origins of the Asteroids. *Scientific American*, *265*(4), 88–95.

Binzel, Richard P., DeMeo, F. E., Burt, B. J., Cloutis, E. A., Rozitis, B., Burbine, T. H., Campins, H., Clark, B. E., Emery, J. P., Hergenrother, C. W., Howell, E. S., Lauretta, D. S., Nolan, M. C., Mansfield, M., Pietrasz, V., Polishook, D., & Scheeres, D. J. (2015). Spectral slope variations for OSIRIS-REx target Asteroid (101955) Bennu: Possible evidence for a fine-grained regolith equatorial ridge. *Icarus*, *256*, 22–29. https://doi.org/10.1016/j.icarus.2015.04.011

Binzel, Richard P, Gaffey, M. J., Thomas, P. C., Zellner, B. H., Storrs, A. D., & Wells, E. N. (1997). Geologic Mapping of Vesta from 1994 Hubble Space Telescope Images. *Icarus*, *128*(1), 95–103. https://doi.org/10.1006/icar.1997.5734

Binzel, Richard P., Rivkin, A. S., Stuart, J. S., Harris, A. W., Bus, S. J., & Burbine, T. H. (2004). Observed spectral properties of near-Earth objects: Results for population distribution, source regions, and space weathering processes. *Icarus*, *170*(2), 259–294. https://doi.org/10.1016/j.icarus.2004.04.004

Bischoff, A. (2001). Meteorite classification and the definition of new chondrite classes as a result of successful meteorite search in hot and cold deserts. Planetary and Space Science, 49(8), 769–776.

Bischoff, A., & Geiger, T. (1995). Meteorites from the Sahara: Find locations, shock classification, degree of weathering and pairing. Meteoritics, 30(1), 113–122. https://doi.org/10.1111/j.1945-5100.1995.tb01219.x

Bloss, F. D. (1971). *Crystallography and crystal chemistry*. Holt, Rineheart, Winston. https://agris.fao.org/agris-search/search.do?recordID=US201300472820

Borden, D., & Giese, R. (2001). Baseline Studies of the Clay Minerals Society Source Clays: Exchange Capacity Measurements by the Ammonia-Electrode Method. *Clays and Minerals*, *49*(5), 441–445.

Bottke, W., Vokrouhlicky, D., Nesvorny, D., & Shrbeny, L. (2010). (6) Hebe Really is the H Chondrite Parent Body. *American Astronomical Society, DPS meeting #42*, 46.06.

Bourtembourg, R. (2012). Messier's Missed Discovery of Pallas in April 1779: *Journal for the History of Astronomy*. https://doi.org/10.1177/002182861204300205

Bowell, E., Chapman, C. R., Gradie, J. C., Morrison, D., & Zellner, B. (1978). Taxonomy of asteroids. *Icarus*, *35*(3), 313–335. https://doi.org/10.1016/0019-1035(78)90085-4

Bowles, J. F. W. (2021). Hydroxides. In D. Alderton & S. A. Elias (Eds.), *Encyclopedia of Geology (Second Edition)* (pp. 442–451). Academic Press. https://doi.org/10.1016/B978-0-08-102908-4.00162-4

Bragg, W. L. (1937). *Atomic structure of minerals*. Cornell University Press. https://agris.fao.org/agris-search/search.do?recordID=US201300222939

Brealey, A. (1995). Aqueous alteration and brecciation in Bells, an unusual, saponite-bearing, CM chondrite. *Geochimica et Cosmochimica Acta*, *59*(11), 2291–2317. https://doi.org/10.1016/0016-7037(95)00107-B

Brezina, A. (1904). The arrangement of collections of meteorites. Proceedings of the American Philosophical Society, 43(176), 211–247.

Brouwer, D., & Woerkom, A. J. J. van. (1950). *The Secular Variations of the Orbital Elements of the Principal Planets* (Vol. 13). U.S. Government Printing Office.

Bruckenthal, E. A., & Singer, R. B. (1987). *Spectral Effects of Dehydration on Phyllosilicates*. *18*. http://adsabs.harvard.edu/abs/1987LPI....18..135B

Brunetto, R., Loeffler, M., Nesvorný, D., Sasaki, S., & Strazzulla, G. (2015). Asteroid Surface Alteration by Space Weathering Processes. In *Asteroids IV*. The University of Arizona Press. https://doi.org/10.2458/azu_uapress_9780816532131-ch031

Bruno, T. J., & Svoronos, P. D. N. (2005). *CRC Handbook of Fundamental Spectroscopic Correlation Charts*. CRC Press.

Brydon, H. B. (1940). Visual Photometry of Variable Stars. *Journal of the Royal Astronomical Society of Canada*, 34, 409.

Burbine, T. H. (1998). Could G-Class asteroids be the parent bodies of CM chondrites. *Meteoritics and Planetary Science*, *33*(2), 253–258.

Burbine, T. H., Buchanan, P. C., Binzel, R. P., Bus, S. J., Hiroi, T., Hinrichs, J. L., Meibom, A., & McCoy, T. J. (2001). Vesta, Vestoids, and the howardite, eucrite, diogenite group:

Relationships and the origin of spectral differences. *Meteoritics and Planetary Science*, *36*(6), 761–781. https://doi.org/10.1111/j.1945-5100.2001.tb01915.x

Burns, R. G. (1970). *Mineralogical Applications of Crystal Field Theory*. Cambridge University Press.

Burns, R. G. (1993). *Mineralogical Applications of Crystal Field Theory.* Second Edition Cambridge University Press.

Bus, S. J., & Binzel, R. P. (2002). Phase II of the small main-belt asteroid spectroscopic survey. The observations. *Icarus*, *158*(1), 106–145. https://doi.org/10.1006/icar.2002.6857

Busigny, V., Cartigny, P., Philippot, P., & Javoy, M. (2004). Quantitative analysis of ammonium in biotite using infrared spectroscopy. *American Mineralogist*, *89*(11–12), 1625–1630. https://doi.org/10.2138/am-2004-11-1206

Calvin, W. M., & King, T. V. V. (1995). Spectral Characteristics of Fe-Phyllosilicates: Comparison to Murchison and Murray. *U.S. Geological Society Proceedings #26.* http://adsabs.harvard.edu/abs/1995LPI....26..207C

Cameron, A. G. W. (1962). The formation of the sun and planets. *Icarus*, *1*(1), 13–69. https://doi.org/10.1016/0019-1035(62)90005-2

Cameron, A. G. W., & Truran, J. W. (1977). The supernova trigger for formation of the solar system. *Icarus*, *30*(3), 447–461. https://doi.org/10.1016/0019-1035(77)90101-4

Carroll, B. W., & Ostlie, D. A. (2017). *An Introduction to Modern Astrophysics* (2nd edition). Cambridge University Press.

Carry, B., Dumas, C., Fulchignoni, M., Merline, W., Berthier, J., Hestroffer, D., Fusco, T., & Tamblyn, P. (2008). *Near-Infrared Mapping and Physical Properties of the Dwarf-Planet Ceres*. https://doi.org/10.1051/0004-6361:20078166

Cassen, P., & Moosman, A. (1981). On the formation of protostellar disks. *Icarus*, *48*(3), 353–376. https://doi.org/10.1016/0019-1035(81)90051-8

Castillo-Rogez, J. C., & McCord, T. B. (2010). Ceres' evolution and present state constrained by shape data. *Icarus*, *205*(2), 443–459. https://doi.org/10.1016/j.icarus.2009.04.008

Chang, K. (2020a, October 21). 'Literally, We Crushed It': Video Shows NASA Space Probe Touch an Asteroid. *The New York Times*. https://www.nytimes.com/2020/10/21/science/nasa-osiris-rex.html

Chang, K. (2020b, December 5). Japan's Journey to an Asteroid Ends with a Hunt in Australia's Outback. *The New York Times*. https://www.nytimes.com/2020/12/05/science/japan-asteroid-hayabusa2-woomera.html

Chapman, C. R. (1976). Asteroids as meteorite parent-bodies: The astronomical perspective. *Geochimica et Cosmochimica Acta*, *40*(7), 701–719. https://doi.org/10.1016/0016-7037(76)90024-7

Chapman, C. R. (2004). Space weathering of asteroid surfaces. *Annual Review of Earth and Planetary Sciences*, *32*(1), 539–567. https://doi.org/10.1146/annurev.earth.32.101802.120453

Chapman, C. R., Johnson, T. V., & McCord, T. B. (1971). A Review of Spectrophotometric Studies of Asteroids. *International Astronomical Union Colloquium*, *12*, 51–65. https://doi.org/10.1017/S0252921100088904

Chapman, C. R., Morrison, D., & Zellner, B. (1975). Surface properties of asteroids: A synthesis of polarimetry, radiometry, and spectrophotometry. *Icarus*, *25*(1), 104–130. https://doi.org/10.1016/0019-1035(75)90191-8

Chilton, H. T., Schmidt, B. E., Duarte, K., Ferrier, K. L., Hughson, K. H. G., Scully, J. E. C., Wray, J. J., Sizemore, H. G., Nathues, A., Platz, T., Schorghofer, N., Schenk, P. M., Landis, M. E., Bland, M., Byrne, S., Russell, C. T. R., & Raymond, C. A. (2019). Landslides on Ceres: Inferences into Ice Content and Layering in the Upper Crust. *Journal of Geophysical Research: Planets*, 1512–1524. https://doi.org/10.1029/2018JE005634

Chladni, E. (1794). *Ueber den Ursprung der von Pallas gefundenen und anderer ihr ähnlicher Eisenmassen, und über einige damit in Verbindung stehende Naturerscheinungen*. Hard Bone. http://digital.slub-dresden.de/id373202636/5

Choi, B-G., McKeegan, K. D., Leshin, L. A., & Wasson, J. T. (1997). Origin of magnetite in oxidized CV chondrites: In situ measurement of oxygen isotope compositions of Allende magnetite and olivine. Earth and Planetary Science Letters, 146(1–2), 337–349. https://doi.org/10.1016/S0012-821X(96)00229-4

Chourabi, B., & Fripiat, J. J. (1981). Determination of Tetrahedral Substitutions and Interlayer Surface Heterogeneity from Vibrational Spectra of Ammonium in Smectites. *Clays and Clay Minerals*, *29*(4), 260–268. https://doi.org/10.1346/CCMN.1981.0290403

Ciarniello, M., De Sanctis, M. C., Ammannito, E., Raponi, A., Longobardo, A., Palomba, E., Carrozzo, F. G., Tosi, F., Li, J. Y., Schröder, S. E., Zambon, F., Frigeri, A., Fonte, S., Giardino, M., Pieters, C. M., Raymond, C. A., & Russell, C. T. (2017). Spectrophotometric properties of dwarf planet Ceres from the VIR spectrometer on board the Dawn mission. *Astronomy and Astrophysics*, *598*, 1–14. https://doi.org/10.1051/0004-6361/201629490

Clark, R. N., 1980, A large scale interactive one-dimensional array processing system. *Publications of the Astronomical Society of the Pacific*, 92, p. 221-224.

Clark, R.N., 1993, SPECtrum Processing Routines User's Manual Version 3 (program SPECPR): U.S. Geological Survey Open-File Report 93-595, 210 p., https://doi.org/10.3133/ofr93595.

Clayton, R. N., & Mayeda, T. K. (1999). Oxygen isotope studies of carbonaceous chondrites. *Geochimica et Cosmochimica Acta*, 63(13), 2089–2104. https://doi.org/10.1016/S0016-7037(99)00090-3

Cloutis, E. A., Gaffey, M. J., Jackowski, T. L., & Reed, K. L. (1986). Calibrations of phase abundance, composition, and particle size distribution for olivine-orthopyroxene mixtures from reflectance spectra. *Journal of Geophysical Research: Solid Earth*, *91*(B11), 11641–11653. https://doi.org/10.1029/JB091iB11p11641

Cloutis, E. A., Hudon, P., Hiroi, T., Gaffey, M. J., & Mann, P. (2011). Spectral reflectance properties of carbonaceous chondrites: 2. CM chondrites. *Icarus*, *216*(1), 309–346. https://doi.org/10.1016/j.icarus.2011.09.009

Cloutis, E. A., Izawa, M. R. M., Pompilio, L., Reddy, V., Hiesinger, H., Nathues, A., Mann, P., Le Corre, L., Palomba, E., & Bell, J. F. (2013). Spectral reflectance properties of HED meteorites+CM2 carbonaceous chondrites: Comparison to HED grain size and compositional variations and implications for the nature of low-albedo features on Asteroid 4 Vesta. *Icarus*, *223*(2), 850–877. https://doi.org/10.1016/j.icarus.2013.02.003

Combe, J.-P., McCord, T. B., Tosi, F., Ammannito, E., Carrozzo, F. G., Sanctis, M. C. D., Raponi, A., Byrne, S., Landis, M. E., Hughson, K. H. G., Raymond, C. A., & Russell, C. T. (2016). Detection of local H2O exposed at the surface of Ceres. *Science*, *353*(6303). https://doi.org/10.1126/science.aaf3010

Coradini, A., Fulchignoni, M., Fanucci, O., & Gavrishin, A. I. (1977). A FORTRAN V program for a new classification technique: The g-mode central method. *Computers & Geosciences*, *3*(1), 85–105. https://doi.org/10.1016/0098-3004(77)90035-8

Cunningham, C. J. (2017). *Investigating the Origin of the Asteroids and Early Findings on Vesta: Historical Studies in Asteroid Research*. Springer International Publishing. https://doi.org/10.1007/978-3-319-58118-7

Davis, D. R., Weidenschilling, S. J., Farinella, P., Paolicchi, P., & Binzel, R. P. (1989). *Asteroid collisional history—Effects on sizes and spins*. 805–826.

De Angelis, S., Manzari, P., De Sanctis, M. C., Ammannito, E., & Di Iorio, T. (2016). VIS-IR study of brucite–clay–carbonate mixtures: Implications for Ceres surface composition. *Icarus*, *280*, 315–327. https://doi.org/10.1016/j.icarus.2016.07.002

De Sanctis, M. C., Ammannito, E., Raponi, A., Marchi, S., McCord, T. B., McSween, H. Y., Capaccioni, F., Capria, M. T., Carrozzo, F. G., Ciarniello, M., Longobardo, A., Tosi, F., Fonte, S., Formisano, M., Frigeri, A., Giardino, M., Magni, G., Palomba, E., Turrini, D.,

… Russell, C. T. (2015). Ammoniated phyllosilicates with a likely outer Solar System origin on (1) Ceres. *Nature*, *528*(7581), 241–244. https://doi.org/10.1038/nature16172

DeMeo, F. E., Binzel, R. P., Slivan, S. M., & Bus, S. J. (2009). An extension of the Bus asteroid taxonomy into the near-infrared. *Icarus*, *202*(1), 160–180. https://doi.org/10.1016/j.icarus.2009.02.005

Dodd, R. T. (1981). *Meteorites: A Petrologic-chemical Synthesis.* Cambridge University Press Archive.

Ehrenfreund, P., Glavin, D. P., Botta, O., Cooper, G., & Bada, J. L. (2001). Extraterrestrial amino acids in Orgueil and Ivuna: Tracing the parent body of CI type carbonaceous chondrites. *Proceedings of the National Academy of Sciences of the United States of America*, 98(5), 2138–2141. https://doi.org/10.1073/pnas.051502898

Endress, M., Zinner, E., & Bischoff, A. (1996). Early aqueous activity on primitive meteorite parent bodies. *Nature*, *379*(6567), 701–703. https://doi.org/10.1038/379701a0

Eschrig, J., Bonal, L., Beck, P., & Prestgard, T. J. (2021). Spectral reflectance analysis of type 3 carbonaceous chondrites and search for their asteroidal parent bodies. *Icarus*, 354, 114034. https://doi.org/10.1016/j.icarus.2020.114034

Farinella, P., Gonczi, R., & Froeschlé, C. (1993). The Injection of Asteroid Fragments into Resonances. *Icarus* (Vol. 101, Issue 2, pp. 174–187). https://doi.org/10.1006/icar.1993.1016

Farinella, Paolo, & Davis, D. R. (1992). Collision rates and impact velocities in the main asteroid belt. *Icarus*, *97*(1), 111–123. https://doi.org/10.1016/0019-1035(92)90060-K

Fedele, D., Tazzari, M., Booth, R., Testi, L., Clarke, C. J., Pascucci, I., Kospal, A., Semenov, D., Bruderer, S., Henning, T., & Teague, R. (2018). ALMA continuum observations of the protoplanetary disk AS 209—Evidence of multiple gaps opened by a single planet. *Astronomy & Astrophysics*, *610*, A24. https://doi.org/10.1051/0004-6361/201731978

Feierberg, M. A., Lebofsky, L. A., & Larson, H. P. (1981). Spectroscopic evidence for aqueous alteration products on the surfaces of low-albedo asteroids. *Geochimica et Cosmochimica Acta*, *45*(6), 971–981. https://doi.org/10.1016/0016-7037(81)90121-6

Feierberg, M. A., Lebofsky, L. A., & Tholen, D. J. (1985). The nature of c-class asteroids from 3-μm spectrophotometry. *Icarus*, *63*(2), 183–191. https://doi.org/10.1016/0019-1035(85)90002-8

Ferrari, M., De Angelis, S., De Sanctis, M. C., Ammannito, E., Stefani, S., & Piccioni, G. (2019). Reflectance spectroscopy of ammonium-bearing phyllosilicates. *Icarus*, *321*, 522–530. https://doi.org/10.1016/j.icarus.2018.11.031

Ferraz-Mello, S. (1994). Kirkwood Gaps and Resonant Groups. In A. Milani, M. Di Martino, & A. Cellino (Eds.), *Asteroids, Comets, Meteors 1993* (pp. 175–188). Springer Netherlands. https://doi.org/10.1007/978-94-011-1148-5_13

Fieber-Beyer, S. K., & Gaffey, M. J. (2020). The Family of (6) Hebe. *The Planetary Science Journal*, *1*(3), 68. https://doi.org/10.3847/PSJ/abc17a

Fornasier, S., Lantz, C., Barucci, M. A., & Lazzarin, M. (2014). Aqueous alteration on main belt primitive asteroids: Results from visible spectroscopy. *Icarus*, *233*, 163–178. https://doi.org/10.1016/j.icarus.2014.01.040

Froeschle, Ch., & Scholl, H. (1986). The secular resonance nu6 in the asteroidal belt. *Astronomy and Astrophysics*, *166*, 326–332.

Frost, B. R., & Beard, J. S. (2007). On Silica Activity and Serpentinization. *Journal of Petrology*, *48*(7), 1351–1368. https://doi.org/10.1093/petrology/egm021

Frost, R. L., & Kloprogge, J. T. (1999). Infrared emission spectroscopic study of brucite. *Spectrochimica Acta - Part A: Molecular and Biomolecular Spectroscopy*, *55*(11), 2195–2205. https://doi.org/10.1016/S1386-1425(99)00016-5

Fukagawa, M., Tamura, M., Itoh, Y., Kudo, T., Imaeda, Y., Oasa, Y., Hayashi, S. S., & Hayashi, M. (2006). Near-Infrared Images of Protoplanetary Disk Surrounding HD 142527. *The Astrophysical Journal*, *636*(2), L153–L156. https://doi.org/10.1086/500128

Gaffey, M. J. (1976). Spectral reflectance characteristics of the meteorite classes. *Journal of Geophysical Research*, 81(5), 905–920. https://doi.org/10.1029/JB081i005p00905

Gaffey, M. J. (1997). Surface Lithologic Heterogeneity of Asteroid 4 Vesta. *Icarus*, 127(1), 130–157. https://doi.org/10.1006/icar.1997.5680

Gaffey, M. (2002). Mineralogy of Asteroids. In *Asteroids III* (pp. 183–204). The University of Arizona Press. papers2://publication/uuid/A789CEFE-2D07-4930-A9F1-FB79D67E7DF2

Gaffey, M. (2003). Observational and Data Reduction Techniques to Optimize Mineralogical Characterizations of Asteroid Surface Materials. *Lunar and Planetary Proceedings #34*. http://adsabs.harvard.edu/abs/2003LPI....34.1602G

Gaffey, M. J., Burbine, T. H., & Binzel, R. P. (1993). Asteroid spectroscopy: Progress and perspectives. *Meteoritics*, *28*(2), 161–187. https://doi.org/10.1111/j.1945-5100.1993.tb00755.x

Gaffey, M. (2010). Space weathering and the interpretation of asteroid reflectance spectra. *Icarus*, *209*(2), 564–574. https://doi.org/10.1016/j.icarus.2010.05.006

Gaffey, M. J., Bell, J. F., Brown, R. H., Burbine, T. H., Piatek, J. L., Reed, K. L., & Chaky, D. A. (1993). Mineralogical Variations within the S-Type Asteroid Class. *Icarus*, *106*(2), 573–602. https://doi.org/10.1006/icar.1993.1194

Gaffey, M. J., & Gilbert, S. L. (1998). Asteroid 6 Hebe: The probable parent body of the H-type ordinary chondrites and the IIE iron meteorites. *Meteoritics & Planetary Science*, *33*(6), 1281–1295. https://doi.org/10.1111/j.1945-5100.1998.tb01312.x

Gaffey, M., & McCord, T. (1978). Asteroid Surface Materials: Mineralogical Characterizations from Reflectance Spectra. *Space Science Reviews*, 21, 555–628.

Gaffey, S. J. (1993). Ultraviolet, Visible, and Near-Infrared Reflectance Spectroscopy: Laboratory Spectra of Geologic Materials. In *Remote Geochemical Analysis: Elemental and Mineralogical Compostion* (pp. 43–77). Cambridge University Press.

Gehrels, T. (1970). Photometry of asteroids. *Academic Press, Inc. London*, 317–375.

Greenwood, R. C., Franchi, I. A., Kearsley, A. T., & Alard, O. (2010). The relationship between CK and CV chondrites. *Geochimica et Cosmochimica Acta*, *74*(5), 1684–1705. https://doi.org/10.1016/j.gca.2009.11.029

Gold, T. (1955). The Lunar Surface. *Monthly Notices of the Royal Astronomical Society*, 115(6), 585–604. https://doi.org/10.1093/mnras/115.6.585

Gomes, R., Levison, H. F., Tsiganis, K., & Morbidelli, & A. (2005). Origin of the cataclysmic Late Heavy Bombardment period of the terrestrial planets. *Nature Letters* (435) p. 466-469. https://doi.org/10.1038/nature03676

Goodrich, C. A. (1992). Ureilites: A critical review. *Meteoritics*, *27*(4), 327–352. https://doi.org/10.1111/j.1945-5100.1992.tb00215.x

Hapke, B. W., Cohen, A. J., Cassidy, W. A., & Wells, E. N. (1970). Solar radiation effects on the optical properties of Apollo 11 samples. *Geochimica et Cosmochimica Acta Supplement*, 1, 2199.

Hapke, B. (2001). Space weathering from Mercury to the asteroid belt. *Journal of Geophysical Research: Planets*, *106*(E5), 10039–10073. https://doi.org/10.1029/2000JE001338

Harlov, D. E., Andrut, M., & Melzer, S. (2001). Characterization of NH4-phlogopite (NH4) (Mg3) [AlSi3O10] (OH)2 and ND4-phlogopite (ND4) (Mg3) [AlSi3O10] (OD)2 using IR spectroscopy and Rietveld refinement of XRD spectra. *Physics and Chemistry of Minerals*, *28*(2), 77–86. https://doi.org/10.1007/s002690000138

Harries, D., Hoppe, P., & Langenhorst, F. (2015). Reactive ammonia in the solar protoplanetary disk and the origin of Earth's nitrogen. *Nature Geoscience*, *8*(2), 97–101. https://doi.org/10.1038/ngeo2339

Hearnshaw, J. B. (2014). *The Analysis of Starlight* (2nd edition). Cambridge University Press.

Herzberg, G. (1945). *Infrared and Raman spectra of polyatomic molecules*. Van Nostrand. New York.

Hiroi, T., Pieters, C. M., Rutherford, M. J., Zolensky, M. E., Sasaki, S., Ueda, Y., & Miyamoto, M. (2004). What are the P-type Asteroids Made Of? *Lunar and Planetary Science* (35). http://adsabs.harvard.edu/abs/2004LPI....35.1616H

Hiroi, Takahiro, Pieters, C. M., & Takeda, H. (1994). Grain size of the surface regolith of asteroid 4 Vesta estimated from its reflectance spectrum in comparison with HED meteorites. *Meteoritics*, *29*(3), 394–396. https://doi.org/10.1111/j.1945-5100.1994.tb00603.x

Hiroi, Takahiro, Pieters, C. M., Zolensky, M. E., & Lipschutz, M. E. (1993). Evidence of Thermal Metamorphism on the C, G, B, and F Asteroids. *Science*, *261*, 1016–1018.

Hiroi, Takahiro, Zolensky, M. E., Pieters, C. M., & Lipschutz, M. E. (1996). Thermal metamorphism of the C, G, B, and F asteroids seen from the 0.7 μm, 3 μm, and UV absorption strengths in comparison with carbonaceous chondrites. *Meteoritics & Planetary Science*, *31*(1), 321–327. https://doi.org/10.1111/j.1945-5100.1996.tb02068.x

Hiroi, T., & Sasaki, S. (2001). Importance of space weathering simulation products in compositional modeling of asteroids: 349 Dembowska and 446 Aeternitas as examples. *Meteoritics & Planetary Science*, *36*(12), 1587–1596. https://doi.org/10.1111/j.1945-5100.2001.tb01850.x

Hoyle, F. (1960). The Origin of the Solar Nebula. *Quarterly Journal of the Royal Astronomical Society*, *1*, 28.

Humboldt, A. von. (2015). *Cosmos: A Sketch of A Physical Description of the Universe Volume 2*. Palala Press.

Hunt, G. R., & Ashley, R. P. (1979). Spectra of altered rocks in the visible and near infrared. *Economic Geology*, *74*(7), 1613–1629. https://doi.org/10.2113/gsecongeo.74.7.1613

Hunt, Graham R. (1977). Spectral signatures of particulate minerals in the visible and near infrared. *GEOPHYSICS*, *42*(3), 501–513. https://doi.org/10.1190/1.1440721

Hunt, Graham R. (1979). Near-infrared (1.3–2.4) μm spectra of alteration minerals—Potential for use in remote sensing. *Geophysics*, *44*(12), 1974–1986. https://doi.org/10.1190/1.1440951

Johnson, T. V., & Fanale, F. P. (1973). Optical properties of carbonaceous chondrites and their relationship to asteroids. *Journal of Geophysical Research*, *78*(35), 8507–8518. https://doi.org/10.1029/jb078i035p08507

Jones, T. D., Lebofsky, L. A., & Marley, M. S. (1990). The Composition and Origin of the C, P, and D Asteroids: Water as a Tracer of Thermal Evolution. *Icarus*, *192*(1), 172–192.

Kaasalainen, M., & Torppa, J. (2001). Optimization Methods for Asteroid Lightcurve Inversion: I. Shape Determination. *Icarus*, *153*(1), 24–36. https://doi.org/10.1006/icar.2001.6673

Kaplan, H. H., Lauretta, D. S., Simon, A. A., Hamilton, V. E., DellaGiustina, D. N., Golish, D. R., Reuter, D. C., Bennett, C. A., Burke, K. N., Campins, H., Connolly, H. C., Dworkin, J. P., Emery, J. P., Glavin, D. P., Glotch, T. D., Hanna, R., Ishimaru, K., Jawin, E. R., McCoy, T. J., … Enos, H. L. (2020). Bright carbonate veins on asteroid (101955) Bennu: Implications for aqueous alteration history. *Science*, *370*(6517). https://doi.org/10.1126/science.abc3557

Kataoka, A., Tsukagoshi, T., Momose, M., Nagai, H., Muto, T., Dullemond, C. P., Pohl, A., Fukagawa, M., Shibai, H., Hanawa, T., & Murakawa, K. (2016). SUBMILLIMETER POLARIZATION OBSERVATION OF THE PROTOPLANETARY DISK AROUND HD 142527. *The Astrophysical Journal*, *831*(2), L12. https://doi.org/10.3847/2041-8205/831/2/L12

Keil, K. (1968). Mineralogical and chemical relationships among enstatite chondrites. *Journal of Geophysical Research* (1896-1977), 73(22), 6945–6976. https://doi.org/10.1029/JB073i022p06945

Keil, K. (2000). Thermal alteration of asteroids: Evidence from meteorites. *Planetary and Space Science*, *48*(10), 887–903. https://doi.org/10.1016/S0032-0633(00)00054-4

Keller, L. P., & McKay, D. S. (1997). The nature and origin of rims on lunar soil grains. *Geochimica et Cosmochimica Acta*, *61*(11), 2331–2341. https://doi.org/10.1016/S0016-7037(97)00085-9

Kallemeyn, G. W., & Wasson, J. T. (1982). The compositional classification of chondrites: III. Ungrouped carbonaceous chondrites. *Geochimica et Cosmochimica Acta*, *46*(11), 2217–2228. https://doi.org/10.1016/0016-7037(82)90196-X

King, T., Clark, R. N., Calvin, W. M., Sherman, D. M., & Brown, R. H. (1992). Evidence for ammonium-bearing minerals on Ceres. *Science*, *255*(5051), 1551–1553. https://doi.org/10.1126/science.255.5051.1551

King, T. V. V., & Clark, R. (1986). Spectral Characteristics of Serpentines and Chlorites Using High Resolution Reflectance Spectroscopy. *Lunar and Planetary Institute 600*, 33.

King, Trude V. V., & Clark, R. N. (1989). Spectral characteristics of chlorites and Mg-serpentines using high-resolution reflectance spectroscopy. *Journal of Geophysical Research: Solid Earth*, *94*(B10), 13997–14008. https://doi.org/10.1029/JB094iB10p13997

Kirkwood, D. (1867). *Meteoric astronomy a treatise on shooting stars, fireballs and aerolites*.

Kleine, T., Münker, C., Mezger, K., & Palme, H. (2002). Rapid accretion and early core formation on asteroids and the terrestrial planets from Hf–W chronometry. *Nature*, *418*(6901), 952–955. https://doi.org/10.1038/nature00982

Krohn, K., Jaumann, R., Stephan, K., Otto, K. A., Schmedemann, N., Wagner, R. J., Matz, K. D., Tosi, F., Zambon, F., von der Gathen, I., Schulzeck, F., Schröder, S. E., Buczkowski, D. L., Hiesinger, H., McSween, H. Y., Pieters, C. M., Preusker, F., Roatsch, T., Raymond, C. A., … Williams, D. A. (2016). Cryogenic flow features on Ceres: Implications for crater-related cryovolcanism. *Geophysical Research Letters*, *43*(23), 11,994-12,003. https://doi.org/10.1002/2016GL070370

Krohn, K., Neesemann, A., Jaumann, R., Otto, K. A., Stephan, K., Wagner, R. J., Tosi, F., Zambon, F., Ruesch, O., Williams, D. A., Raymond, C. A., & Russell, C. T. (2018). Ring-Mold Craters on Ceres: Evidence for Shallow Subsurface Water Ice Sources. *Geophysical Research Letters*, *45*(16), 8121–8128. https://doi.org/10.1029/2018GL078697

Küppers, M., O'Rourke, L., Bockelée-Morvan, D., Zakharov, V., Lee, S., von Allmen, P., Carry, B., Teyssier, D., Marston, A., Müller, T., Crovisier, J., Barucci, M. A., & Moreno, R. (2014). Localized sources of water vapour on the dwarf planet (1) Ceres. *Nature*, *505*(7484), 525–527. https://doi.org/10.1038/nature12918

Lantz, C., & Clark, B. E. (2012). Space weathering on low albedo asteroids. *European Planetary Science Congress 2012*, *7*, 3–5.

Laplace, P. S. marquis de. (1835). *Exposition du système du monde*. Bachelier.

Larkin, P. (2011). *Infrared and Raman Spectroscopy: Principles and Spectral Interpretation (1st ed.)*. Elsevier.

Larson, H. P., Feierberg, M. A., Fink, U., & Smith, H. A. (1979). Remote spectroscopic identification of carbonaceous chondrite mineralogies: Applications to Ceres and Pallas. *Icarus*, *39*(2), 257–271. https://doi.org/10.1016/0019-1035(79)90168-4

Lauretta, D. S., Hua, X., & Buseck, P. R. (2000). Mineralogy of fine-grained rims in the alh 81002 cm chondrite. *Geochimica et Cosmochimica Acta*, *64*(19), 3263–3273. https://doi.org/10.1016/S0016-7037(00)00425-7

Lazzarin, M., Marchi, S., Moroz, L. V., Brunetto, R., Magrin, S., Paolicchi, P., & Strazzulla, G. (2006). Space Weathering in the Main Asteroid Belt: The Big Picture. *The Astrophysical Journal*, *647*(2), L179–L182. https://doi.org/10.1086/507448

Lebofsky, L. A. (1978). Asteroid 1 Ceres: Evidence for water of hydration. *Monthly Notices of the Royal Astronomical Society*, *182*(1), 17–21.

Lebofsky, L. A. (1980). Infrared Reflectance Spectra of Asteroids: A Search for Water of hydration. *The Astronomical Journal*, *85*(5), 573–585. https://doi.org/10.1017/CBO9781107415324.004

Leshin, L. A., Rubin, A. E., & McKeegan, K. D. (1997). The oxygen isotopic composition of olivine and pyroxene from CI chondrites. *Geochimica et Cosmochimica Acta*, 61(4), 835–845. https://doi.org/10.1016/S0016-7037(96)00374-2

Li, J.-Y., Reddy, V., Nathues, A., Corre, L. L., Izawa, M. R. M., Cloutis, E. A., Sykes, M. V., Carsenty, U., Castillo-Rogez, J. C., Hoffmann, M., Jaumann, R., Krohn, K., Mottola, S., Prettyman, T. H., Schaefer, M., Schenk, P., Schröder, S. E., Williams, D. A., Smith, D. E., … Russell, C. T. (2016). Surface Albedo and Spectral Variability of Ceres. *The Astrophysical Journal*, *817*(2), L22. https://doi.org/10.3847/2041-8205/817/2/L22

Longobardo, A., Palomba, E., Carrozzo, F. G., Galiano, A., De Sanctis, M. C., Stephan, K., Tosi, F., Raponi, A., Ciarniello, M., Zambon, F., Frigeri, A., Ammannito, E., Raymond, C. A., & Russell, C. T. (2019). Mineralogy of the Occator quadrangle. *Icarus*, *318*, 205–211. https://doi.org/10.1016/j.icarus.2017.09.022

Lorenz, C., Kurat, G., Brandstätter, F., & Nazarov, M. A. (2003). *NWA 1235: A Phlogopite-bearing Enstatite Meteorite*. *34*. http://adsabs.harvard.edu/abs/2003LPI....34.1211L

Lutgens, F. K., Tarbuck, E. J., & Tasa, D. G. (2012). *Essentials of Geology* (11th ed.). Prentice Hall.

Mann, R. J. (1853). A guide to the knowledge of the heavens. *London, Jarrold & Sons, [1853] 2d Ed., 2nd*. http://adsabs.harvard.edu/abs/1853gkhe.book.....M

Marchi, S., Raponi, A., Prettyman, T. H., De Sanctis, M. C., Castillo-Rogez, J., Raymond, C. A., Ammannito, E., Bowling, T., Ciarniello, M., Kaplan, H., Palomba, E., Russell, C. T., Vinogradoff, V., & Yamashita, N. (2019). An aqueously altered carbon-rich Ceres. *Nature Astronomy*, *3*(2), 140–145. https://doi.org/10.1038/s41550-018-0656-0

Mason, B. (1967). Meteorites. *American Scientist*, 55(4), 429–455.

McCord, T., Adams, J., & Johnson, T. (1970). Asteroid Vesta: Spectral Reflectivity and Compositional Implications. *Science*, *168*(3938), 1445–1447.

McSween, H. Y. (2006). *Meteorites and their Parent Planets* (2nd ed.). Cambridge University Press.

McSween, H. Y., Richardson, S. M. (1977). The composition of carbonaceous chondrite matrix. *Geochimica et Cosmochimica Acta*, 41(8), 1145–1161.

Melvill, T. (1754). Observations of Light and Colours. In *Essays and Observations, Physical Literacy* (Vol. 2, p. 30). Edinburgh.

Mennella, V., Baratta, G. A., Esposito, A., Ferini, G., & Pendleton, Y. J. (2003). The Effects of Ion Irradiation on the Evolution of the Carrier of the 3.4 Micron Interstellar Absorption Band. *The Astrophysical Journal*, *587*(2), 727–738. https://doi.org/10.1086/368342

Miles, R. (2007). A light history of photometry: From Hipparchus to the Hubble Space Telescope. *Journal of the British Astronomical Association*, *117*(4), 172–186. https://doi.org/2007JBAA..117..172M

Milliken, R. E., & Rivkin, A. S. (2009). Brucite and carbonate assemblages from altered olivine-rich materials on Ceres. *Nature Geoscience*, *2*(4), 258–261. https://doi.org/10.1038/ngeo478

Mittlefehldt, D. W., Bogard, D. D., Berkley, J. L., & Garrison, D. H. (2003). Brachinites: Igneous rocks from a differentiated asteroid. *Meteoritics & Planetary Science*, *38*(11), 1601–1625. https://doi.org/10.1111/j.1945-5100.2003.tb00004.x

Mookherjee, M., Redfern, S. A. T., Zhang, M., & Harlov, D. E. (2002). Orientational order-disorder of N(D,H)4+ in tobelite. *American Mineralogist*, *87*(11–12), 1686–1691. https://doi.org/10.2138/am-2002-11-1218

Moroz, L. V., Fisenko, A. V., Semjonova, L. F., Pieters, C. M., & Korotaeva, N. N. (1996). Optical Effects of Regolith Processes on S-Asteroids as Simulated by Laser Shots on Ordinary Chondrite and Other Mafic Materials. *Icarus*, *122*(2), 366–382. https://doi.org/10.1006/icar.1996.0130

Morris, R. V. (1978). The surface exposure/maturity/of lunar soils-Some concepts and Is/FeO compilation. *Lunar and Planetary Science Conference Proceedings*, 9, 2287–2297.

Morris, RICHARD V. (1978). In situ reworking/gardening/of the lunar surface-Evidence from the Apollo cores. *Lunar and Planetary Science Conference Proceedings*, 9, 1801–1811.

Morris, R. V., Lauer, H. V., Lawson, C. A., Gibson, E. K., Nace, G. A., & Stewart, C. (1985). Spectral and other physicochemical properties of submicron powders of hematite (α-Fe2O3), maghemite (γ-Fe2O3), magnetite (Fe3O4), goethite (α-FeOOH), and lepidocrocite (γ-FeOOH). *Journal of Geophysical Research: Solid Earth*, *90*(B4), 3126–3144. https://doi.org/10.1029/JB090iB04p03126

Muñoz Caro, G. M., Ruiterkamp, R., Schutte, W. A., Greenberg, J. M., & Mennella, V. (2001). UV photodestruction of CH bonds and the evolution of the 3.4 μm feature carrier—I. The case of aliphatic and aromatic molecular species. *Astronomy & Astrophysics*, *367*(1), 347–354. https://doi.org/10.1051/0004-6361:20000341

Murchie, S., Robinson, M., Clark, B., Li, H., Thomas, P., Joseph, J., Bussey, B., Domingue, D., Veverka, J., Izenberg, N., & Chapman, C. (2002). Color Variations on Eros from NEAR Multispectral Imaging. *Icarus*, *155*(1), 145–168. https://doi.org/10.1006/icar.2001.6756

Mustard, J. F., & Hays, J. E. (1997). Effects of Hyperfine Particles on Reflectance Spectra from 0.3 to 25 μm. *Icarus*, *125*(1), 145–163. https://doi.org/10.1006/icar.1996.5583

Nathues, A., Hoffmann, M., Schaefer, M., Le Corre, L., Reddy, V., Platz, T., Cloutis, E. A., Christensen, U., Kneissl, T., Li, J. Y., Mengel, K., Schmedemann, N., Schaefer, T., Russell, C. T., Applin, D. M., Buczkowski, D. L., Izawa, M. R. M., Keller, H. U.,

O'Brien, D. P., … Vincent, J. B. (2015). Sublimation in bright spots on (1) Ceres. *Nature*, *528*(7581), 237–240. https://doi.org/10.1038/nature15754

Nehru, C. E., Prinz, M., Weisberg, M. K., Ebihara, M., Clayton, R. N., & Mayeda, T. K. (1992). Brachinites: A new primitive achondrite group. *Meteoritics*, 27.

Nesvorný, D., & Morbidelli, A. (1998). Three-Body Mean Motion Resonances and the Chaotic Structure of the Asteroid Belt. *The Astronomical Journal*, *116*(6), 3029–3037. https://doi.org/10.1086/300632

Nesvorný, David, Jedicke, R., Whiteley, R. J., & Ivezić, Ž. (2005). Evidence for asteroid space weathering from the Sloan Digital Sky Survey. *Icarus*, *173*(1), 132–152. https://doi.org/10.1016/j.icarus.2004.07.026

Newton, I. (1704). *Opticks, or, a Treatise of the Reflexions, Refractions, Inflexions and Colours of Light; also Two Treatises of the Species and Magnitude of Curvilinear Figures*. http://www.archive.org/details/gri_c00033125008801785

Noble, S. K., Pieters, C. M., & Keller, L. P. (2007). An experimental approach to understanding the optical effects of space weathering. *Icarus*, 192(2), 629–642. https://doi.org/10.1016/j.icarus.2007.07.021

Noguchi, T., Nakamura, T., Kimura, M., Zolensky, M. E., Tanaka, M., Hashimoto, T., Konno, M., Nakato, A., Ogami, T., Fujimura, A., Abe, M., Yada, T., Mukai, T., Ueno, M., Okada, T., Shirai, K., Ishibashi, Y., & Okazaki, R. (2011). Incipient Space Weathering Observed on the Surface of Itokawa Dust Particles. *Science*, *333*(6046), 1121–1125. https://doi.org/10.1126/science.1207794

Noguchi, Takaaki, Kimura, M., Hashimoto, T., Konno, M., Nakamura, T., Zolensky, M. E., Okazaki, R., Tanaka, M., Tsuchiyama, A., Nakato, A., Ogami, T., Ishida, H., Sagae, R., Tsujimoto, S., Matsumoto, T., Matsuno, J., Fujimura, A., Abe, M., Yada, T., … Ishibashi, Y. (2014). Space weathered rims found on the surfaces of the Itokawa dust particles. *Meteoritics & Planetary Science*, *49*(2), 188–214. https://doi.org/10.1111/maps.12111

Noonan, J. W., Reddy, V., Harris, W. M., Bottke, W. F., Sanchez, J. A., Furfaro, R., Brown, Z., Fernandes, R., Kareta, T., Lejoly, C., Nallapu, R. T., Niazi, H. K., Slick, L. R., Schatz, L., Sharkey, B. N. L., Springmann, A., Angle, G., Bailey, L., Acuna, D. D., … Wilburn, G. (2019). Search for the H Chondrite Parent Body among the Three Largest S-type Asteroids: (3) Juno, (7) Iris, and (25) Phocaea. *The Astronomical Journal*, *158*(5), 213. https://doi.org/10.3847/1538-3881/ab4813

Ostrowski, D. R., Gietzen, K., Lacy, C., & Sears, D. W. G. (2010). An investigation of the presence and nature of phyllosilicates on the surfaces of C asteroids by an analysis of the continuum slopes in their near-infrared spectra. *Meteoritics and Planetary Science*, *45*(4), 615–637. https://doi.org/10.1111/j.1945-5100.2010.01047.x

Papanastassiou, D., & Wasserburg, G. (1975). Rb-Sr study of a lunar dunite and evidence for early lunar differentiates. *Proceedings from the Lunar and Planetary conference*, 6, 1467-1489.

Papike, J. J., & Cameron, M. (1976). Crystal chemistry of silicate minerals of geophysical interest. *Reviews of Geophysics*, *14*(1), 37–80. https://doi.org/10.1029/RG014i001p00037

Park, R. S., Konopliv, A. S., Bills, B. G., Rambaux, N., Castillo-Rogez, J. C., Raymond, C. A., Vaughan, A. T., Ermakov, A. I., Zuber, M. T., Fu, R. R., Toplis, M. J., Russell, C. T., Nathues, A., & Preusker, F. (2016). A partially differentiated interior for (1) Ceres deduced from its gravity field and shape. *Nature*, *537*(7621), 515–517. https://doi.org/10.1038/nature18955

Patterson, C. (1956). Age of meteorites and the earth. *Geochimica et Cosmochimica Acta*, *10*(4), 230–237. https://doi.org/10.1016/0016-7037(56)90036-9

Peebles, C. (2000). *Asteroids: A History* (1st edition). Smithsonian Institution Press.

Pfalzner, S., Davies, M. B., Gounelle, M., Johansen, A., Münker, C., Lacerda, P., Zwart, S. P., Testi, L., Trieloff, M., & Veras, D. (2015). The formation of the solar system. *Physica Scripta*, *90*(6), 068001. https://doi.org/10.1088/0031-8949/90/6/068001

Pieters, C. M., Taylor, L. A., Noble, S. K., Keller, L. P., Hapke, B., Morris, R. V., Allen, C. C., McKAY, D. S., & Wentworth, S. (2000). Space weathering on airless bodies: Resolving a mystery with lunar samples. *Meteoritics & Planetary Science*, 35(5), 1101–1107.

Pilcher, F. (1979). Circumstances of minor planet discovery. *Asteroids*, 1130–1154.

Pitjeva, E. V., & Pitjev, N. P. (2018). Masses of the Main Asteroid Belt and the Kuiper Belt from the Motions of Planets and Spacecraft. *Astronomy Letters*, *44*(8–9), 554–566. https://doi.org/10.1134/S1063773718090050

Pizzarello, S., & Williams, L. B. (2012). Ammonia in the Early Solar System: An Account from Carbonaceous Meteorites. *The Astrophysical Journal*, *749*(2), 161. https://doi.org/10.1088/0004-637X/749/2/161

Prior, G. T. (1920). The classification of Meteorites. *Mineralogical Magazine and Journal of the Mineralogical Society*, 19(90), 51–63. https://doi.org/10.1180/minmag.1920.019.90.01

Prinz, M., Nehru, C. E., Delaney, J. S., & Weisberg, M. (1983). Silicates in IAB and IIICD Irons, Winonaites, Lodranites an Brachina: A Primitive and Modified-Primitive Group. *Lunar and Planetary Science Conference*, *14*, 616–617.

Rayner, J. T., Toomey, D. W., Onaka, P. M., Denault, A. J., Stahlberger, W. E., Vacca, W. D., Cushing, M. C., & Wang, S. (2003). SpeX: A Medium-Resolution 0.8–5.5 Micron Spectrograph and Imager for the NASA Infrared Telescope Facility. *Publications of the Astronomical Society of the Pacific*, *115*(805), 362–382. https://doi.org/10.1086/367745

Reddy, V. (2016). *Reddy Main Belt Asteroid Spectra V1.0*. EAR-A-I0046-3-REDDYMBSPEC-V1.0. NASA Planetary Data System. https://sbnapps.psi.edu/ferret/datasetDetail.action?dataSetId=EAR-A-I0046-3-REDDYMBSPEC-V1.0

Rivkin, A. S., Davies, J. K., Johnson, J. R., Ellison, S. L., Trilling, D. E., Brown, R. H., & Lebofsky, L. A. (2003). Hydrogen concentrations on C-class asteroids derived from remote sensing. *Meteoritics & Planetary Science*, *38*(9), 1383–1398. https://doi.org/10.1111/j.1945-5100.2003.tb00321.x

Rivkin, A. S., Volquardsen, E. L., & Clark, B. E. (2006). The surface composition of Ceres: Discovery of carbonates and iron-rich clays. *Icarus*, *185*(2), 563–567. https://doi.org/10.1016/j.icarus.2006.08.022

Rousseau, B., Sanctis, M. C. D., Raponi, A., Ciarniello, M., Ammannito, E., Frigeri, A., Ferrari, M., Angelis, S. D., Carrozzo, F. C., Tosi, F., Schröder, S. E., Raymond, C. A., & Russell, C. T. (2020). The surface of (1) Ceres in visible light as seen by Dawn/VIR. *Astronomy & Astrophysics*, *642*, A74. https://doi.org/10.1051/0004-6361/202038512

Rubin, A. E. (1997). Mineralogy of meteorite groups. *Meteoritics & Planetary Science*, *32*(2), 231–247. https://doi.org/10.1111/j.1945-5100.1997.tb01262.x

Ruesch, O., Platz, T., Schenk, P., McFadden, L. A., Castillo-Rogez, J. C., Quick, L. C., Byrne, S., Preusker, F., O'Brien, D. P., Schmedemann, N., Williams, D. A., Li, J.-Y., Bland, M. T., Hiesinger, H., Kneissl, T., Neesemann, A., Schaefer, M., Pasckert, J. H., Schmidt, B. E., … Russell, C. T. (2016). Cryovolcanism on Ceres. *Science*, *353*(6303). https://doi.org/10.1126/science.aaf4286

Russell, C. T., Raymond, C. A., Ammannito, E., Buczkowski, D. L., De Sanctis, M. C., Hiesinger, H., Jaumann, R., Konopliv, A. S., McSween, H. Y., Nathues, A., Park, R. S., Pieters, C. M., Prettyman, T. H., McCord, T. B., McFadden, L. A., Mottola, S., Zuber, M. T., Joy, S. P., Polanskey, C., … Yamashita, N. (2016). Dawn arrives at ceres: Exploration of a small, volatile-rich world. *Science*, *353*(6303), 1008–1010. https://doi.org/10.1126/science.aaf4219

Russel, N. (1906). On the Light-Variations of Asteroids and Satellites. *The Astrophysical Journal*, 24(1), 1–18.

Russell, H. N. (1912). On the Determination of the Orbital Elements of Eclipsing Variable Stars. I. *The Astrophysical Journal*, 35, 315. https://doi.org/10.1086/141942

Ruzicka, A., Snyder, G. A., & Taylor, L. A. (1997). Vesta as the howardite, eucrite and diogenite parent body: Implications for the size of a core and for large-scale differentiation. *Meteoritics & Planetary Science*, *32*(6), 825–840. https://doi.org/10.1111/j.1945-5100.1997.tb01573.x

Sanchez, J. A., Reddy, V., Nathues, A., Cloutis, E. A., Mann, P., & Hiesinger, H. (2012). Phase reddening on near-Earth asteroids: Implications for mineralogical analysis, space

weathering and taxonomic classification. *Icarus*, *220*(1), 36–50. https://doi.org/10.1016/j.icarus.2012.04.008

Sasselov, D. D. (2003). The New Transiting Planet OGLE-TR-56b: Orbit and Atmosphere. *The Astrophysical Journal*, 596(2), 1327–1331. https://doi.org/10.1086/378145

Sawyer, S. R. (1991). *A High Resolution CCD Spectroscopic Survey of Low Albedo Main Belt Asteroids—Results and Analysis*. *23*, 1235.

Serio, G. F., Manara, A., & Sicoli, P. (2002). Giuseppe Piazzi and the Discovery of Ceres. *Asteroids III*, 17–24.

Shu, F. H., Adams, F. C., & Lizano, S. (1987). Star Formation in Molecular Clouds: Observation and Theory. *Annual Review of Astronomy and Astrophysics*, *25*(1), 23–81. https://doi.org/10.1146/annurev.aa.25.090187.000323

Sorby, H. C. (1858). On the Microscopical, Structure of Crystals, indicating the Origin of Minerals and Rocks. *Quarterly Journal of the Geological Society*, *14*(1–2), 453–500. https://doi.org/10.1144/GSL.JGS.1858.014.01-02.44

Stinchcomb, G. A., & Barker, E. F. (1929). The Molecular Spectrum of Ammonia I. Two Types of Infra-Red Vibration Bands. *Physical Review*, *33*(3), 305–308. https://doi.org/10.1103/PhysRev.33.305

Stüeken, E. E., Buick, R., & Schauer, A. J. (2015). Nitrogen isotope evidence for alkaline lakes on late Archean continents. *Earth and Planetary Science Letters*, *411*, 1–10. https://doi.org/10.1016/j.epsl.2014.11.037

Tedesco, E. F., Williams, J. G., Matson, D. L., Weeder, G. J., Gradie, J. C., & Lebofsky, L. A. (1989). A three-parameter asteroid taxonomy. *The Astronomical Journal*, *97*, 580. https://doi.org/10.1086/115007

Tennyson, J. (2005). *Astronomical Spectroscopy: An Introduction to the Atomic and Molecular Physics Of Astronomical Spectroscopy (Vol. 2)*. Imperial College Press.

Tholen, D. (1984). *Asteroid Taxonomy from Cluster Analysis of Photometry*. [PhD Dissertation, University of Arizona]. The University of Arizona Press.

Tholen, D. J., & Barucci, M. A. (1989). Asteroid taxonomy. In R. P. Binzel, T. Gehrels, & M. S. Matthews (Eds.), *Asteroids II* (pp. 298–316). The University of Arizona Press.

Tosi, F., Carrozzo, F. G., Raponi, A., De Sanctis, M. C., Thangjam, G., Zambon, F., Ciarniello, M., Nathues, A., Capria, M. T., Rognini, E., Ammannito, E., Hoffmann, M., Krohn, K., Longobardo, A., Palomba, E., Pieters, C. M., Stephan, K., Raymond, C. A., & Russell, C. T. (2018). Mineralogy and temperature of crater Haulani on Ceres. *Meteoritics and Planetary Science*, *53*(9), 1902–1924. https://doi.org/10.1111/maps.13078

Townsend, T. E. (1987). Discrimination of iron alteration minerals in visible and near-infrared reflectance data. *Journal of Geophysical Research: Solid Earth*, *92*(B2), 1441–1454. https://doi.org/10.1029/JB092iB02p01441

Van Schmus, W. R., & Wood, J. A. (1967). A chemical-petrologic classification for the chondritic meteorites. *Geochimica et Cosmochimica Acta*, 31(5), 747–765.

Vilas, F. (1994). A Cheaper, Faster, Better Way to Detect Water of Hydration on Solar System Bodies. *Icarus*, *111*(2), 456–467.

Vilas, F., & Gaffey, M. J. (1989). Phyllosilicate absorption features in main-belt and outer-belt asteroid reflectance spectra. *Science*, *246*(4931), 790–792. https://doi.org/10.1126/science.246.4931.790

Vilas, F., Jarvis, K. S., & Gaffey, M. J. (1994). Iron Alteration Minerals in the Visible and Near-Infrared Spectra of Low-Albedo Asteroids. *Icarus*, *109*(2), 274–283. https://doi.org/10.1006/icar.1994.1093

Vilas, F., Larson, S. M., Hatch, E. C., & Jarvis, K. S. (1993). CCD Reflectance Spectra of Selected Asteroids. II. Low-Albedo Asteroid Spectra and Data Extraction Techniques. *Icarus*, *105*(1), 67–78. https://doi.org/10.1006/icar.1993.1111

Vilas, F., & Sykes, M. V. (1996). Are low-albedo asteroids thermally metamorphosed? *Icarus*, *124*(2), 483–489. https://doi.org/10.1006/icar.1996.0224

Viikinkoski, M., Hanuš, J., Kaasalainen, M., Marchis, F., & Ďurech, J. (2017). Adaptive optics and lightcurve data of asteroids: Twenty shape models and information content analysis. *Astronomy & Astrophysics*, 607, A117. https://doi.org/10.1051/0004-6361/201731456

Watson, E. C. (1952). The First Reported Observations on Emission Spectra. *American Journal of Physics*, *20*(9), 569–577. https://doi.org/10.1119/1.1933326

Weaver, C., & Pollard, L. (1979). *The Chemistry of Clay Minerals*. Elsevier.

Wells, E., & Hapke, B. (1977). Lunar soil: Iron and titanium bands in the glass fraction. *Science*, 195(4282), 977–979.

Weisberg, M. K., McCoy, T. J., & Krot, A. N. (2006). Systematics and Evaluation of Meteorite Classification. *Meteorites and the Early Solar System II*, 34.

Wetherill, G. W. (1980). Formation of the terrestrial planets. *Annual Review of Astronomy and Astrophysics*, *18*, 77–113. https://doi.org/10.1146/annurev.aa.18.090180.000453

Williams, J. G. (1969). Secular Perturbations in the Solar System. In *Ph.D. Thesis*. http://adsabs.harvard.edu/abs/1969PhDT.....2W

Wing, M. R., & Bada, J. L. (1991). The origin of the polycyclic aromatic hydrocarbons in meteorites. *Origins of Life and Evolution of the Biosphere*, 21(5), 375–383. https://doi.org/10.1007/BF01808308

Wisdom, J. (1983). Chaotic behavior and the origin of the 31 Kirkwood gap. *Icarus*, *56*(1), 51–74. https://doi.org/10.1016/0019-1035(83)90127-6

Wood, J. A. (1967). Chondrites: Their metallic minerals, thermal histories, and parent planets. *Icarus*, 6(1–3), 1–49.

Xu, S., Binzel, R. P., Burbine, T. H., & Bus, S. J. (1995). Small Main-Belt Asteroid Spectroscopic Survey: Initial Results. *Icarus*, *115*(1), 1–35. https://doi.org/10.1006/icar.1995.1075

Zellner, B., Tholen, D. J., & Tedesco, E. F. (1985). The eight-color asteroid survey: Results for 589 minor planets. *Icarus*, *61*(3), 355–416. https://doi.org/10.1016/0019-1035(85)90133-2

Zolensky, M., & McSween, H. Y., Jr. (1988). Aqueous alteration. *Meteorites and the Early Solar System*, 114–143.